

Analysis of Time-Lapse Seismic Technology Using a Physical Model of a Porous Channel Sand

A Thesis
Presented to
the Faculty of the Department of Geosciences
University of Houston

In Partial Fulfillment
of the Requirements for the Degree
Master of Science

By
Ricko Andy Wardhana
August, 2001

ABSTRACT

Time-lapse seismic has become an increasingly popular tool in the oil and gas industry as we move from exploration in new frontier basins to production in more mature basins. The goal of time-lapse seismic is to augment the information measured at injection and production wells by attempting to directly detect the movement of fluid fronts in an effort to more completely sweep hydrocarbons from the reservoir.

I represent my reservoir by an idealized channel sand system. To my knowledge, there are very few physical or numerical model experimental studies on this topic so far. Numerical studies suffer from the computational cost of fully 3-D elastic wave equation modeling. Physical models suffer from the limitation of materials where traditionally, we have used epoxies and resins having a Poisson's ratio of about 0.30. To model the idealized reservoir in question, I collaborated with the UH Art Department, and found that sintered glass beads can model a porous sand having a Poisson's ratio close to 0.10.

I started my work with model fabrication and 3-D acquisition in AGL's physical modeling laboratory, followed with data processing prior to interpretation. I pioneered new experimental techniques and work flows in constructing a model with porous media, injected the chosen media with fluid, and calibrated the transducer radiation patterns for AVO analysis.

I gathered three 3-D datasets over my model corresponding to different fluid distributions. I then processed these data with a simple relative-amplitude preserving flow, including 3-D pre-stack time-migration. I delineated the channel fluid-front by extracting and comparing seismic attributes of the datasets. Of these attributes, seismic coherence and AVO were able to better illuminate channel fluid-front than amplitude extraction, envelope and instantaneous frequency.

TABLE OF CONTENTS

I. INTRODUCTION	1
I.1. Seismic on demand	1
I.2. Aims of the Research.....	2
I.3. Background.....	2
I.4. Organization of the thesis	3
II. SEISMIC AMPLITUDE INTERPRETATION	5
II.1. Reflection coefficient formulation based on Zoeppritz's equations	5
II.2. Gassmann's petrophysical link to seismic.....	7
II.3. The effect of Poisson's ratio on reflection coefficient	9
II.4. Linear approximation of Zoeppritz's equation.....	10
II.4.1. Bortfeld's approximation: The fluid and rigidity terms	10
II.4.2. Aki and Richards' approximation: Velocities and density terms	11
II.4.3. Shuey's approximation: The Normal Incidence and Poisson Reflectivity.....	12
III. POROUS CHANNEL SAND PHYSICAL MODEL EXPERIMENT	14
III.1. Constructing the model	16
III.1.1. Porous channel sand.....	16
III.1.2. Embedding the channel in a 'shale' matrix.....	21
III.1.3. Fluid Injection Apparatus.....	23
III.1.4. Selecting the Pore Fluid	25
III.2. Acquisition Geometry	26
IV. TIME-LAPSE DATA PROCESSING.....	31
IV.1. Assessing data quality.....	31
IV.1.1. Energy irregularity between traces	31

IV.1.2. Signal-to-noise ratio.....	33
IV.1.3. Geometry.....	34
IV.2. Data processing.....	34
IV.2.1. Transducer directivity and geometrical spreading correction.....	34
IV.2.2. Velocity analysis, NMO, and stacking.....	36
IV.2.3. Filtering.....	39
IV.2.4. Time-lapse association between datasets.....	40
IV.2.5. Amplitude balancing.....	41
IV.2.6. Post-stack f-k time migration.....	42
IV.2.7. Pre-stack time migration.....	42
IV.2.8. 2-D migration of vertically-stacked data.....	45
V. SEISMIC ATTRIBUTE ANALYSIS OF TIME-LAPSE DATASETS.....	46
V.1. Time-slice evaluation.....	46
V.2. Seismic attribute analysis.....	52
V.2.1. Instantaneous frequency.....	53
V.2.2. Cross-correlation.....	55
V.2.3. Root-Mean-Square (RMS) amplitude.....	57
V.3. Comparison to the model estimate.....	63
V.4. Coherence analysis.....	70
VI. CONCLUSION.....	73
VI.1. Suggestions for future work.....	74
APPENDIX A.....	76
APPENDIX B.....	90
APPENDIX C.....	95
REFERENCES.....	99

Chapter I

INTRODUCTION

I.1 Seismic on demand

Demand for hydrocarbons increases with increasing industrial development and population growth. As the demand for hydrocarbons rises, we find that most domestic hydrocarbon fields have already been found and exploited. Enormous amounts of oil may remain in the reservoir after the first exploitation attempt due to inaccurate reservoir characterization, or hydrocarbon movement by injection fluids. There is wide opportunity for further exploitation if we can precisely locate new wells based on a more robust reservoir characterization.

The development and application of seismic reflection methods have evolved within the past decade. One of the important seismic technologies being utilized to better understand reservoir characteristics is time-lapse technology, whereby multiple seismic surveys are acquired at different times over the same reservoir. Numerous time-lapse seismic applications have been carried out only within the past few years (Sparkman, 1988). Despite the fact that time-lapse technology has been used widely in both 2-D and 3-D

seismic exploration, it is still quite new, such that further calibration of data acquisition, processing, imaging, and interpretation are needed.

I.2 Aims of the Research

In this thesis, I will design and construct a new class of physical model suitable for studying time-lapse seismic experiments. In particular, I will evaluate amplitude versus offset (AVO) and coherence analysis as a means of mapping fluid movement by acquiring several sets of 3-D physical model data.

I.3 Background

Time-lapse or 4-D seismic is a recently developed tool designed to aid in a more complete exploitation of an existing hydrocarbon reservoir. Clearly, time-lapse seismic increases the cost of seismic data by adding additional surveys. We encounter other problems in using this new method, however. In particular, we suffer from problems of data repeatability, or data registration. In a marine environment subject to tides, currents and a variable sea state, it is difficult to exactly reoccupy the same source and receiver locations, even if we tried. In the land environment, it is unreasonable to expect the same shallow hydrological and soil conditions, giving rise to changes in coupling. In both environments, we may choose to use more modern acquisition equipment or more

effective acquisition techniques. For this reason, relative amplitude processing and seismic attributes appear to be the most promising means of reconciling two 3-D surveys separated by several years (Castagna, 2000).

One way to evaluate which seismic attributes to use is by conducting numerical or physical modeling experiments. Repeatability of seismic acquisition in a time-lapse study can be controlled in a modeling experiment, thereby eliminating this element from our analysis until we are ready to address it. Unfortunately, there are very few, if any, 3-D physical or numerical model studies on time-lapse seismic due to material and computational limitations. 3-D numerical modeling of elastic wave seismic field experiments is currently beyond the capabilities of all but those institutions with the most advanced parallel processing facilities (House et al., 2000). In contrast, 3-D physical scale models are relatively inexpensive, but at the time this thesis was initiated, little had been done in simulating porous permeable reservoirs with Poisson's ratio near 0.1. Nevertheless, difficult experimental problems remain, including the inability to scale fluid viscosity and uncertainties in model construction of porous fluid-filled media.

I.4 Organization of the thesis

This thesis uses experimental time-lapse physical modeling to evaluate AVO and seismic coherence as a fluid-flow detection tool. In Chapter 2, I will introduce a brief background of AVO analysis and seismic coherence. In Chapter 3, I will describe my experimental

technique of material preparation, model making, and data collection. In this chapter, I will also identify the limitations I encountered in model preparation and in physical modeling in general. In Chapters 4 and 5 I will discuss the next steps - data processing, 3-D interpretation, and AVO analysis. Results and conclusions are described in Chapter 6 along with some suggestions for future work.

Chapter II

SEISMIC AMPLITUDE INTERPRETATION

Along with trap definition, porosity estimation and pore-fluid discrimination are the most important geophysical goals in hydrocarbon exploration using the seismic tool. During the past 20 years, the Amplitude Variation with Offset (AVO) attribute has become well established in hydrocarbon reservoir characterization.

The theoretical foundations of AVO were laid by Knott (1899) and Zoeppritz (1919). Their work was extended to modern seismic amplitude by Gassman (1951), Koefoed (1955), Bortfeld (1961), Aki and Richards (1980), Ostrander (1984), Shuey (1985), and Verm and Hilterman (1995). In this chapter, I will provide an overview of recent AVO developments.

II.1 Reflection coefficient formulation based on Zoeppritz's equations

In this section, I will introduce a formulation of reflection coefficient that was developed after Zoeppritz (1919), which later on I will use for computing the AVO response from

the channel model. Consider a plane wave traveling into the earth with an angle θ , that is incident onto an interface separating two different rocks having properties $(\alpha_1, \beta_1, \rho_1,$ and $\alpha_2, \beta_2, \rho_2)$, and is then recorded by a receiver on the earth's surface (Figure 2.1).

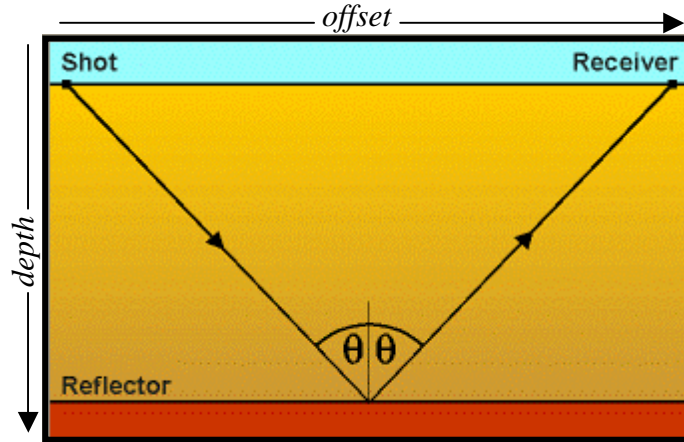


FIG. 2.1. The seismic experiment.

Cerveny and Ravindra (1971) derived a mathematical expression for the reflection coefficient of downgoing P and upgoing P waves that is given as:

$$RC_{PP} = -1 + 2P_1 D^{-1} (\alpha_2 \beta_2 P_2 X^2 + \beta_1 \alpha_2 \rho_1 \rho_2 P_4 + q^2 \Theta^2 P_2 P_3 P_4) \quad (2.1)$$

where

$$D = \alpha_1 \alpha_2 \beta_1 \beta_2 \Theta^2 Z^2 + \alpha_2 \beta_2 P_1 P_2 X^2 + \alpha_1 \beta_1 P_3 P_4 Y^2 + \rho_1 \rho_2 (\beta_1 \alpha_2 P_1 P_4 + \alpha_1 \beta_2 P_2 P_3) + q^2 \Theta^2 P_1 P_2 P_3 P_4,$$

and

$$q = 2(\rho_2 \beta_2^2 - \rho_1 \beta_1^2),$$

$$X = \rho_2 - q \Theta^2, \quad Y = \rho_1 + q \Theta^2, \quad Z = \rho_2 - \rho_1 - q \Theta^2,$$

$$\Theta = \sin \theta_i / V_i, \quad V_1 = \alpha_1, \quad V_2 = \beta_1, \quad V_3 = \alpha_2, \quad V_4 = \beta_2,$$

$$P_i = (1 - V_i^2 \Theta^2)^{1/2} \quad (i = 1, 2, 3, 4).$$

The importance of the formulation above is that it closely fits Zoeppritz's equations. One disadvantage of this long mathematical expression is that we hardly can understand the direct impact of rock-properties on reflection coefficients.

II.2 Gassmann's petrophysical link to seismic

Amplitude anomalies are due to differences in rock properties, such as velocity and density, which in turn are based on differences in material and pore fluid.

Beginning with an elastic isotropic medium, we define the P-wave and S-wave velocities as

$$V_p \text{ (km/s)} = \alpha = \sqrt{\frac{K + \frac{4}{3}\mu}{\rho}}, \quad (2.2.a)$$

$$V_s \text{ (km/s)} = \beta = \sqrt{\frac{\mu}{\rho}}, \quad (2.2.b)$$

and the Poisson's ratio, σ , as a function of V_p and V_s ,

$$\sigma = \frac{\frac{1}{2}\left(\frac{V_p}{V_s}\right)^2 - 1}{\left(\frac{V_p}{V_s}\right)^2 - 1} \quad (2.3)$$

where K is the bulk modulus measured in GPa,

μ is shear modulus measured in GPa,

and ρ is density measured in gm/cm^3 .

K and μ , which indicate the strength of a body, or the amount of strain due to compressional and shear forces, are the main elements that control seismic velocities. Density in general plays a secondary role in determining seismic velocities. Gardner et al. (1974) introduced an early qualitative overview on velocity-density relationship of various rock materials. Porous media filled with fluid are no longer homogeneous on the microscopic scale such that equations 2.2 and 2.3 no longer directly apply. Nevertheless, Gassman (1951) generalized these equations by introducing four components, the dry-rock modulus (K_{dry}), the matrix material modulus (K_{ma}), the pore-fluid (K_{fl}) bulk modulus, and the porosity (ϕ). The dry-rock moduli (K_{dry} and μ_{dry}) are essentially the bulk and shear moduli of a squeezed porous rock when the pore fluid has been removed and pore spaces became open to air. The matrix material (K_{ma}) and pore-fluid (K_{fl}) bulk moduli are the bulk moduli of the mineral and fluid respectively. Gassman's P-wave velocity equation contains two terms, which we call the dry-rock and fluid terms:

$$\rho V_p^2 = \underbrace{K_{dry} + \frac{4}{3}\mu_{dry}}_{\text{Dry-rock term}} + \underbrace{\frac{\left(1 - \frac{K_{dry}}{K_{ma}}\right)^2}{\left(1 - \phi - \frac{K_{dry}}{K_{ma}}\right) \frac{1}{K_{ma}} + \frac{\phi}{K_{fl}}}}_{\text{Fluid term}} \quad (2.4)$$

Notice that the dry-rock term has a similar expression to that of an elastic isotropic medium (equation 2.2.a) and is independent of pore fluid, while the fluid term changes as

the pore-fluid content changes. Since fluid does not support any shear movement, the S-wave velocity equation is analogous to that of an elastic isotropic medium: $\beta = \sqrt{\frac{\mu}{\rho}}$.

The density, however, does affect the S-wave velocity as the pore fluid changes and is given by

$$\rho = \rho_{\text{ma}}(1 - \phi) + \rho_{\text{fl}}\phi, \quad (2.5)$$

where ρ_{ma} and ρ_{fl} are the matrix and pore fluid densities (in gm/cm³),

and ϕ is the rock porosity.

In principle, we can use Gassman's equation to link estimates of velocity (or reflection coefficients) to obtain information about the reservoir fluid.

II.3 The effect of Poisson's ratio on reflection coefficient

Koefoed (1955) calculated the P-wave reflection coefficients of a plane wave reflected from an interface of two elastic media valid for angles of incidence between 0 to 30 degrees. By using the formula that was derived by Knott (1899), Koefoed (1955) varied the Poisson's ratio of the two media and concluded that "*...the differences in Poisson's ratio of rock strata as they occur in nature would affect the change of the reflection coefficient with the angle of incidence to an extent that would be of practical significance in seismic prospecting.*"

A comprehensive verification of Koefoed's (1955) statement was published 29 years afterward by Ostrander (1984). Using a hypothetical gas-sand model with Poisson's ratio of 0.1 combined with some examples from actual field data with known well control information, Ostrander (1984) restated the strong influence of Poisson's ratio on changes in reflection coefficient with angle of incidence. In addition, he also suggested the importance of seismic data processing flows to preserve relative amplitudes on CDP gathered traces before stacking.

II.4 Linear approximation of Zoeppritz's equation

Zoeppritz's equations are implicitly coupled to the various rock properties of interest and do not provide any direct interpretive insight to the AVO behavior. For this reason, linear approximations of Zoeppritz's equation were developed to explicitly relate rock properties thereby providing interpreters with a more direct understanding of AVO anomalies.

II.4.1 Bortfeld's approximation: The fluid and rigidity terms

Bortfeld formulated the early reflection and transmission coefficient approximations of Zoeppritz's equation in 1961. He derived linear equations that he claimed were accurate to within a few degrees of the critical angle. The P-wave reflection coefficient is given as:

$$RC(\theta) \approx \frac{1}{2} \ln \left[\frac{\alpha_2 \rho_2 \cos \theta}{\alpha_1 \rho_1 \cos \theta} \right] + \left(\frac{\sin \theta_1}{\alpha_1} \right)^2 (\beta_1^2 - \beta_2^2) \left[2 + \frac{\ln(\rho_2 / \rho_1)}{\ln(\beta_2 / \beta_1)} \right]. \quad (2.6)$$

The diagram shows two horizontal double-headed arrows. The first arrow is positioned under the first term of the equation, $\frac{1}{2} \ln \left[\frac{\alpha_2 \rho_2 \cos \theta}{\alpha_1 \rho_1 \cos \theta} \right]$, and is labeled "Fluid term". The second arrow is positioned under the second term, $\left(\frac{\sin \theta_1}{\alpha_1} \right)^2 (\beta_1^2 - \beta_2^2) \left[2 + \frac{\ln(\rho_2 / \rho_1)}{\ln(\beta_2 / \beta_1)} \right]$, and is labeled "Rigidity term".

Bortfeld's equations show that two major terms influence the value of reflection coefficient from an interface. The first, or fluid term is the equivalent to the reflection coefficient from a fluid-fluid interface which does not support any shear particle movement ($\beta_1 = \beta_2 = 0$). Interestingly, Bortfeld's equation shows that the second term, the rigidity-term for both gas-saturated and water-saturated sand models, are almost identical. The reason is simply because the rigidity term depends primarily on β which is independent of the pore-fluid content. Thus, the differences in AVO response differences between gas and water as pore fluid content are solely determined by the first or fluid term.

II.4.2 Aki and Richards' approximation: Velocities and density terms

Bortfeld's (1961) formula was further refined by Richards and Frasier (1976), and continued by Aki and Richards (1980). The approximation they composed is attractively written in three terms that emphasizes the contribution of variations in rock properties, the first involving density ($\Delta\rho$), the second involving P-wave velocity ($\Delta\alpha$), and the third involving S-wave velocity ($\Delta\beta$). The equation for the reflection coefficient from an interface separating two elastic media is described as

$$RC(\theta) \approx \frac{1}{2} \left(1 - \frac{4\beta^2}{\alpha^2} \sin^2 \theta \right) \frac{\Delta\rho}{\rho} + \frac{1}{2 \cos^2 \theta} \frac{\Delta\alpha}{\alpha} - \frac{4\beta^2}{\alpha^2} \frac{\Delta\beta}{\beta} \sin^2 \theta, \quad (2.7)$$

where $\Delta\alpha = \alpha_2 - \alpha_1$, $\Delta\beta = \beta_2 - \beta_1$, $\Delta\rho = \rho_2 - \rho_1$,

$$\alpha = (\alpha_1 + \alpha_2)/2, \beta = (\beta_1 + \beta_2)/2, \rho = (\rho_1 + \rho_2)/2.$$

II.4.3 Shuey's approximation: The Normal Incidence and Poisson Reflectivity

Whereas the earlier approximations involved α , β , and ρ , Shuey (1985) published a closed form approximation of Zoeppritz's equations which involved α , ρ , and σ , or Poisson's ratio. This work motivated Verm and Hilterman (1995) to rearrange Shuey's equation so that it emphasizes the rock-property dependence on incident angle, with each term becoming important over a different range of incidence angles:

$$RC(\theta) \approx \frac{1}{2} \left(\frac{\Delta\alpha}{\alpha} + \frac{\Delta\rho}{\rho} \right) \left(1 - \frac{4\beta^2}{\alpha^2} \sin^2 \theta \right) + \frac{\Delta\sigma \sin^2 \theta}{(1-\sigma)^2} + \frac{1}{2} \frac{\Delta\alpha}{\alpha} \left(\tan^2 \theta - \frac{4\beta^2}{\alpha^2} \sin^2 \theta \right). \quad (2.8)$$

Change of acoustic impedance strongly influences the near-angle response (1st term), while variation of Poisson's ratio strongly influences the mid-angle response (2nd term), and P-wave velocity dominates the far-angle response (3rd term).

Verm and Hilterman (1995) formulated a further simplification of this approximation equation under the assumptions that V_p/V_s ratio ≈ 2 (or $\sigma \approx 1/3$) and for angles less than 30° such that the far angle term can be dropped:

$$RC(\theta) \approx NI \cos^2\theta + PR \sin^2\theta \quad (2.9)$$

where the normal incidence term, NI, is given by

$$NI = \frac{\alpha_2 \rho_2 - \alpha_1 \rho_1}{\alpha_2 \rho_2 + \alpha_1 \rho_1},$$

and the Poisson reflectivity term, PR, is given by

$$PR = \frac{\sigma_2 - \sigma_1}{\left(1 - \frac{\sigma_2 + \sigma_1}{2}\right)^2}.$$

Notice here that as the angle of incidence increases that the NI term acts to decrease the amplitude response while the PR term which (becomes more dominant) acts to increase the amplitude response.

Since the assumption of $\sigma = 1/3$ reduces the generalization of this simplified Shuey's equation (Verm and Hilterman, 1995), Hilterman (2001) obtained:

$$\begin{aligned} NI(1 - .67 \sin^2\theta) & \quad \text{for } \sigma = 0.40, \\ NI(1 - 1.3 \sin^2\theta) & \quad \text{for } \sigma = 0.25, \\ NI(1 - 1.6 \sin^2\theta) & \quad \text{for } \sigma = 0.15, \end{aligned} \quad (2.10)$$

to replace for other values of σ , the first or NI term of the equation in order to better approximate the exact Zoeppritz's approximation.

Chapter III

POROUS CHANNEL SAND PHYSICAL MODEL EXPERIMENT

The technology of seismic modeling, both numerically and physically, has played an important role in many areas of seismology. Synthetic models help researchers and interpreters to better understand the seismic response from a suite of earth models, which can then be compared to the real field data. Numerical modeling techniques provide us with a means of defining the earth model, acquisition geometry, signal attributes, and other desired events. On the other hand, although physical modeling parameters are also user-defined, they are subject to experimental limitations in electronics, positioning, and material behavior or ambient laboratory temperatures and pressures. Most importantly, physical models must be built - either milled, ground, cast, carved, sintered, glued, or otherwise fashioned into the desired earth structure. Consequently, choosing suitable materials in a physical model experiment is crucial to obtaining appropriate synthetic data.

Unlike ray-tracing, but like grid based wave equation numerical modeling, physical modeling does not allow us to specify user-desired events. Given random heterogeneity (flaws) throughout the model, as well as coupling and electronic noise, synthetic seismic

data provided by physical model experiment may represent the signal to noise level of actual field data better than numerical methods. At present, 3-D multi shot elastic numerical modeling is so computationally expensive that it is the focus of a major computer research effort at National Laboratories (House et al., 2000). Contrary to the numerical modeling computational demand, physical modeling techniques can produce 3-D multi shot elastic synthetic data without any significant computational constraint. The single receiver configuration used in this thesis allows us to collect one vertically stacked trace each second, or some 40,000 traces per day.

While physical models have been used in 3-D seismic illumination studies for more than 25 years, very little has been done in simulating porous reservoirs. In this thesis, I will exploit a porous media physical model as a tool to understand seismic acquisition for time-lapse seismic analysis.

In this chapter, I will describe a physical model simulating a simple sand channel filled with a permeable material. I will then inject a fluid through this channel in order to better calibrate the ability of seismic attributes to detect a moving front.

III. 1 Constructing the model

III.1.1 Porous channel sand

Workers in rock physics have constructed porous sand models in several research laboratories. Gik (1997) used foam plastic grains distributed in resin to imitate the pores. Molyneux and Schmitt (1999) mixed glass beads with quartz sand for a compressional-wave velocity study in attenuating media. Winkler (1983) compared the velocity dispersion and attenuation factor of some sandstone samples with more homogeneous sintered glass beads. Continuing this work, sandstone analogs made from sintered glass beads with porosity ranging between 1 % and 43 % were tested to establish a relationship between ultrasonic velocity and porosity (Berge et al., 1995). Sherlock (1999) used sorted sand to study the influence of fluid migration pathway in combination with buoyancy and hydrodynamic flow, which finally can be mapped in 3-D reservoir images.

Following Berge et al. (1995), I expect sintered glass beads to provide an excellent means of conducting a time-lapse seismic modeling experiment. I am able to control the porosity and permeability by choosing bead size and heating history. Baking the glass beads in a kiln at 700°C for 15 minutes creates good contact or cementation between the grains while maintaining connectivity between the pores. Despite the imperfect grain size scaling that falls around $a = 20$ cm (after applying the 10,000:1 scale), using another material with smaller grain size gives rise to strong capillary effects we do not wish to model.

The specifications of glass beads used are as follows:

Product name : Glas-Shot

Composition : SiO₂ (71-74%), Na₂O (12-15%), CaO (8-10%), MgO (1.5- 3.8%),
Al₂O₃ (0.2-1.5%), K₂O (0-0.2%), Fe₂O₃ (0-Trace).

Density : 2.42 – 2.50 g/cm³

Melting temperature : 730 °C

Manufacturer : Cataphote Inc., Jackson, MS, USA.

(Website: www.cataphote.com)

One of the uses of glass beads is in the construction of simple cylindrical filters used in the beverage processing industry. Fusing glass beads into the shape of a channel has its own complexities in that the sintered beads are too rigid to bend and too brittle to grind. Instead, I collaborated with faculty and students in the University of Houston Art Department, who have experience in casting a wide variety of ceramics and clays. We first constructed a channel structure with clay (Figure 3.1). Note that two thinner, shallower river channels join to become a wider, thicker channel at the lower end. We used this clay model to build a ceramic mold (Figure 3.2). This mold was then filled with glass beads. Note here also that there are wide varieties of ceramics in which each having different temperature capabilities. Choosing the proper ceramic for my mold is essential to avoiding cracks or breaks during the glass bead sintering process, particularly if someone wishes to reuse the mold for future models to allow studies of variable porosity.

Designing the channel shape at the 1:10,000 physical model scale requires consideration of the seismic wave propagation characteristics to be studied. To distinguish the top and bottom of the channel, I designed the channel thickness in the center to be greater than a quarter wavelength of the ultrasonic signal (tuning resolution). Hence, for an ultrasonic signal with 300 kHz dominant frequency propagating in a medium with a velocity of 2100 m/s, the sintered glass beads minimum thickness required to avoiding the tuning effect is approximately 1.75 mm. Even though the channel has 10 mm thickness, its syncline shape will gradually decrease the thickness to become very thin when it gets to the edge. Thus, this thin edge is expectedly subject to the tuning effect phenomenon. The Fresnel zone must be taken into account in understanding the limits to the horizontal resolution. The Fresnel zone radius that equals $\frac{1}{8}$ wavelength corresponds to 87.5 m. A channel width of 400 m will adequately satisfy this horizontal limit.

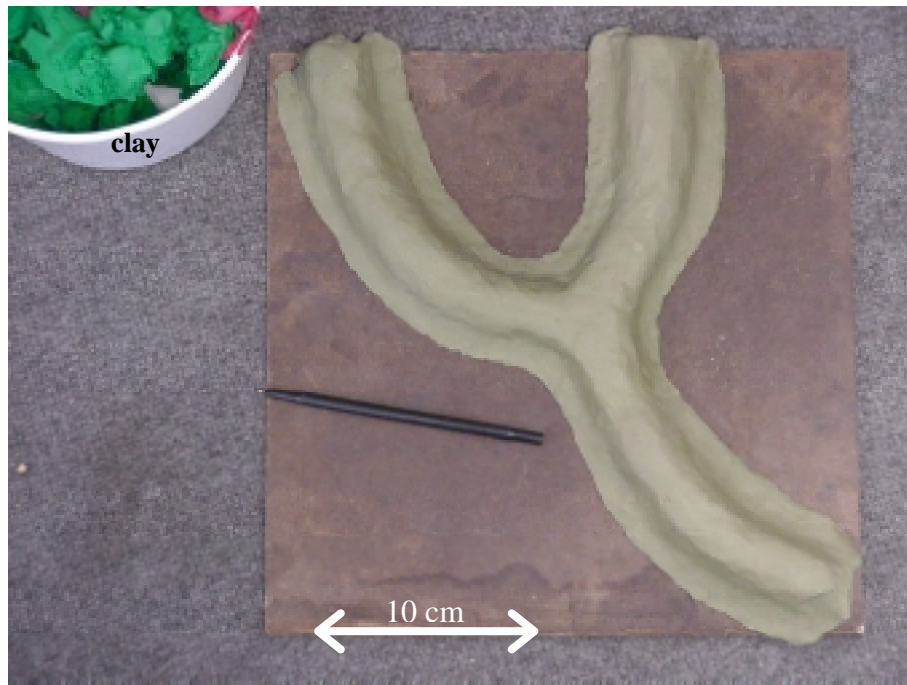


FIG. 3.1. A channel design made of clay (upside down).

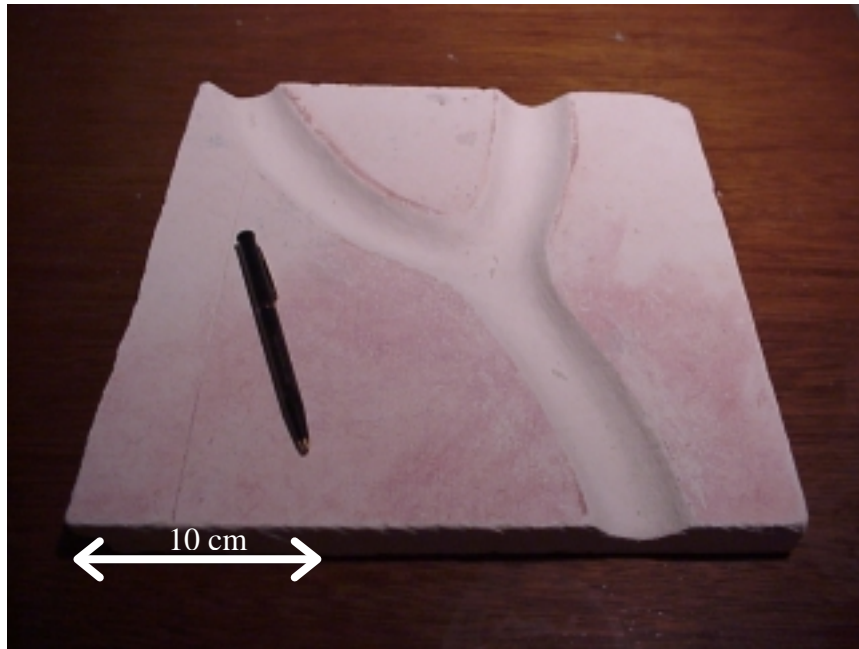
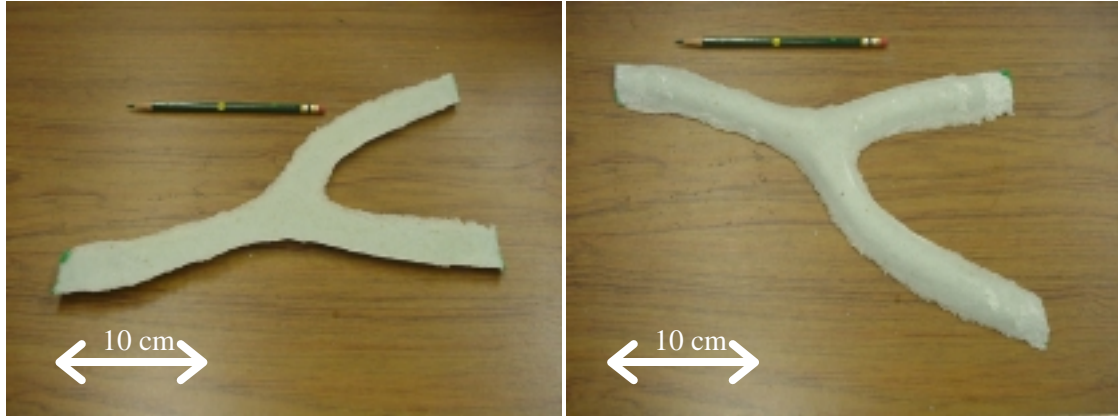


FIG. 3.2. Ceramic mold with channel structure.

In order to experimentally determine the sintering temperature of glass beads I packed a 3.75 cm diameter 6 cm long tube with glass beads, placed it in the kiln and gradually increased the temperature up to the approximate sintering temperature, then held the temperature for a different time periods. Samples subjected to each sintering temperature and time period were evaluated for solidity and permeability. The ideal sintered glass bead model should support its own weight, not crumble at the surface, yet maintain permeable connection between the pores. I found these criteria were met when the temperature was set at 700°C, held there for 15 minutes, and then slowly decreased over a period of approximately 15 hours (Figure 3.3). This time-consuming slow temperature increment and decrement process is essential in order to prevent large temperature gradients which may cause an inhomogeneous sintering condition between the outer and inner part of the glass bead channel.



(a)

(b)

FIG. 3.3. The sintered glass beads channel seen from the (a) top and (b) bottom.

Physical properties measurements of the sintered glass beads are essential to our calibration effort. I measured compressional and shear velocities using contact transducers. The average of compressional and shear velocities for six independent dry and wet sintered glass bead measurements are:

Fused glass bead	Vp (m/s)	Vs (m/s)	ρ (gm/cm³)	Poisson's ratio
Dry	1,742 \pm 196	1,221 \pm 54	1.7	0.02
Wet	2,540 \pm 278	1,095 \pm 49	2.1	0.38

Table 3.1. Physical properties of dry and wet sintered glass bead model.

Laboratory measurement of density of glass beads with the value of 2.56 gm/cm³ falls agreeably within the range from the manufacturer's specification. While for gas-filled and glycerol-filled sintered glass beads, the measured densities are 1.7 and 2.1 gm/cm³ respectively. Laboratory measurement of the mass and volume of dry and wet sintered glass beads gives us a porosity of 33.4%.

III.1.2 Embedding the channel in a 'shale' matrix

Physical modeling experiments provide us a means of testing a method or theory. In most cases, models are built as simple as possible to eliminate phenomena that do not contribute to the immediate experimental purpose, other than adding more difficulties during the model construction and data interpretation. The purpose of my experiment is to evaluate seismic attributes for a time-lapse experiment. For this reason, we chose a simple stratigraphic vs. a complex structural model. We also buried our model deep enough in our water tank to avoid interference from surface multiples.

In order to clearly isolate the effects of fluids in a porous medium I embedded my 'sand' channel between two isotropic homogeneous 'shale' layers at the top and the base of the channel. The top layer of clear epoxy has $V_p = 2,468$ m/s, $V_s = 1,100$ m/s, $\rho = 1.15$ gm/cm³. The bottom layer of black resin has $V_p = 2,545$ m/s, $V_s = 1,100$ m/s, $\rho = 1.36$ gm/cm³. The Poisson's ratio of the two layers are 0.38 and 0.39, consistent with that of shales.

I built the model upside down, starting from the top layer and working my way up to the bottom. A mixture of clear epoxy E-1676 and catalyst E-10C with 1:1 weight ratio was poured into a 30 x 30 cm² metal mold, thin layer by thin layer to achieve the desired height. Since we want the channel sand to sit in a dipping structure, at a certain time the mold was tilted by 7.3° while letting the epoxy mixture solidify. After attaining the desired dipping block of clear epoxy, the channel sand made of sintered glass beads

needs to be welded firmly to the epoxy. While a very thin layer of epoxy would act as the glue, the sintered glass beads must not be dropped immediately after the thin epoxy layer is poured, otherwise the fluid epoxy will invade the glass bead pores and solidify, thereby reducing the channel porosity and permeability. To prevent filling the pores, I first sealed the sintered glass bead channel surfaces by spraying them with clear acrylic thereby forming an impermeable thin layer. I also delayed dropping the sintered glass bead channel until the thin epoxy was partially cured and had a sufficiently high viscosity to prevent invasion into the pores.

I employed the technique with the second layer, black resin, made of Stycast 2741 black epoxy resin and black catalyst 15 LV with 1:1 weight ratio. This step was even more tedious than the first because the black resin harden at a much slower rate than clear epoxy. Additionally, since during model construction the black resin would lie on top of the channel, the weight of black resin would add the additional pressure onto the glass beads pores. I, therefore, decided to preserve the porosity and permeability of the sintered glass beads by painting the surface with black resin. I repeated this painting process 10 times while letting the thin layer dry between applications. Once the impermeable layer is established, a thick layer of black resin can sit properly on top of the channel without disturbing the pores. At all times during these procedures, care must be taken not to crack the fragile sintered glass bead channel.

A step before pouring black resin on top of the model is to ensure that all ends of the channel are kept open for allowing fluid injection afterwards. For this reason, I covered

the channel ends with clay so that I could remove it easily after the model cured. This clay should perfectly cover the entire channel ends to guarantee there is no chance of leak when I start pouring a thick layer of black resin. Figure 3.4 shows the blueprint and the entire model after the black resin solidified.

III.1.3 Fluid Injection Apparatus

Simulation of marine acquisition in this modeling experiment requires the entire model to be immersed in the water tank. Therefore, it is necessary to design a method with a low-risk plan for sealing the channel sand from any association with the surrounding (water) medium so that gas/fluid in the channel pores remain undisturbed, while at the same time allowing me to inject fluid into the channel in several stages thereby simulating a time lapse experiment.

I attached a transparent plastic hose of 2.5 mm diameter to the three ends of the channel by using a water-impermeable silicon-based adhesive (Marine Goop), with the free hose ends being stretched above the water level. The adhesive also acts as the channel end seal from the outside medium. This arrangement (Figure 3.5) allows us to inject fluid from one end of the hose using a syringe while letting the other hose ends open so that the pore air (or liquid) may escape.

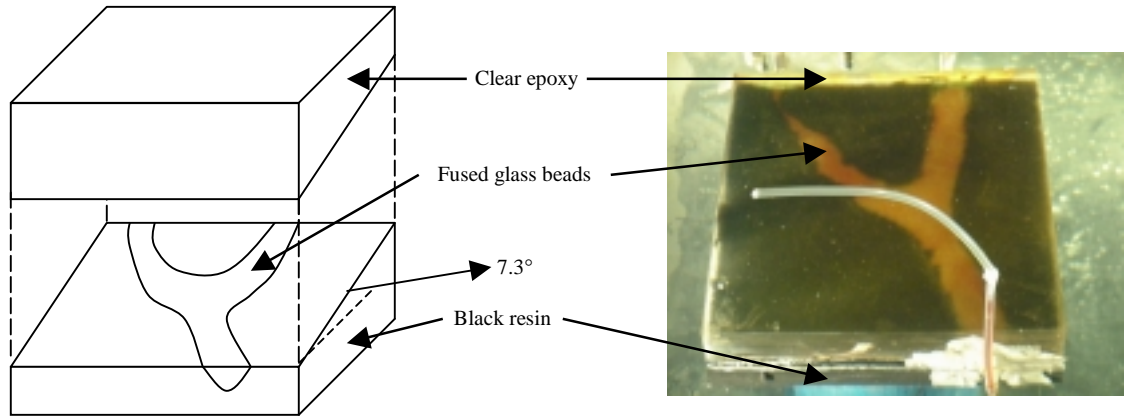


FIG. 3.4. Schematic and digital photo of the physical model .

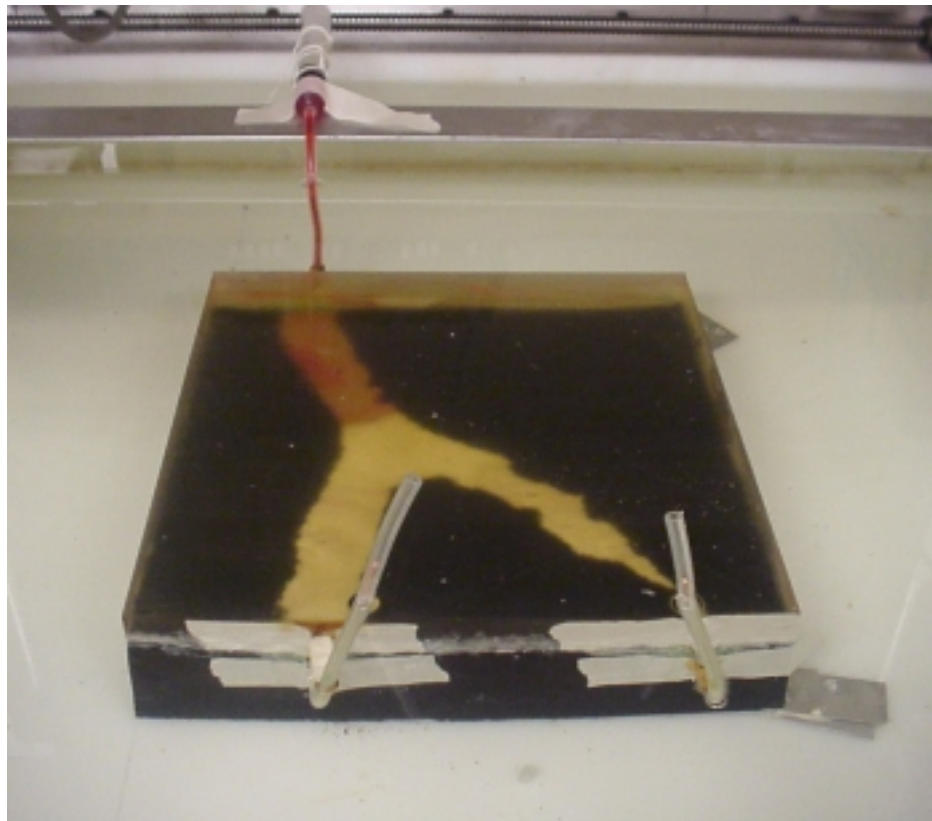


FIG. 3.5. Fluid injection method using implanted hoses and a syringe.

III.1.4 Selecting the Pore Fluid

Choosing which fluid to inject into the channel is also subject to scale model constraints. Initially I plan to run the time-lapse simulation backwards from the real earth CO₂ injection case, starting with a gas-filled channel that is gradually charged with fluid, but maintaining a fixed fluid front during a week of data collection. For this reason, it is important to select a fluid that sufficiently viscous to minimize osmosis through the channel.

I evaluated three fluid candidates, water, vegetable oil, and glycerol, in terms of osmosis through the sintered glass beads. To do so, I soaked small (5 mm) pieces of sintered glass beads in water, vegetable oil, and glycerol for the same period of time and then measured how far each fluid moved upward through the sintered glass beads as a function of time. Figure 3.6 shows the final state of this experiment and leads us to choose glycerol as the pore fluid. Of the three fluids, the glycerol fluid-front shows the sharpest boundary between dry and wet areas. The characteristics of glycerol are as follows:

Composition : HOCH₂CHOHCH₂OH

Density : 1.25 gm/cm³

Color : Clear

To distinguish dry sintered glass beads from the one filled with glycerol, I added a few drops of red food color to the glycerol, such that the boundary of wet and dry channel can be visually recognized through the clear epoxy thereby serving as a control.

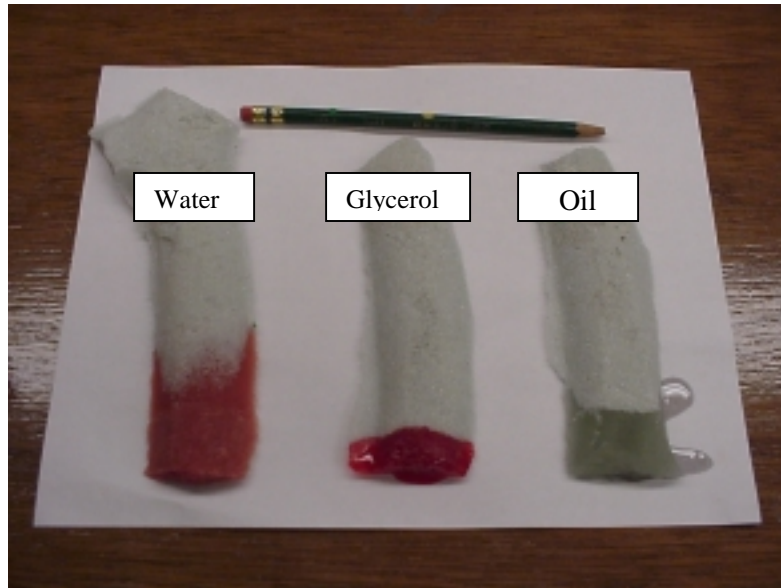


FIG. 3.6. Sintered glass beads after having been dipped for 5 seconds in water, glycerol, and cooking oil. Glycerol moves slower than the other fluids, and maintains a sharp boundary to for use in our discrimination experiments.

III.2 Acquisition Geometry

I simulated marine data acquisition in my time-lapse experiment in the AGL acoustic (water) tank using Edo Acoustic SN 327 spherical transducers as both the source and receiver. A calibration test of these transducers is described in Appendix A. Although the model is relatively small, acquiring data in the acoustic tank allows me to avoid surface multiples which would complicate data processing and interpretation.

I collected 47 lines of single azimuth data separated by 50 m, giving a crossline coverage of 2300 m. Each line has 116 CDP gathers with 20 m between adjacent CDP points. A

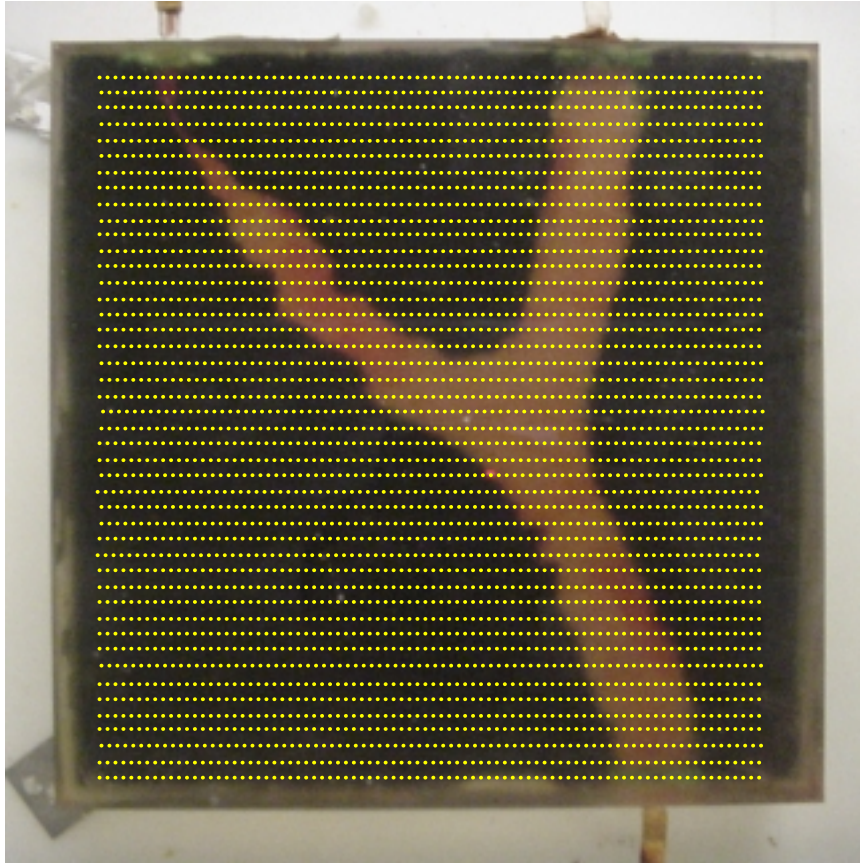


FIG. 3.8. CDP coverage over the channel model. All CDPs have a fixed 37 folds.

Most of the data in this experiment were not vertically stacked and suffered from noise from elevators, lights, electronics, air conditions, traffic from I-45, and students changing classes in our 7-story building. To improve the signal to noise ratio, I collected and then vertically stacked 50 traces per source-receiver pair location. The acquisition time using our current physical model software increases dramatically, so that given my time constraints I only had time to re-acquire a 2-D vertical stack acquisition line rather than

reshooting the entire survey (Figure 3.9). I acquired these two 2-D datasets of two channel conditions, wet and dry. Having these two 2-D lines with higher signal to noise ratio are preferable than only relying on 3-D datasets with low signal to noise ratio, especially when AVO and coherency analysis are to be conducted that requires high-precision trace amplitudes.

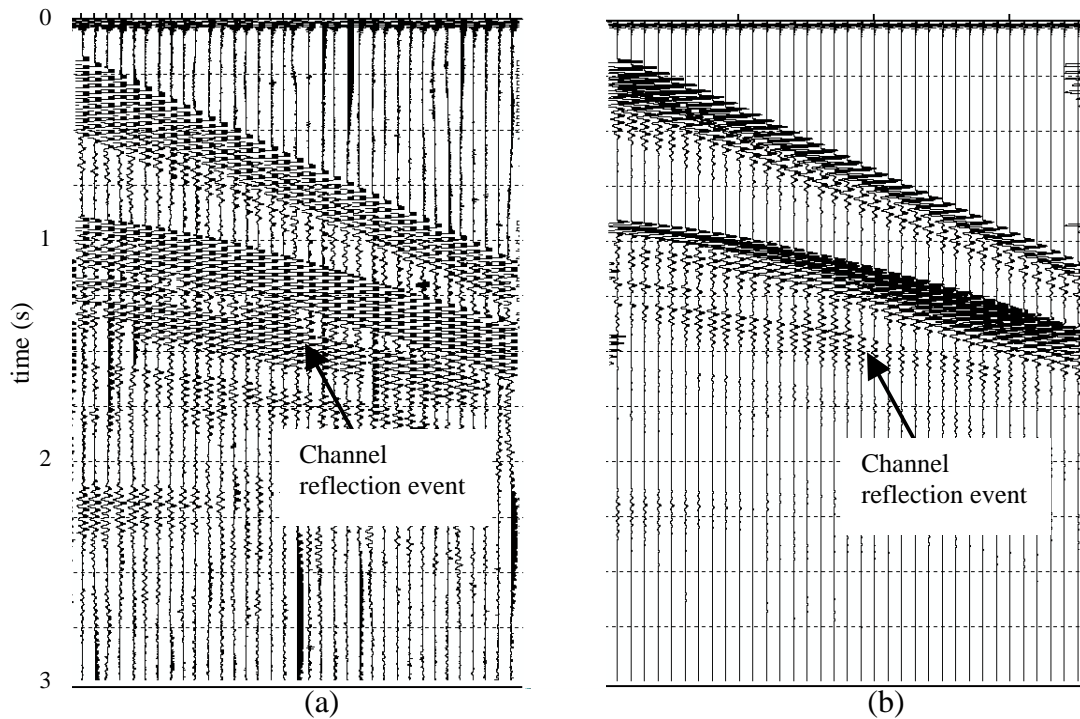


FIG. 3.9. A CDP gather with a vertical stack of (a) one, and (b) fifty traces. The data on the left is representative of most of the data presented in this thesis.

I also attempted to reduce the strong direct transmission signal amplitudes. Placing a rubber pad between the source and receiver transducers resulting in a decrease of 50% of the direct transmission amplitude while not affecting the other signals (Figure 3.10).

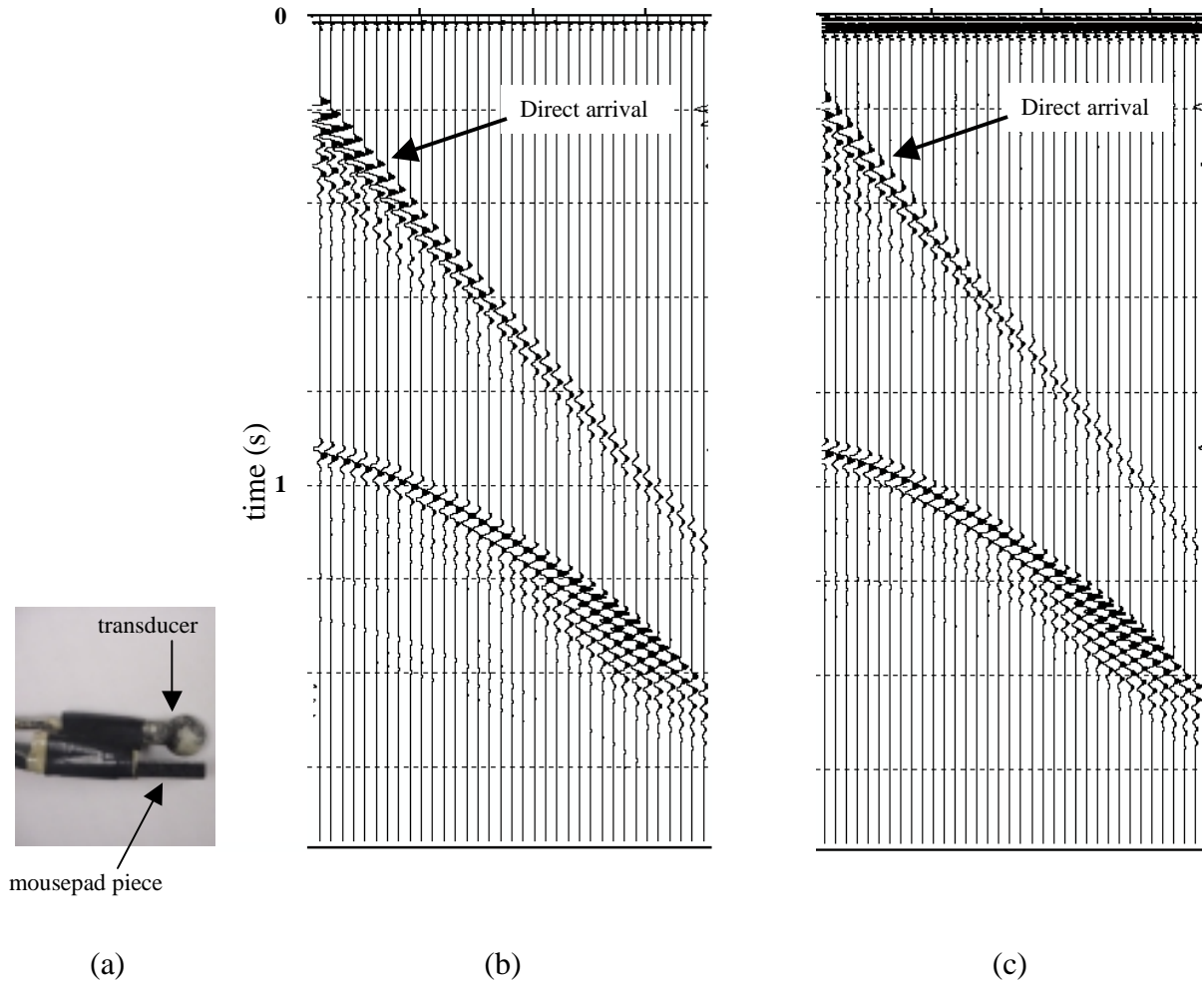


FIG. 3.10. (a) Use of an absorbing barrier (mousepad) to reduce the energy of direct transmission from source to receiver. (b) The seismic section recorded without the pad and (c) with the pad inserted between the source and receiver transducers.

Chapter IV

TIME-LAPSE DATA PROCESSING

IV.1 Assessing data quality

Determining the quality of my physical model data is essential in ascribing any differences between the time-lapse datasets due to changes in fluid product rather than variations in my experimental apparatus. In the previous chapter, I described how I acquire time-lapse physical model data. In this chapter, I will examine the data quality from each dataset in light of time-lapse interpretation.

IV.1.1 Energy irregularity between traces

The most obvious problem with data acquisition is amplitude preservation. In Figure 4.1 we note that traces comprising CDP gather 24, 25, as well as some traces comprising CDP gather 26 have only 25% of the amplitude of CDP gathers 27 and 28 and the further offset traces of CDP 26. After careful analysis, we identified a grounding deficiency in our DC pre-amplifier power supply. Fortunately, this amplifier error is easily corrected by a simple, constant, scaling parameter that is applied to those data collected during the time of the grounding problem (Figure 4.2).

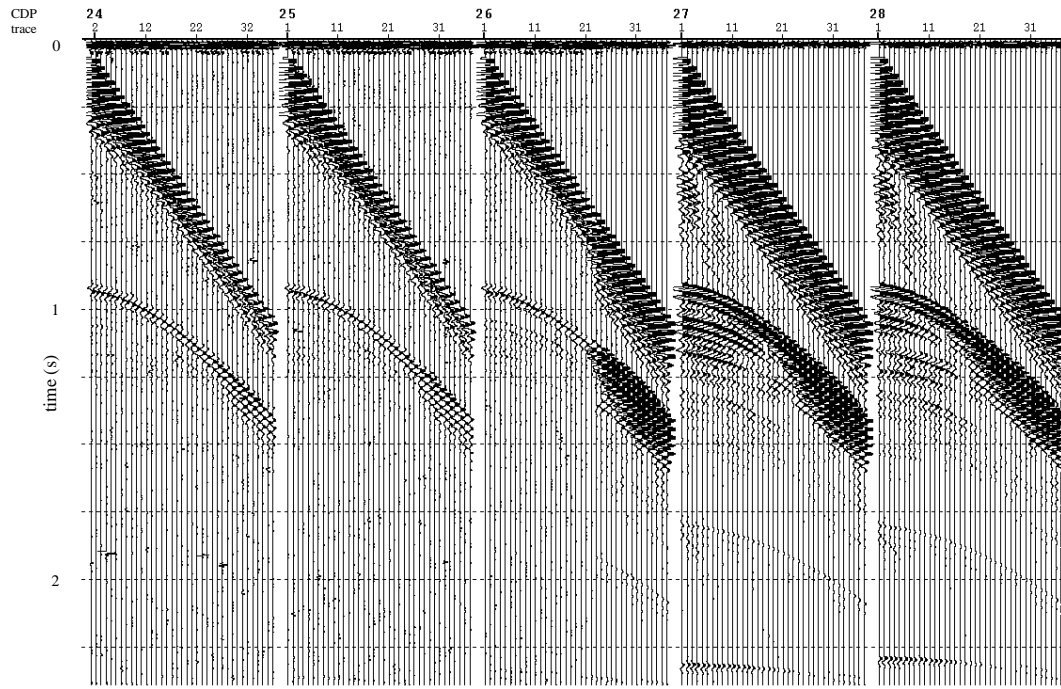


FIG. 4.1. Amplitude irregularity in the raw data. Note that CDPs 24 and 25 have only 25% the amplitude of CDPs 27 and 28.

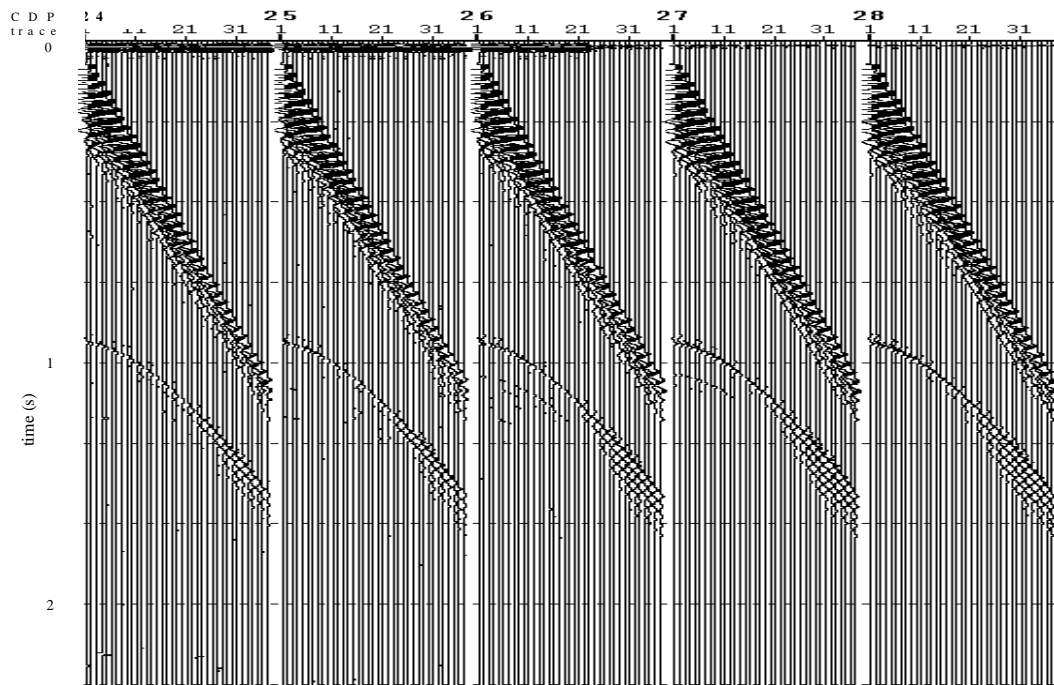


FIG. 4.2. Amplitude correction of the data shown in Figure 4.1 by simple scaling.

IV.1.2 Signal-to-noise ratio

Electrical and mechanical devices including fans, generators, elevators, air conditioners, as well as our recording system itself create noise in physical modeling experiments.

Sometimes the source of the noise is obscure. An insecure BNC connector can generate occasional noise burst in the data (Figure 4.3). The tape-based data acquisition system used in this experiment did not allow for QC of intermediate results during the six days of acquisition. While I have designed a better wiring connection to avoid such noise bursts, we need to design our new Labview-based system to routinely check for their occurrence and alert the system operator.

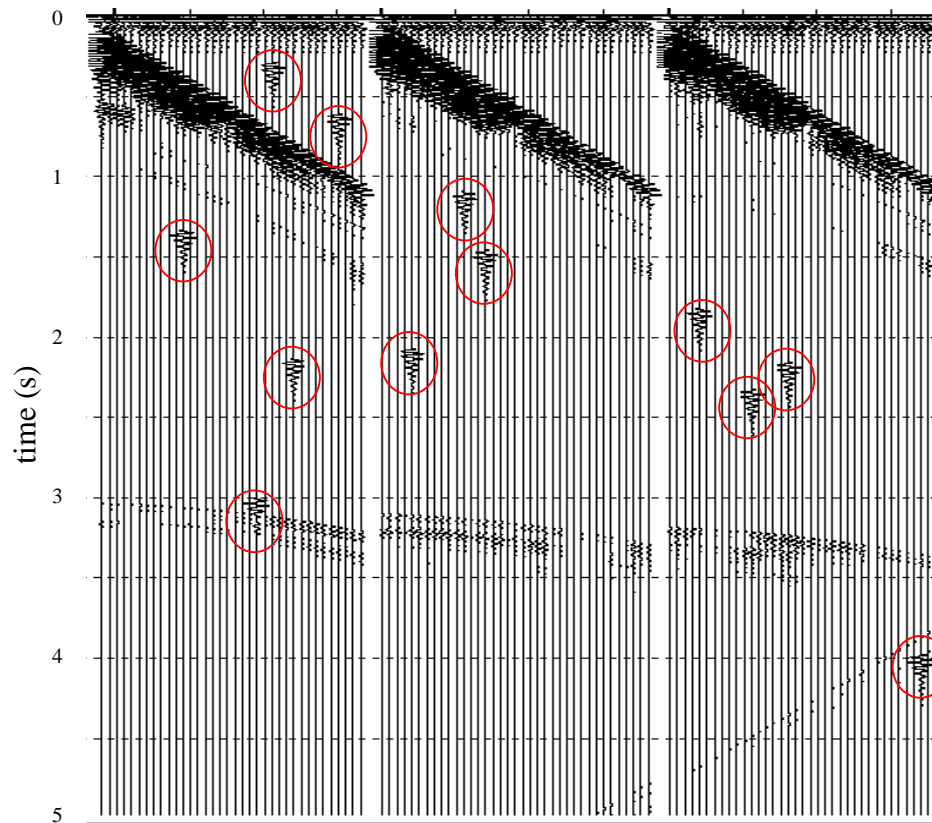


FIG. 4.3. Noise bursts (circled) in the data due a loose BNC connection.

IV.1.3 Geometry

In Chapter 3, I described that I collected 47 parallel lines consisting of 116 two-dimensional CDP gathers per line, resulting in a rectangular grid of CDP bins, with the center of each bin beneath each zero-offset point. One disadvantage of this acquisition geometry is the lack of source/receiver pairs having azimuths beyond the in-line direction (see Figure 3.7).

IV.2 Data processing

My data processing flow is simple, consisting of amplitude correction prior to velocity analysis, pre-stack common-offset time migration, and stacking.

IV.2.1 Transducer directivity and geometrical spreading correction

Preserving relative-amplitude is a major concern during data processing for AVO. First, I must calibrate the amplitude with the transducer directivity factor. The scaling factor for each trace is linearly interpolated from the angle directivity curve (see Appendix B). In order to calculate the emergence angle necessary for the transducer directivity correction (see Appendix A, Figure A.4), I built a simple layer-cake model representing a single acquisition line, and traced rays using software provided by GX Technology (Figure 4.4). The dipping structure of the actual model that bends the reflection raypaths has been included.

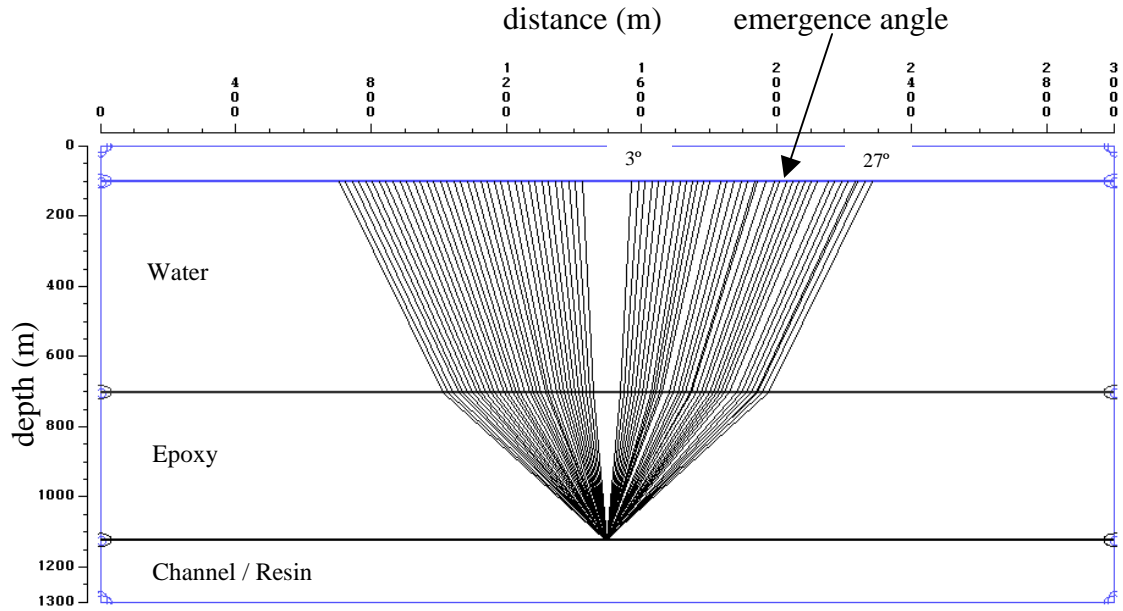


FIG. 4.4. Ray-tracing modeling of the channel reflection predicts emergence angles of 3° to 27° to be used in transducer calibration.

Next, I apply a geometrical spreading correction (Yilmaz, 1987) using the equation:

$$S(t) = \frac{\bar{V}(t).t}{\bar{V}(t_{\text{final}}).t_{\text{final}}} \quad (4.1)$$

where $\bar{V}(t)$ = average velocity at time t (m/s),

\bar{V}_{final} = final average velocity (m/s),

t_{final} = final data length (s).

The equation above was implemented on all datasets using the time-velocity pairs obtained during velocity analysis. Figure 4.5 shows an example of common shot gather before and after the correction.

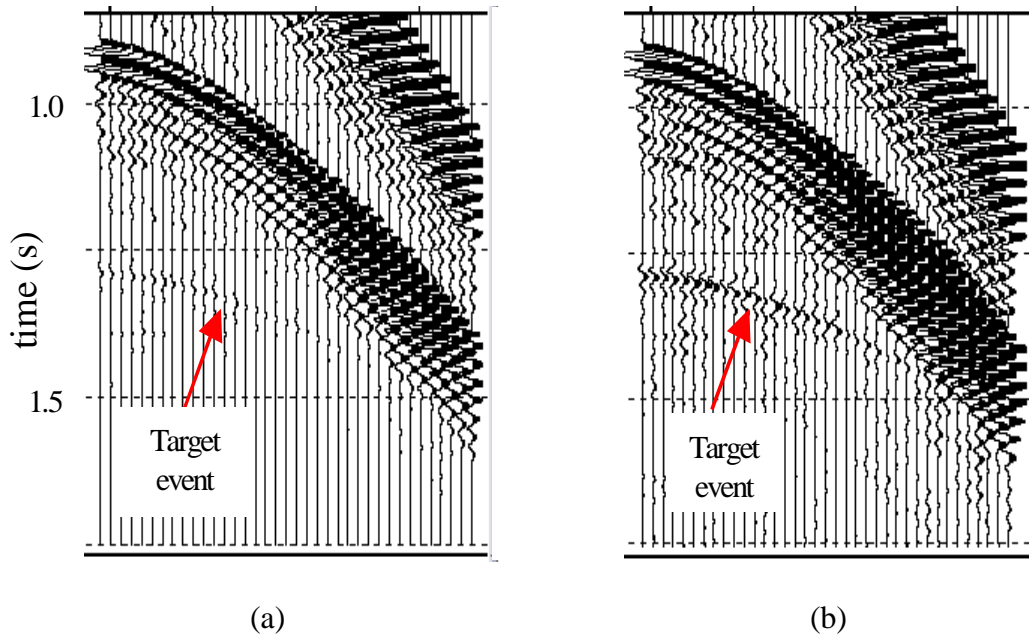


FIG. 4.5. Data (a) before and (b) after geometrical spreading correction given by equation 4.1.

IV.2.2 Velocity analysis, NMO, and stacking

The seismic acquisition lines were designed to be roughly perpendicular to the channel feature. In addition, the model was constructed to have only moderate structural dip, such that conventional velocity analysis is adequate. The only velocity picking difficulty encountered is when the reflections approach diffraction events from the model edges and fluid injection hoses. However, sorting the data into common offset gathers in the crossline direction allows event recognition of the dip (Figure 4.6).

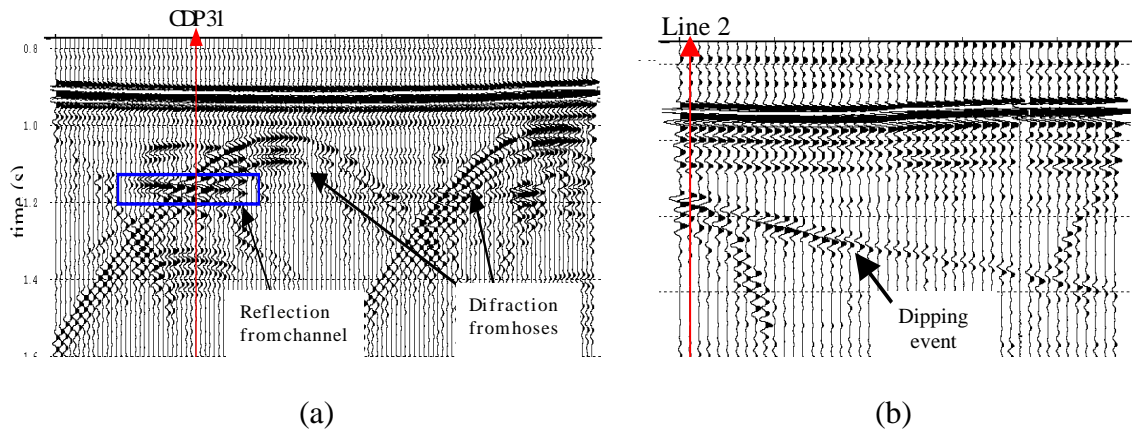


FIG. 4.6. Reflection event on (a) line 2 can be easily identified using (b) the crossline at CDP 31. The red line indicates where the subline and crossline intersect.

The velocity function derived for the first time-lapse dataset cannot be applied to subsequent datasets because of slight differences in source and receiver positioning (see section IV.1.3). Consequently, NMO corrections were done using a unique velocity analysis for each time-lapse dataset, followed with mute and stacking.

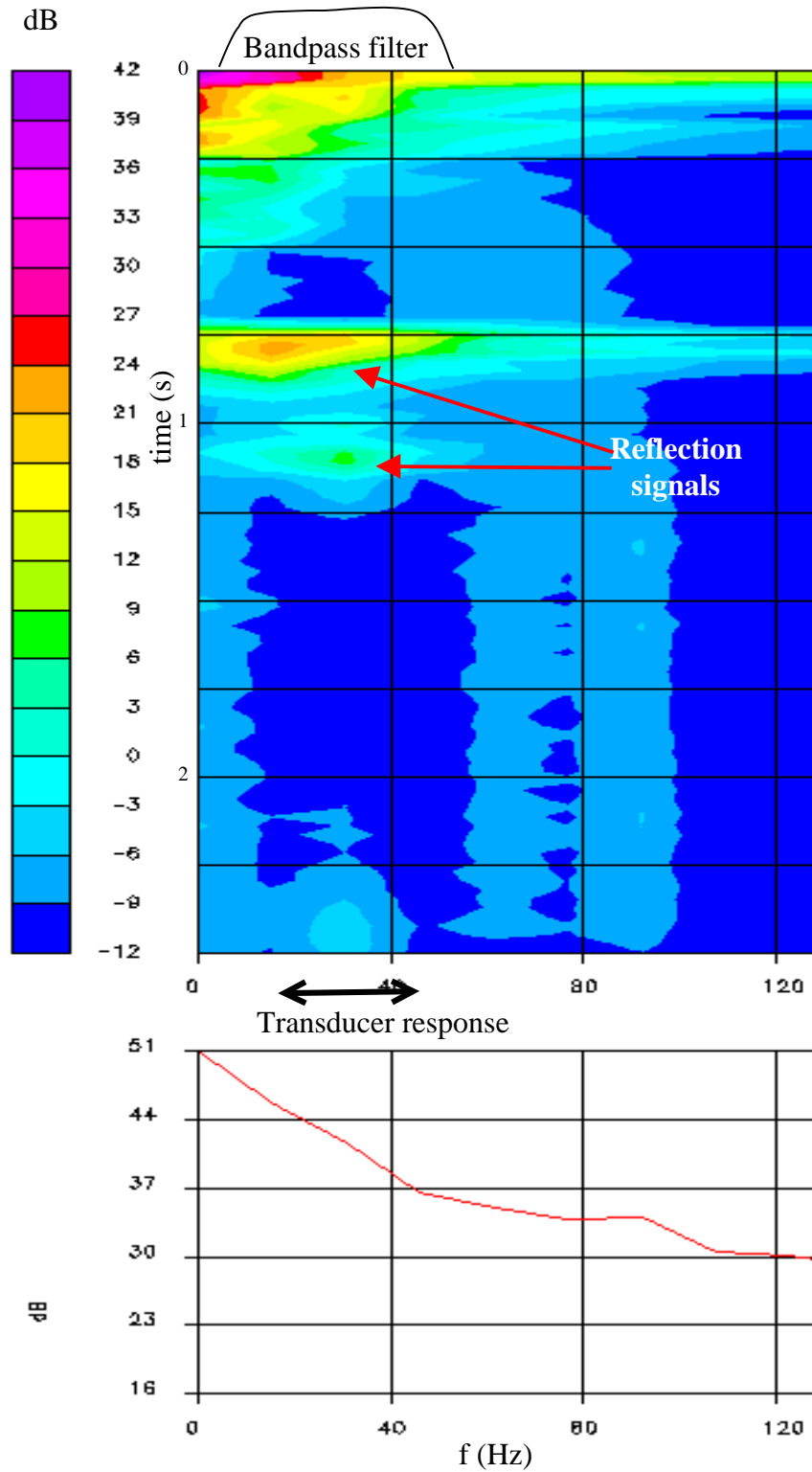


FIG. 4.7. Spectral analysis of a near offset gather shows noise at around 0 Hz and between 50 to 100 Hz.

IV.2.3 Filtering

Having calculated the transducer bandwidth and resonance (Appendix A), I can search for and eliminate noise that falls outside these values. In Figure 4.7, we note significant noise around 0 Hz and between 50 to 100 Hz. The low frequency noise comes from a grounding deficiency, and the high frequency noise comes from unknown electrical or mechanical devices surrounding the physical modeling tank. Applying a trapezoidal bandpass filter of 5-10-45-50 Hz to the stacked data effectively suppresses the noise level (Figure 4.8).

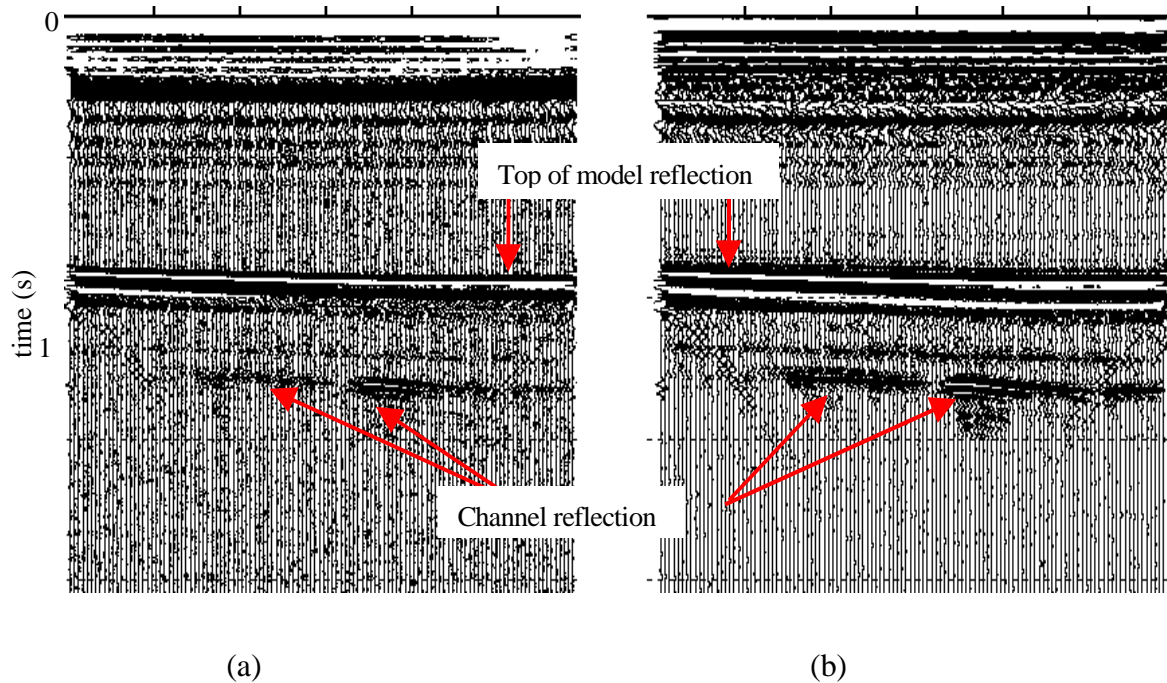


FIG. 4.8. Line 15 (a) before and (b) after bandpass filtering.

IV.2.4 Time-lapse association between datasets

Since I collected my time-lapse measurement in several stages, sometimes with weeks between experiments, I expect to find slight differences between the time-lapse datasets that are connected to acquisition rather than fluid flow. One major difference is a static shift of roughly 0.008 s between one dataset and another. The most probable reason is that of imprecise transducer origin at the beginning of each survey. From the first (water bottom) reflection event, the transducer positioning error is observed to be around 0.008 s delay (Figure 4.9), which corresponding to a 1.2 mm (model coordinate) spatial error. This 3-dimensional spatial error is because of the transducer origin misplacement, which is due to the limitation of student eyes. We will need to design our new Labview-based system to have a mechanical or electronic homing device.

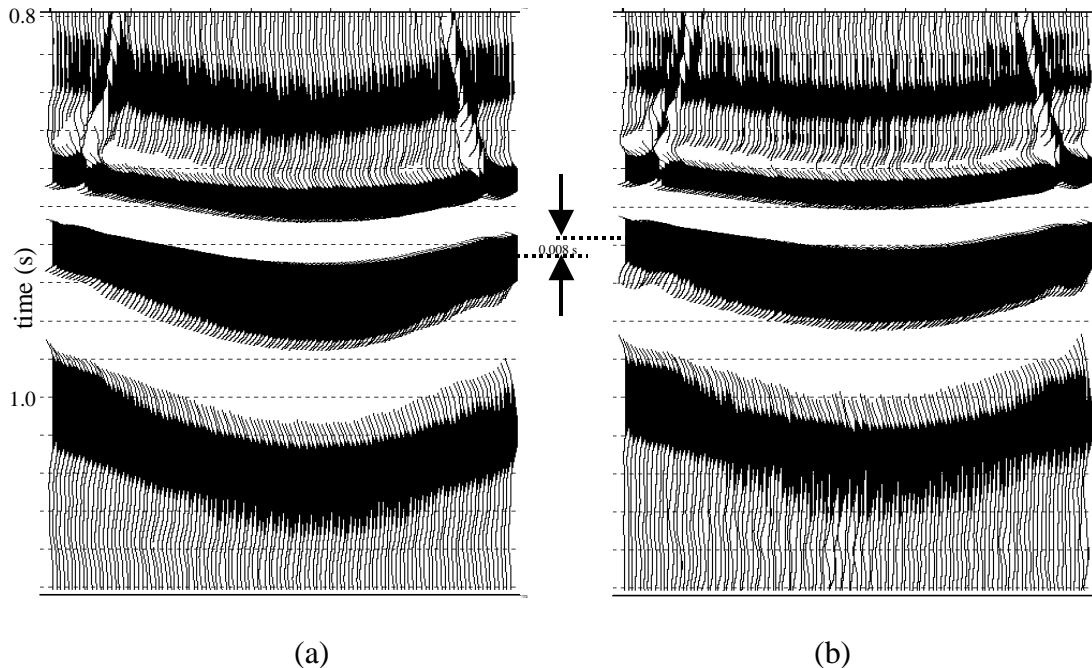


FIG. 4.9. Time lag of 0.008 s occurs between dataset (a) and dataset (b) collected in different surveys.

IV.2.5 Amplitude balancing

The stacked data of my different time-lapse datasets show considerable amplitude differences, not only where the channel is, but also at the water/clear-epoxy interface which should be invariable. The reason for this phenomenon is not obvious at this time, but irregularities in the electronic instrument power-supply and amplifier are good suspects. To resolve this discrepancy, amplitude balancing between datasets is necessary for time-lapse comparison. Examples of stack sections before and after amplitude balancing are shown in Figure 4.10. The scaling factor for each dataset will also be used to correct the prestack data in order to examine the AVO response.

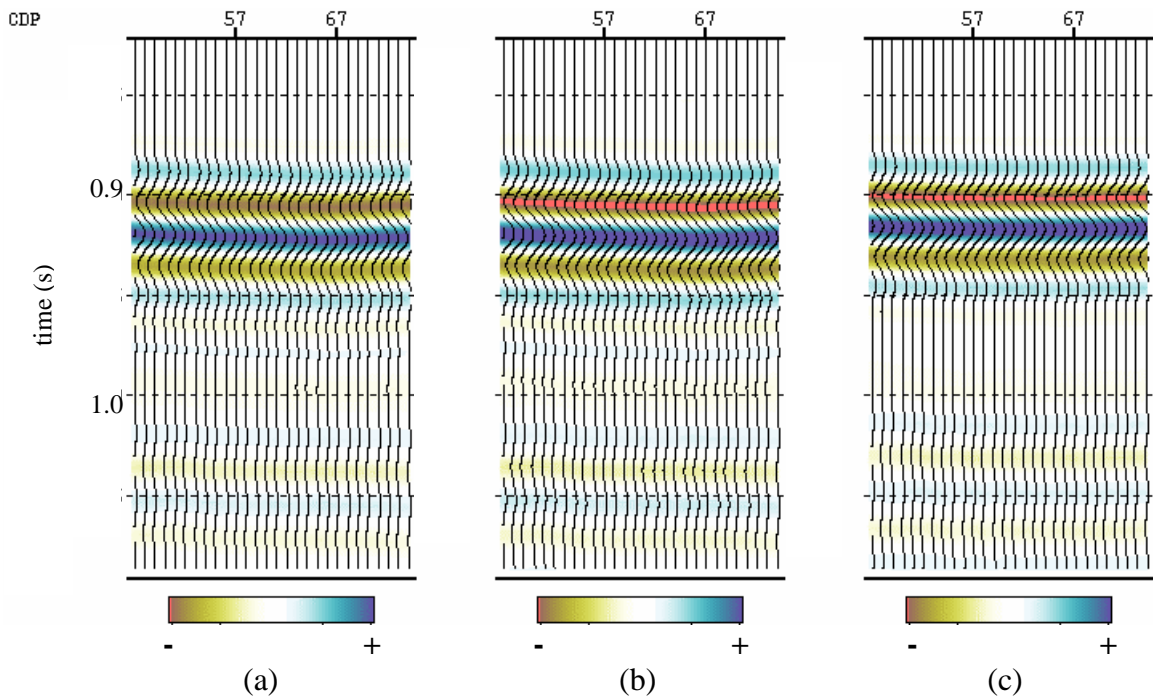


FIG. 4.10. Window about the water-epoxy interface for the (a) dry channel experiment, and (b) its scaled version (0.85) to match with the amplitude of the (c) wet channel experiment.

IV.2.6 Post-stack f-k time migration

Post-stack datasets now are ready for migration. A frequency-wavenumber domain 3-D time migration scheme (Stolt, 1978) is given by:

$$p(x,y,t) \rightarrow P(k_x, k_y, \omega) \rightarrow P'(k_x, k_y, k_z = [\omega^2/V^2 - k_x^2 - k_y^2]^{-1/2}) \rightarrow p'(x,y,z). \quad (4.2)$$

is implemented using Disco/Focus processing software (Paradigm Geophysical) to attain the channel image for each dataset (Figure 4.11).

IV.2.7 Pre-stack time migration

Besides implementing post-stack migration on the previous section, I also run a pre-stack Kirchhoff time migration on the time-lapse datasets (Figure 4.12) on AGL's Beowulf Cluster.

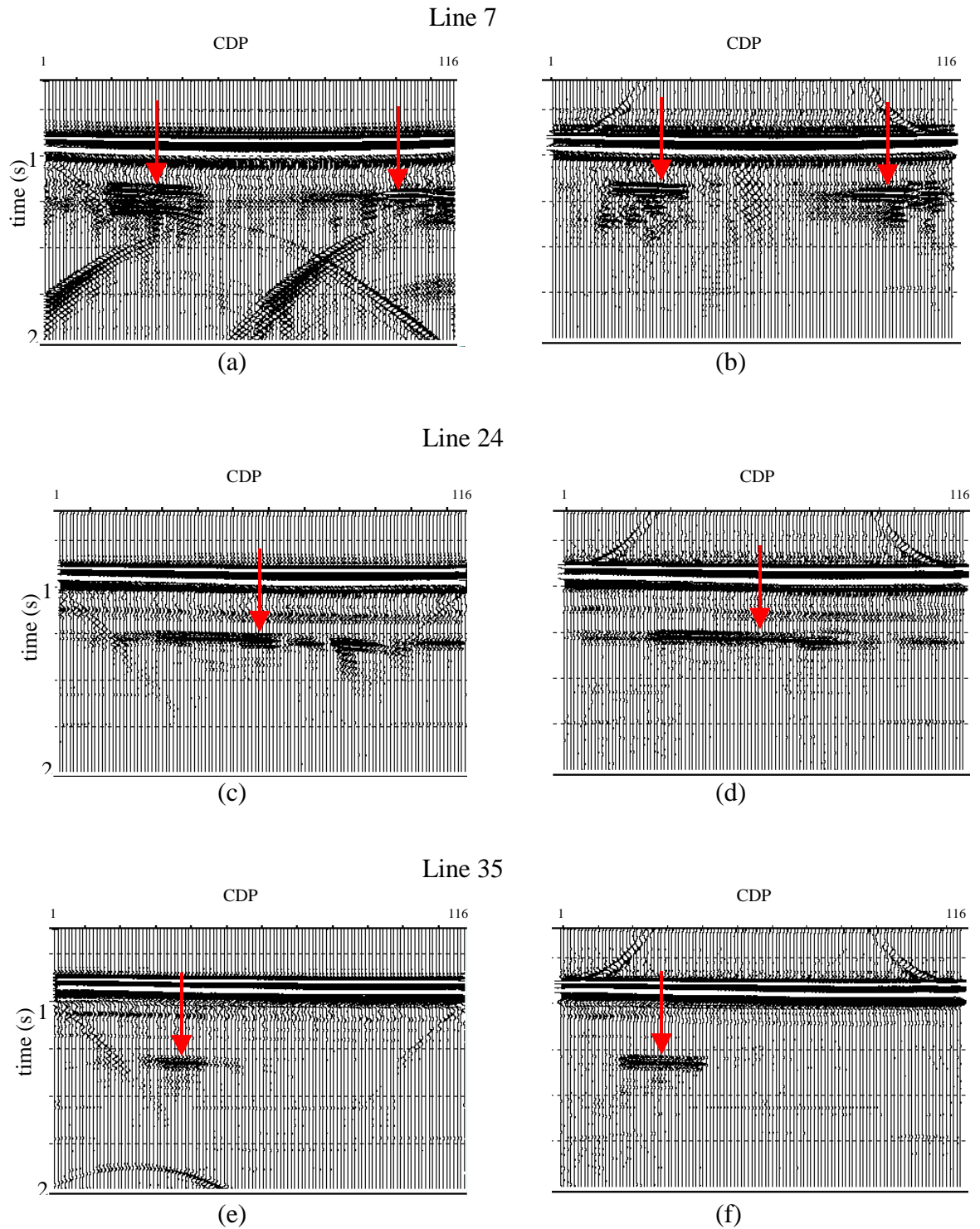


FIG. 4.11. Stacked line sections (a), (c), and (e), and their f-k migration results shown in section (b), (d), and (f), respectively. Reflection events from the channel (red arrow) are identified at around 1250 ms.

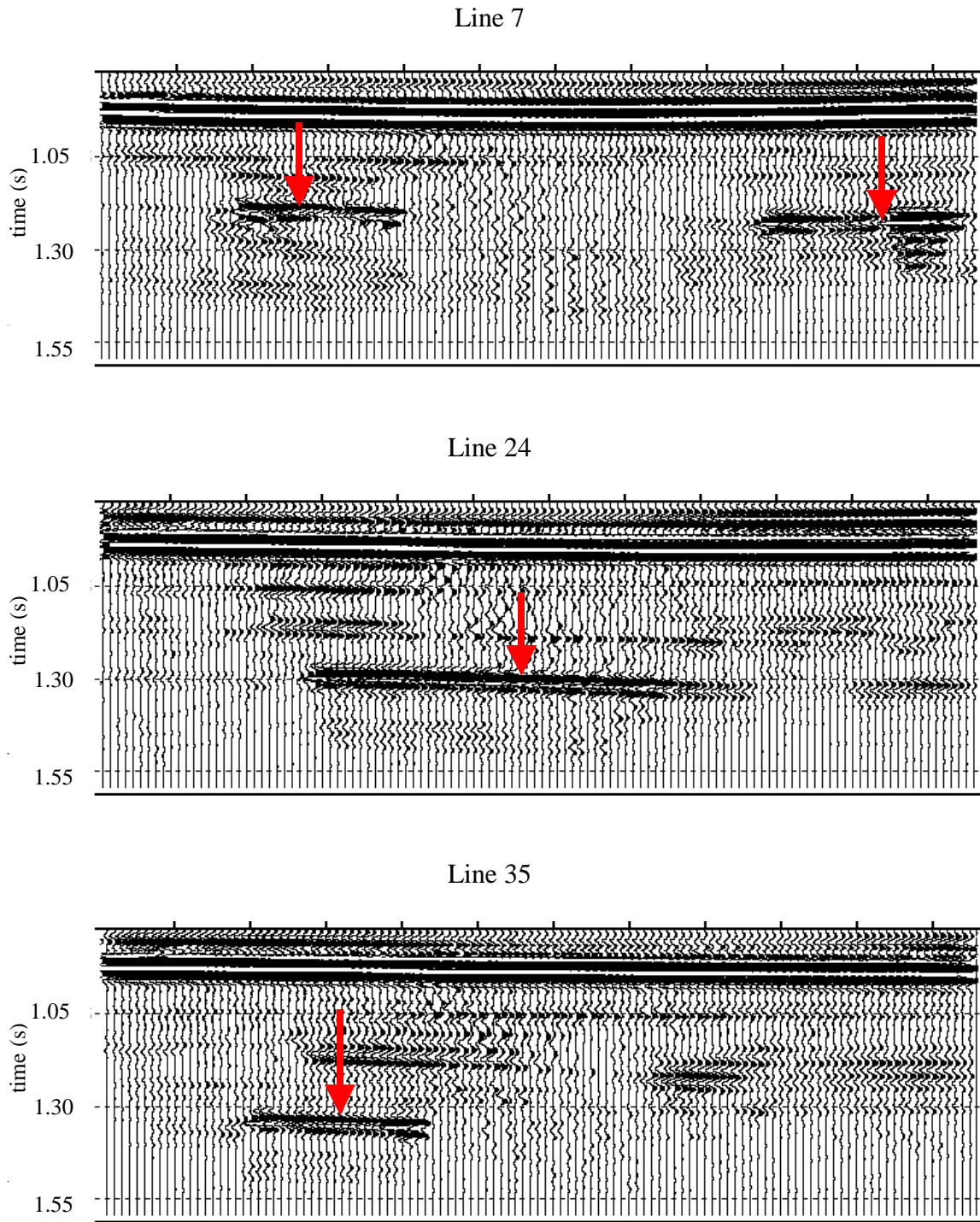


FIG. 4.12. Pre-stack Kirchhoff time migration result after mute and stacking. Channel reflection events are indicated by the arrows.

IV.2.8 2-D migration of vertically-stacked data

Other time-lapse datasets that I acquired using 2-D lines consist of 50 traces at each source and receiver pair location. After vertically stacking each CDP, which increases the signal-to-noise ratio, I apply the same data processing flow as before. The migration I use here is a wave equation finite difference technique in prestack time domain (Lowenthal et. al., 1976) provided by Focus/Disco processing package (Paradigm Geophysical). Migrated sections of both dry and wet channel sand are shown in Figure 4.13.

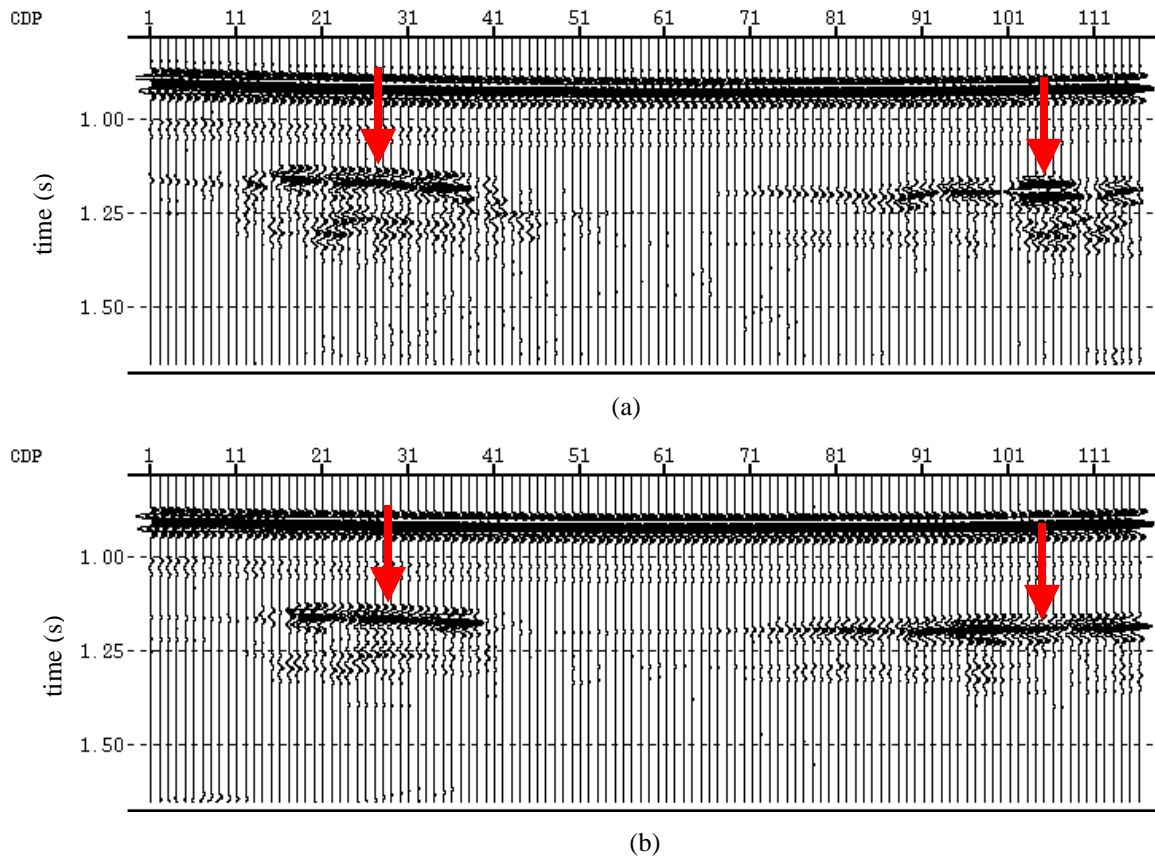


FIG. 4.13. Dry (a) and wet (b) channel sand images of line 5 using 2-D pre-stack time migration.

Chapter V

SEISMIC ATTRIBUTE ANALYSIS OF TIME-LAPSE DATASETS

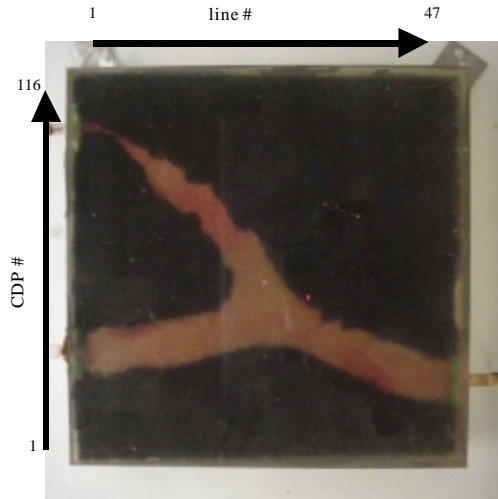
In this chapter, I will discuss the interpretation of time-lapse physical model data in order to determine pore fluid in the channel. First I will map the channel structure on time-slices through the migrated datasets. Second, I will upload these 3-D datasets into the Geoframe seismic interpretation package provided by Geoquest and do attribute analysis for pore-fluid identification. My simplest attribute analysis will be instantaneous frequency, cross-correlation, and Root Mean Square (RMS) amplitude on the stack of the pre-stack time-migrated data. The next will be simple AVO analysis on near, mid, and far angle stacks. Finally, I will generate coherence cubes of the datasets to study their feasibility as an alternative pore-fluid identification tool.

V.1 Time-slice evaluation

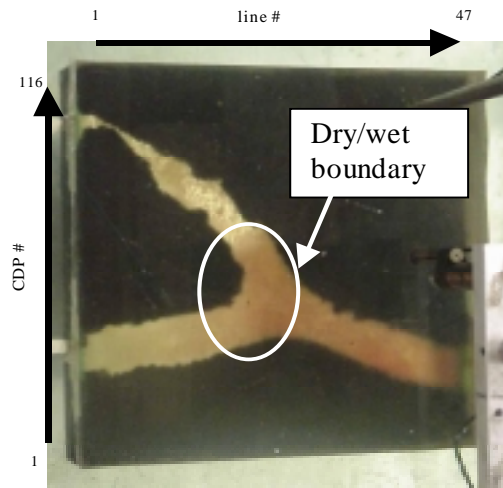
Three migrated time-lapse datasets of wet, half-wet, and dry channel-sand situations (Figure 5.1.a, b, and c), were collected, processed, and displayed in the time-slice domain using Focus 3D provided by Paradigm Geophysical (Figure 5.2). Viewing migrated time-slice sections in an animation loop greatly enhances the ability to identify the channel

structure. Figure 5.2 shows time slices at every 30 ms. The ringy signal of our transducer causes mixing of reflectors from the top and bottom of the dipping channel to continue for some time. Ideally, we should flatten the data on the horizon of interest before extracting the data for display.

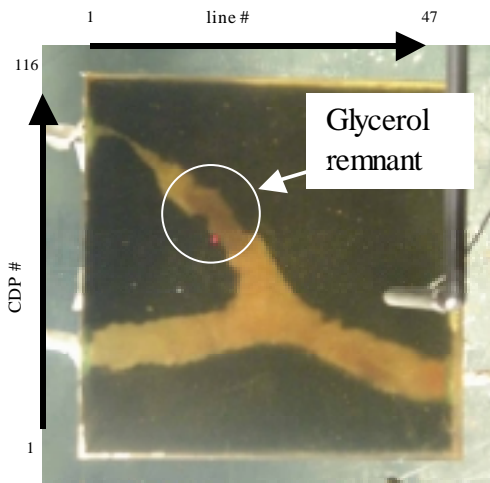
Seismic interpretation software, such as IESX (provided on Geoframe by Geoquest) is used to map reflection times of a picked horizon and clearly shows the east-west dipping structure where the channel is located (Figure 5.3). Note here that the time structure map in Figure 5.3 also gives some hints of the channel edges, but a better recognition of the channel is provided from the dip map (Figure 5.4).



(a)



(b)



(c)

FIG. 5.1. Digital photograph through the top clear resin layer of the (a) wet channel-sand, (b) half-wet channel-sand, and (c) dry channel-sand.

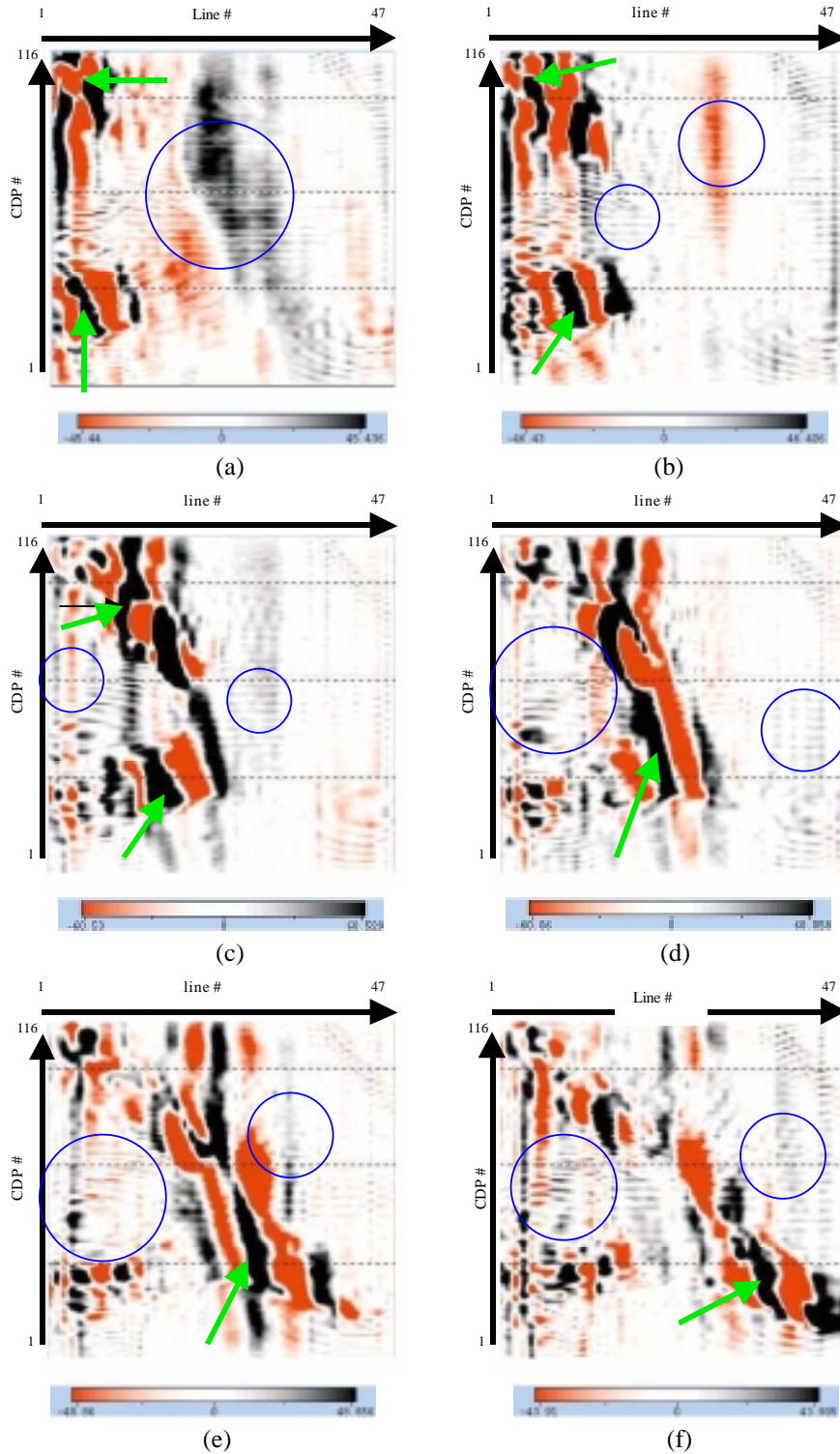


FIG. 5.2. Channel reflection events can be identified (green arrows) in time slices at (a) 1180 ms, (b) 1210 ms, (c) 1240 ms, (d) 1270 ms, (e) 1300 ms, and (f) 1330 ms. Some examples of acquisition footprint are indicated by blue circles.

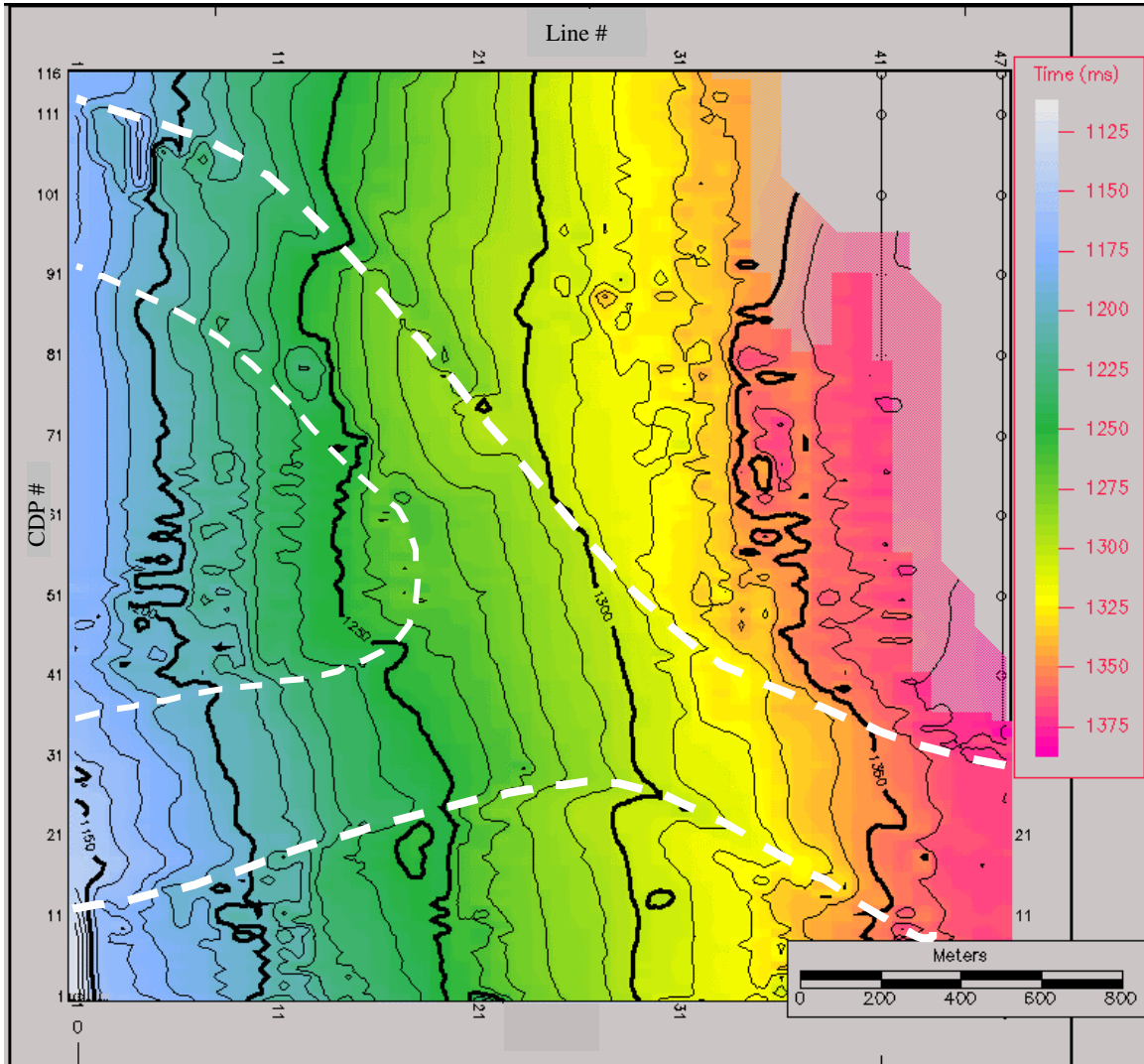
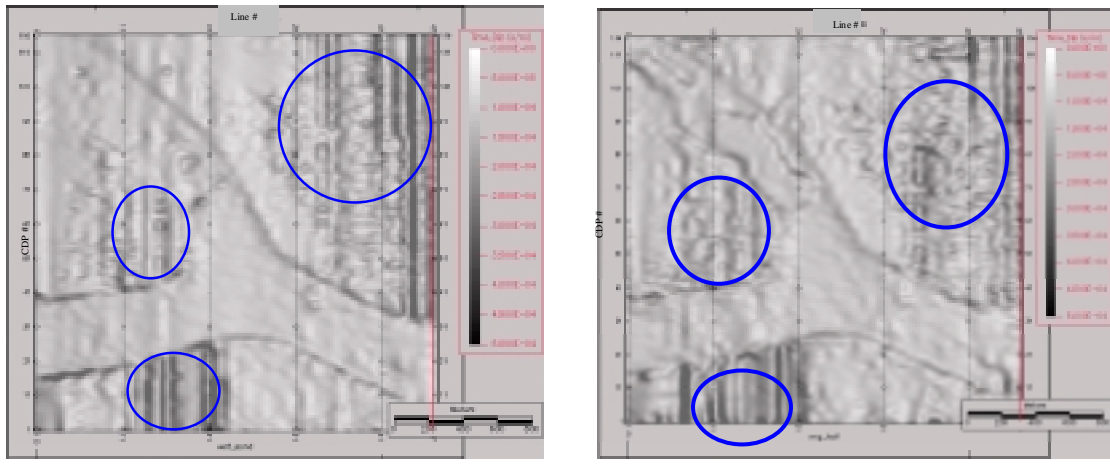
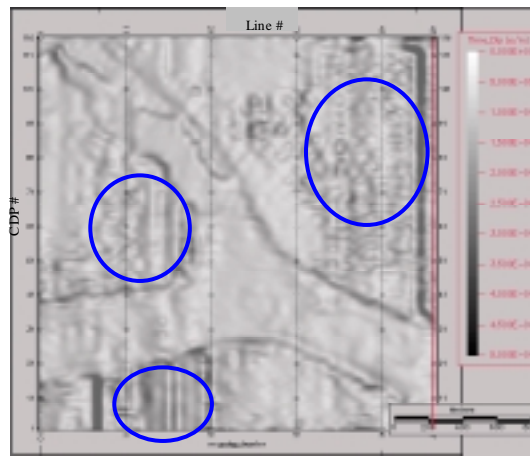


FIG. 5.3. Time structure map of the channel horizon shows the east-west dipping (7°) structure and the channel edges along dotted white curves.



(a)

(b)



(c)

FIG. 5.4. Dip maps of the (a) wet, (b) half-wet, and (c) dry channel horizon can enhance the illumination of channel structure since the channel top is slightly higher than the surrounding interface. Acquisition footprints are found in some areas (in circles).

V.2 Seismic attribute analysis

After the channel structure identification, the next task is to attempt to delineate the channel and internal gas/glycerol fronts. In this section, I will analyze the characteristics of some commonly used seismic attributes available within Geoframe IESX, with the aim of detecting the presence of gas and glycerol in the channel. By comparing these seismic attributes to the known actual (optically photographed) model, I can study the effectiveness of different seismic attributes as a pore-fluid indicator.

In order to generate seismic attributes along the dipping horizon shown in Figures 5.3, and 5.5, I set a time window from 20 ms above to 20 ms below the horizon shown in Figure 5.5.

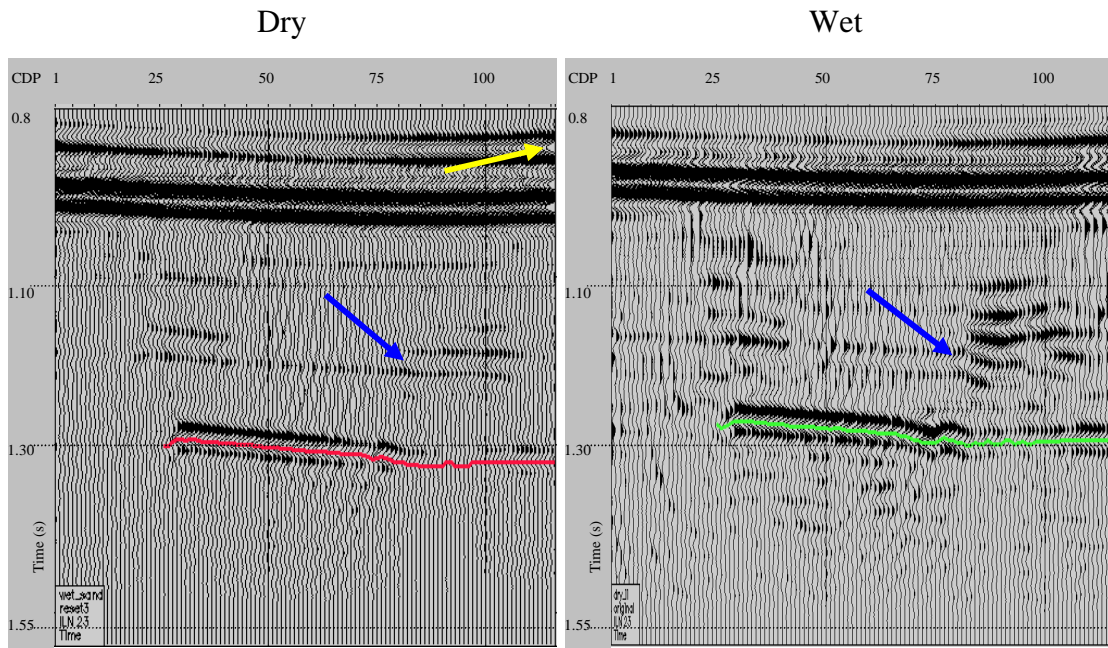
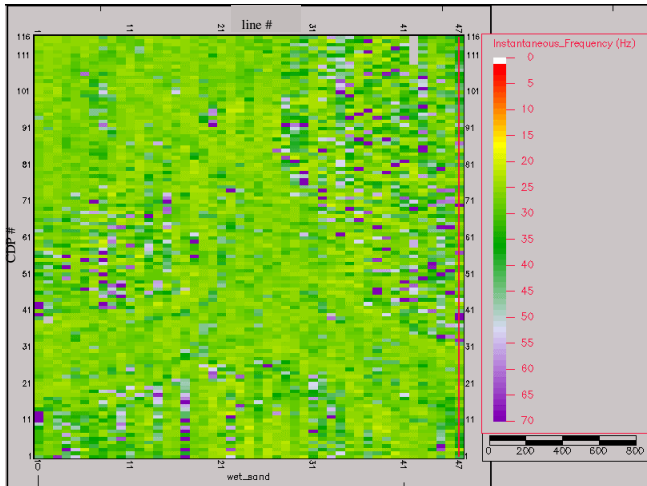


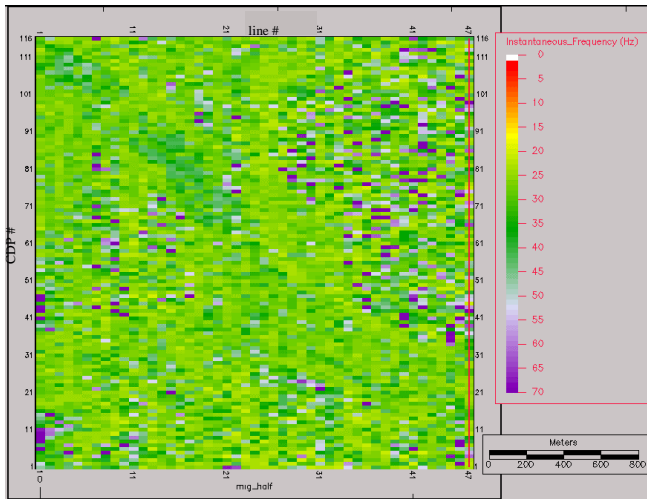
FIG. 5.5. Horizon pick (in green and red) along the trough of the channel reflection event on line 24. The event indicated by the blue arrow is an interface formed by pouring the epoxy in 1 cm increments to minimize heat generation. The large trough indicated by the yellow arrow is due to the collapsed diffraction energy from the model edge.

V.2.1 Instantaneous frequency

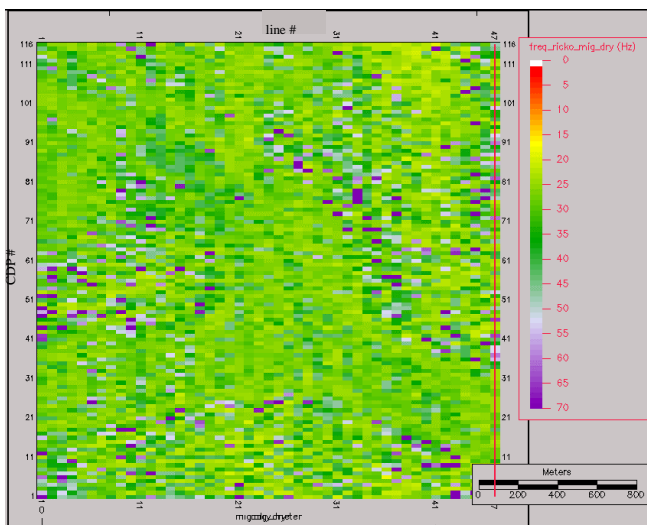
The instantaneous frequency is a measure of the frequency of the waveform at every sample. I produced instantaneous frequency maps for all three channel conditions (Figure 5.6). As expected from its formulation, the instantaneous frequency, whose values fall at around 30 Hz, does not seem to depend on fluid type and is not a good prediction of pore-fluid content for my channel model.



(a)



(b)



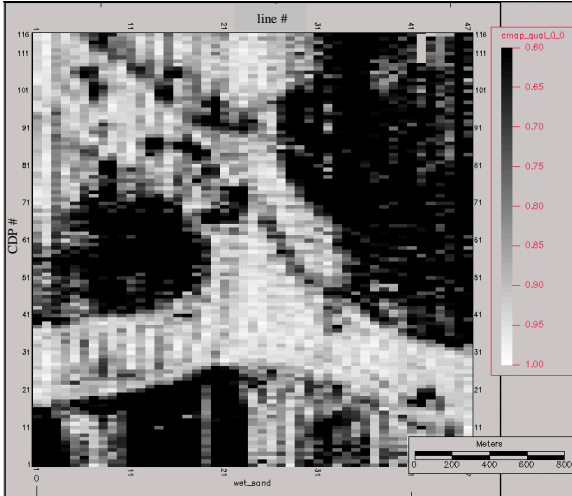
(c)

FIG. 5.6. Instantaneous frequency maps of (a) wet channel, (b) half-wet channel, (c) dry channel. The dominant instantaneous frequency is at 30 Hz.

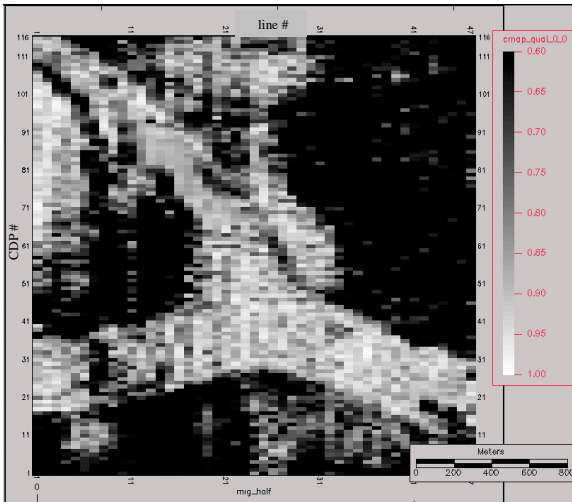
V.2.2 Cross-correlation

Cross-correlation mapping generates an attribute whose values are derived from the cross-correlation of each trace against a number of adjacent traces. The computed attribute provides a measure of similarity between the traces being compared. A high correlation indicates the traces match well, while low correlation indicates that they are dissimilar.

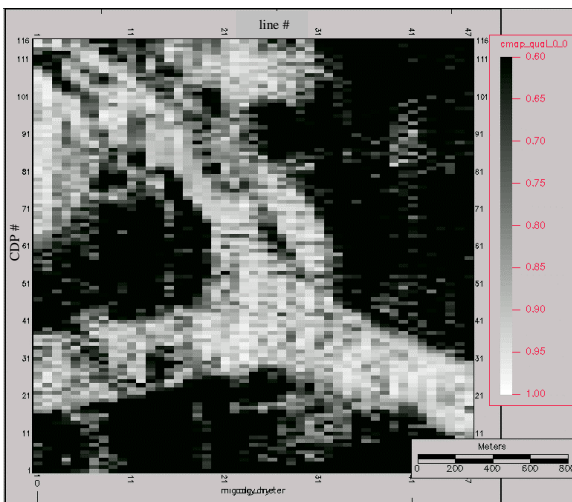
The operation is performed along the same channel horizon as the other attributes. The computation begins with cross-correlating a trace with eight adjacent traces and then averaging the output. Note here that I input a constant 70 ms correlation window and 15 ms search window, while assigning the zero reference along the horizon. Hence, the center of cross-correlation process is always maintained along the horizon, providing a more useful output display. The cross-correlation maps across the horizon (Figure 5.7) allow us to identify the channel structure, where the trace discontinuity occurs, but unfortunately not the dry and wet channel boundary.



(a)



(b)



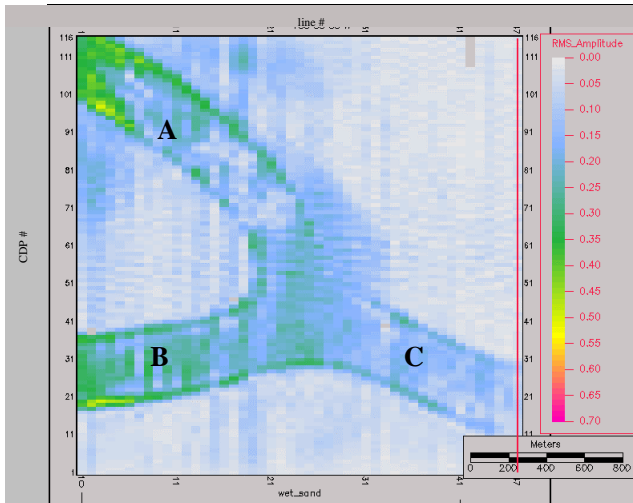
(c)

FIG. 5.7. Cross-correlation maps of (a) wet channel, (b) half-wet channel, (c) dry channel.

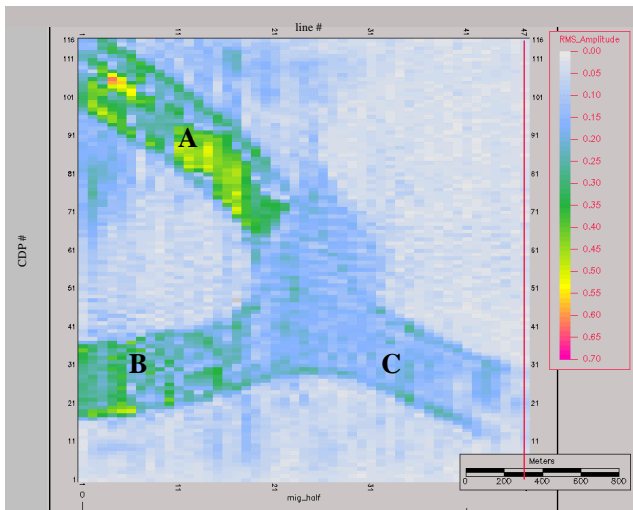
V.2.3 Root-Mean-Square (RMS) amplitude

The RMS amplitude is calculated by taking the square-root of the sum of the amplitude squared divided by the number of live samples. I used the same 40 ms time window along the horizon to calculate the RMS amplitude. Each dataset was normalized to the top water-epoxy reflection at around 910 ms.

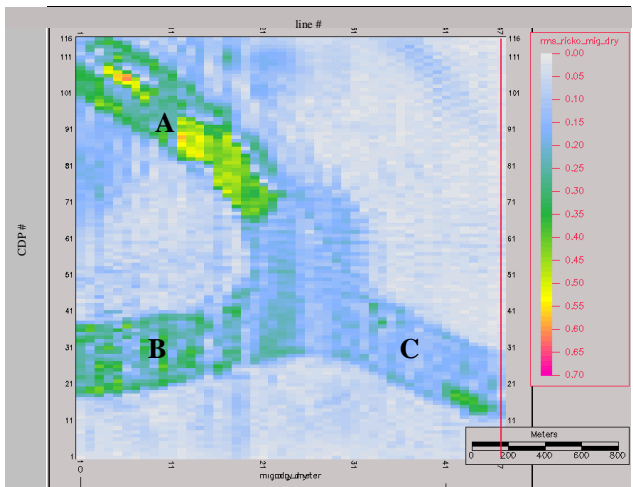
Examining the RMS amplitude maps on Figure 5.8, we note that the wet and half-wet channel situation correlates closely to the optically photographed control model (compare Figures 5.8.a and 5.8.b with Figures 5.1.a and 5.1.b). Lower RMS amplitude values occur at area label 'C' of half-wet channel and at area label 'A', 'B', and 'C' of the wet channel. Since these areas are all in a wet state, then the similarity of wet area RMS amplitude responses and the difference of wet and dry RMS amplitude responses between datasets may be considered to be a good candidate as a pore-fluid indicator. However, this hypothesis needs to be verified, especially since the third RMS amplitude map, extracted from the dry channel situation, shows more ambiguous responses. The dry channel RMS amplitude map in Figure 5.8.c does not show the expected high amplitude along the entire channel, but only at the same dry area (areas labeled 'A' and 'B') that the half-wet channel has. In other words, the area label 'C' appears to remain 'wet'.



(a)



(b)



(c)

FIG. 5.8. RMS amplitude maps of (a) wet channel, (b) half-wet channel, (c) dry channel.

Carefully comparing all three maps in Figure 5.8, I note that:

- (a) On the dry channel map, the RMS amplitude at 'B' is considerably lower than that at area 'A' even though both areas are dry. This irregularity also appears on the half-wet channel.
- (b) At 'C' on all datasets, although all three maps show low RMS amplitude values, the dry channel has a little higher RMS amplitude (indicated with more blue and a few green colors) compared to the half-wet and wet channels. This wet area on the half-wet and wet channels has equivalent RMS amplitude values.

Closer examination of the optical control image (Figure 5.9) shows a patchy area at 'A' that does not look like other areas of the channel. This area seems to be shinier or more optically reflective in Figure 5.9. I have two hypotheses as to the cause of this anomaly:

- (1) there was a loose contact between the epoxy and sintered glass beads due to model warping as it cooled, or
- (2) there was an incomplete flushing of the fluid with air between experiments. It becomes very difficult to incorporate this particular anomaly area (labeled as 'A') for further comparison or evaluation.

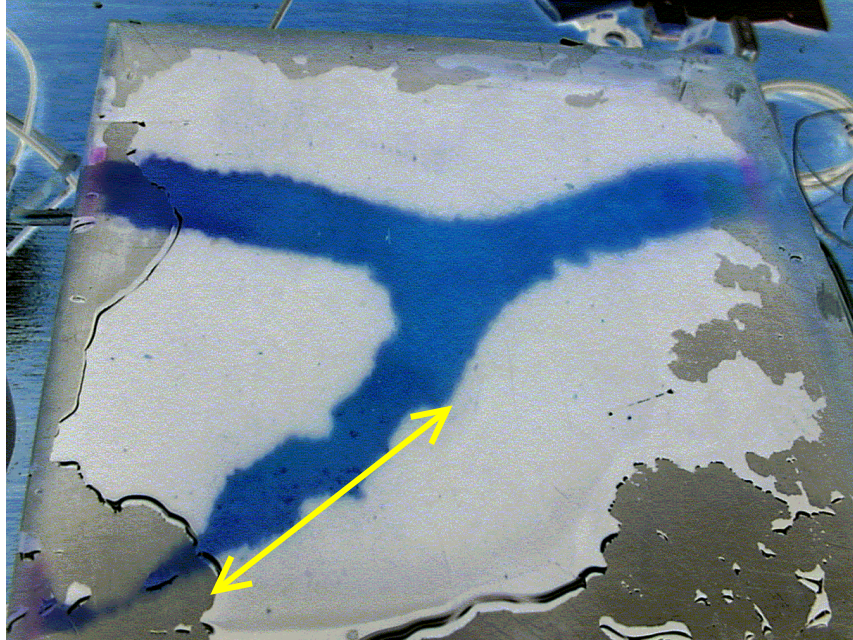


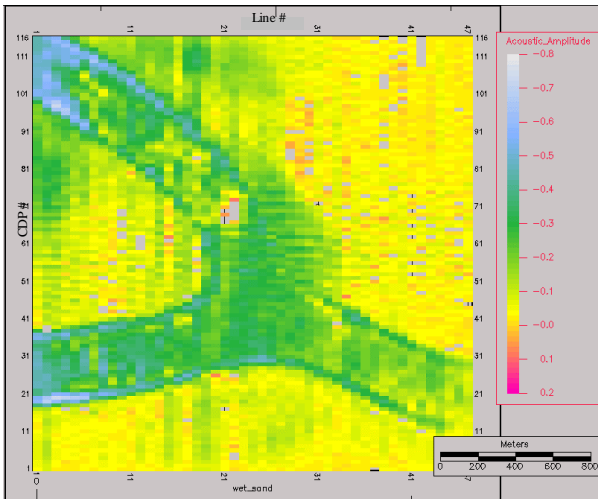
FIG. 5.9. The channel model anomaly area that gives misleading high RMS amplitude is shown along the arrow on this digital photograph. A film of water lies on top to render the clear epoxy more transparent.

Putting area ‘A’ aside for further evaluation, I still have the other dry area (labeled as ‘B’) which shows a higher RMS amplitude than the wet area. Additionally, the slight RMS amplitude difference observed at area ‘C’, as mentioned in point (b) previously, also shows an RMS amplitude increase in the dry channel dataset. Thus, except for anomaly area ‘A’, other areas are acting according to prediction.

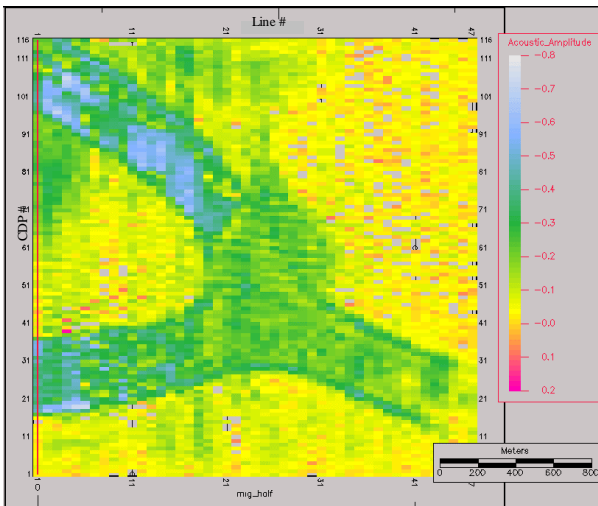
In order to understand why the RMS amplitude changes only slightly with fluid changes, I went back to look at the channel physical model. At this point, the channel is in dry condition, since I swept the glycerol with air during my last run of time-lapse acquisition. Although I had intended my first model to be the dry channel (as constructed) followed

by half-wet and wet channels, I could not use these first three datasets due to a very poor signal-to-noise ratio (see Chapter 4). Consequently, when I attempted to recollect the data, the entire channel had been first filled with the glycerol. During my second attempt of data acquisition, we first collected the wet channel data, and then drained the channel with a vacuum machine to collect partial dry and dry channel data. Not surprisingly, some glycerol is trapped inside the 'dry' channel, indicated by some light red color in the model (seen in Figure 5.1.c). This 'unfortunate' circumstance turns out to better simulate most real reservoir exploitations. This remaining glycerol or bypassed pay inside the channel causes the small RMS amplitude contrast between dry and wet channels at area 'B' and 'C' and is not very significant. Figure 5.10 shows the amplitude extraction maps along the dipping horizon for wet, half-wet, and dry channels, which correspond similarly to the RMS amplitude analysis.

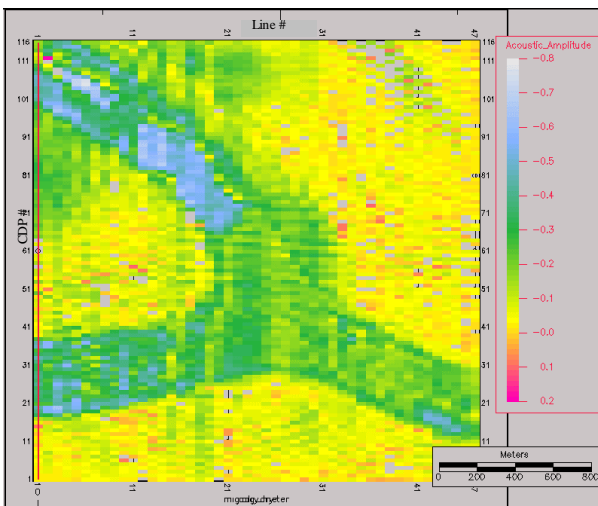
So far, we can only say that RMS amplitude changes perhaps indicate different channel environments. In the following section, I will discuss the prestack data evaluation and the comparison to the theoretical estimate, which focuses on fluid type discrimination.



(a)



(b)



(c)

FIG. 5.10. Amplitude extraction maps along the dipping horizon for (a) wet, (b) half-wet, and (c) dry channels.

V.3 Comparison to the model estimate

In order to compare the amplitude of physical model migrated data and its theoretical prediction, an amplitude response estimate based on the model rock-properties must be first established. In order to understand the migrated amplitude response, I need to build the AVO response prediction of the model beforehand. Using the material properties described in Chapter 3, I run the same modeling software I used in Appendix B (Cerveny and Ravindra, 1971), for both dry and wet channel-sand models (Figure 5.11).

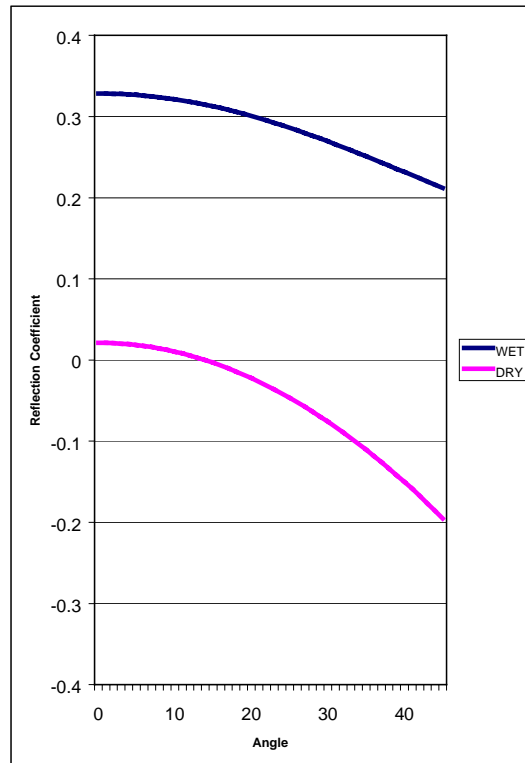


FIG. 5.11. Theoretical Reflection Coefficient versus angle from dry and wet channel sand reflections. Angles corresponding with the data acquisition geometry are in the range between 10° to 30°.

As shown in Figure 5.11, the absolute reflection coefficient values shows that the wet sand 'trough' will decrease and the dry sand 'peak' will increase as the angle of incidence increases. Note here that the negative sign of dry sand will rotate the signal phase by 180 degrees). The dry and wet sand responses do not fall into the same class (Rutherford and Williams, 1989). The dry channel model AVO response is associated with class 3 or bright-spot AVO, while the wet channel model AVO response is associated with class 1 or dim-spot AVO.

Certainly, the comparison with the time-lapse datasets must be done in the pre-stack domain, whereby I then choose to use the pre-stack migrated data. Since the pre-stack migration algorithm assigns a larger value for its output offset interval (100 m) than the acquisition geometry (40 m), the number of traces in a CDP gather after migration is fewer. Therefore, for AVO comparison I only selected the first seven traces in a CDP gather, which sufficiently represent all wave propagation within about 30° incidence angle- the maximum angle in which my AVO anomaly prediction is still reliable. Note here also that the pre-stack migrated first trace always has zero amplitude because it is located at zero offset, and my time-lapse data does not have any offsets between 0 and 50 m. Conveniently, the availability of only six traces will roughly resemble an angle stack. Some CDP gathers of dry, half-wet, and wet channel located at area label 'C' are shown in Figure 5.12. Note here that the channel in the half-wet dataset over this region is wet. Figure 5.13 displays these three time-lapse datasets at the location labeled 'B'. Contrarily, the channel in the half-wet dataset over this region is dry.

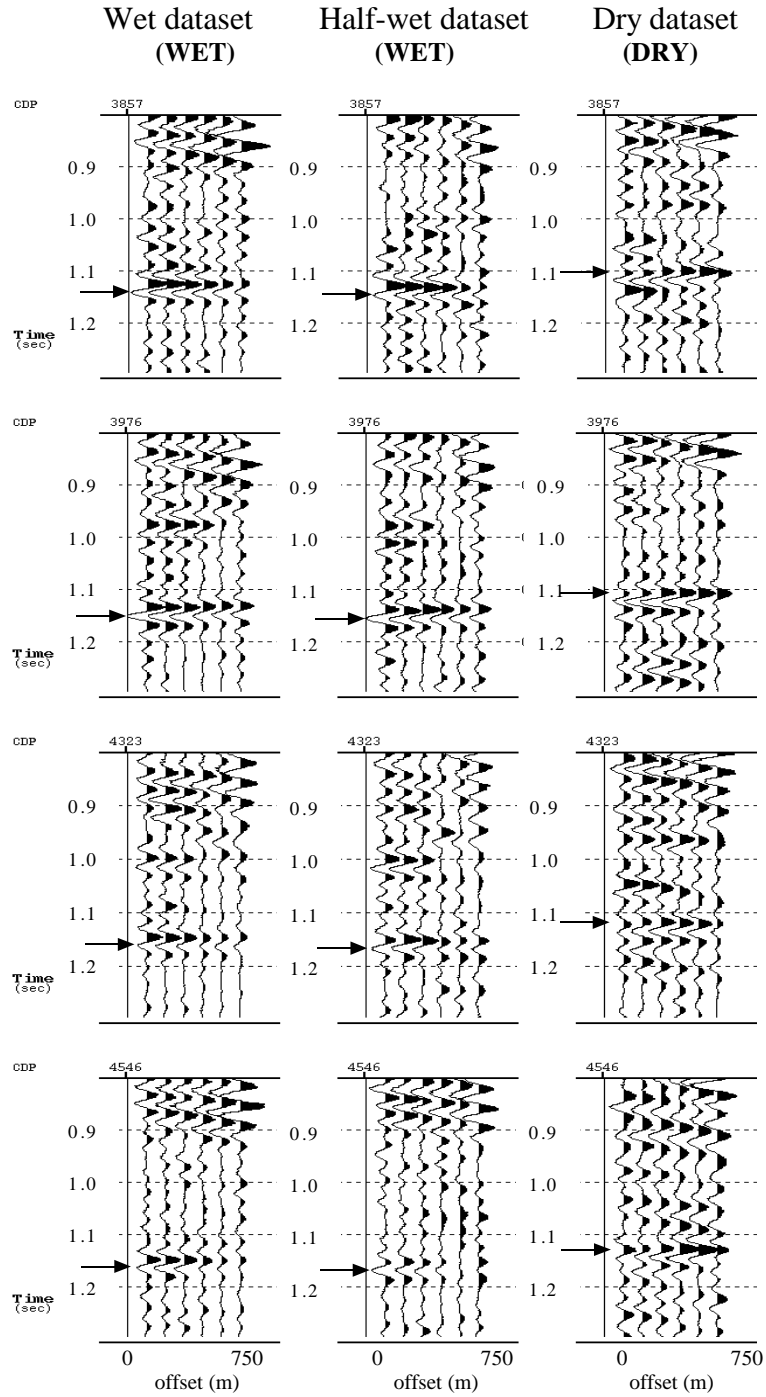


FIG. 5.12. CDP gather comparison at 4 locations of dry, wet, and wet channels corresponding to area C on Figure 5.8. Target events, indicated with arrows, show amplitude increase with angle for the dry channel and amplitude decrease with angle for the wet channel.

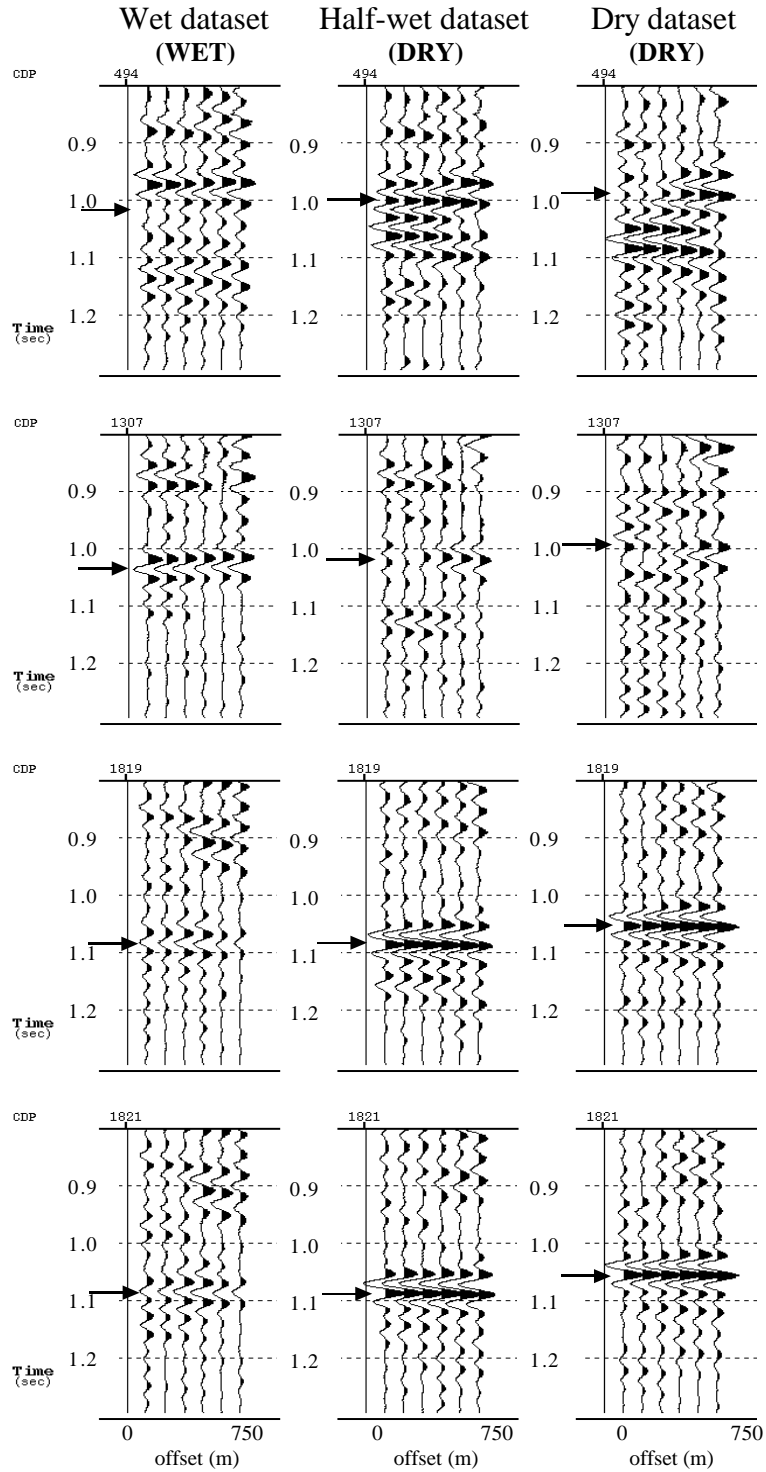


FIG. 5.13. CDP gather comparison at 4 locations of wet, dry, and dry channels corresponding to area B on Figure 5.8. Target events, indicated with arrows, show amplitude increase with angle for the dry channel and amplitude decrease with angle for the wet channel.

Three important facts I observed from Figures 5.12 and 5.13 are:

- (a) The reflection events in the dry channel dataset arrive 20 ms earlier than the same events in half-wet and wet datasets. Inaccurate transducer positioning causes time differences between these datasets (see Chapter 3).
- (b) The reflection events on wet and half-wet datasets arrive at the same time approximately (by matching the earlier waveforms at around 0.85 ms on Figure 5.12).
- (c) The channel reflection undergoes a phase reversal between the dry and wet pore fluid cases.
- (d) Amplitude decreases with offset for the wet channel situation, and increases with offset for the dry channel situation.

Notice that some deviations from observation (d) are found in these two figures. For example, in Figure 5.12, the amplitude in the dry area decreases at far traces after it increases first. Also in Figure 5.13, amplitude does not change much in the wet area. However, considering that the phases are reversed and the amplitudes are changed as described in (d), I will argue that these deviations are tolerable, because of the fact that phase reversal does strongly correlate with the RC plot from the model (Figure 5.11) as the wet channel has a positive RC and the dry channel has a negative RC. Secondly, the predicted amplitude increase with offset in the dry channel and amplitude decrease with offset in the wet channel (Figure 5.11) are also associated with the time-lapse data. Note too that the gradient amplitude changes of the dry channel are greater than those of the wet channel, implying that the amplitude increase in the dry channel should be easier to

recognize. These gradient changes correspond with the RC estimate on Figure 5.11 as well.

Having examined and compared the time-lapse datasets with the AVO prediction, we now have more confidence to better discriminate pore-fluid contents. Hence, incorporating this AVO analysis on pre-stack data with the previous attribute analysis will enable us to estimate the fluid movement. The near, mid, and far angles are also mapped along the dipping horizon. Figure 5.14 shows these amplitude extraction maps for wet, half-wet, and dry channels.

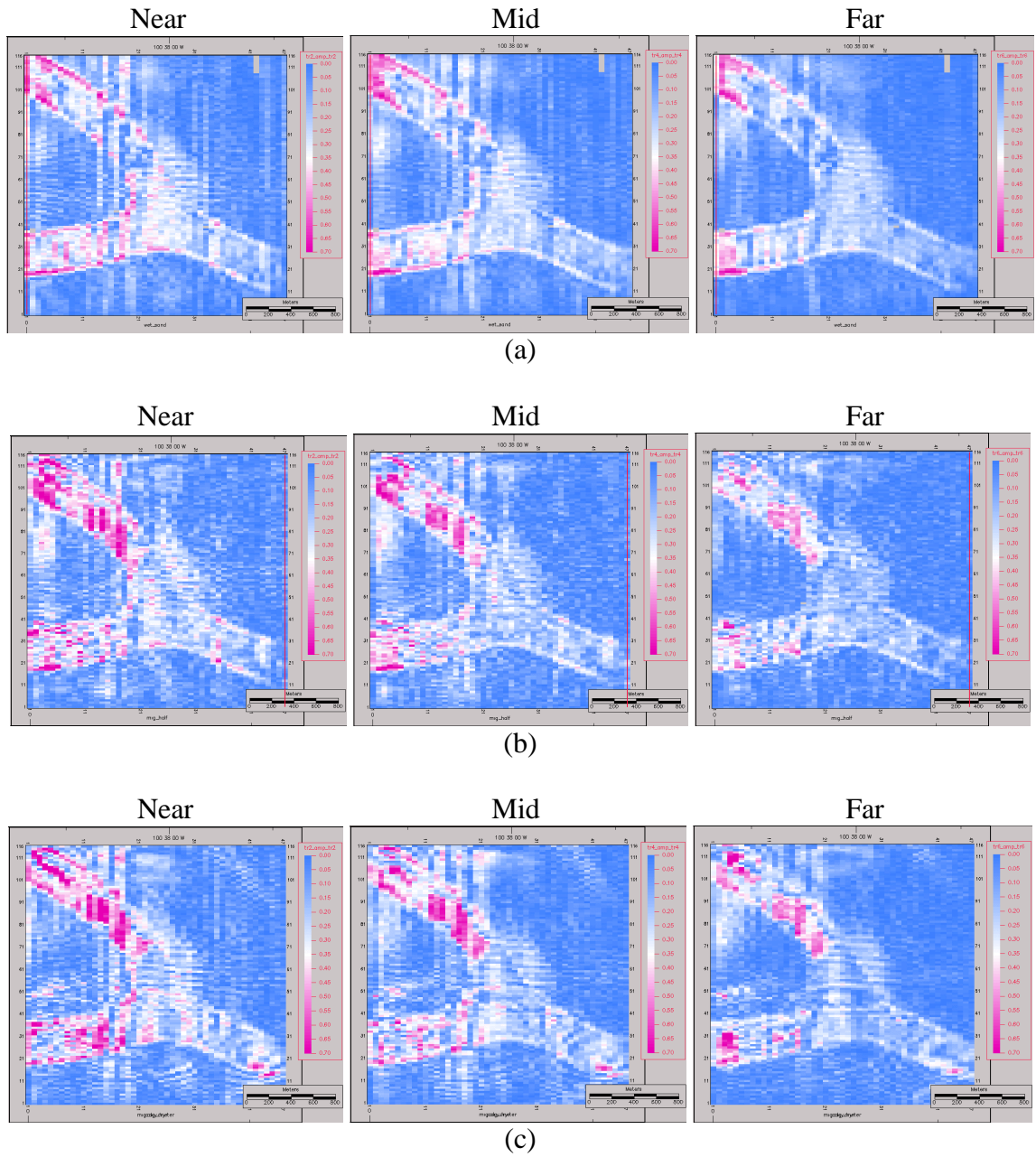
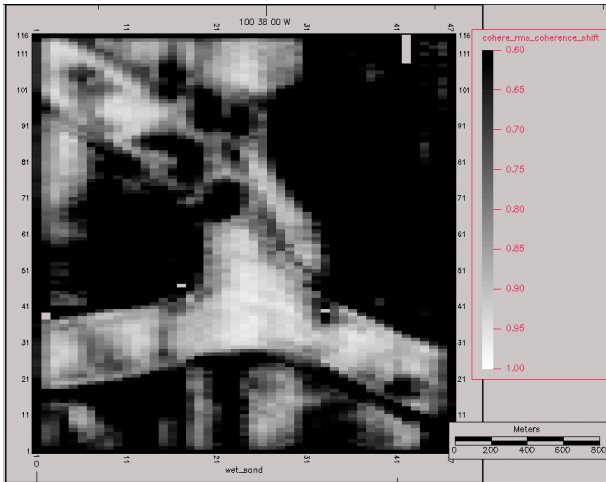


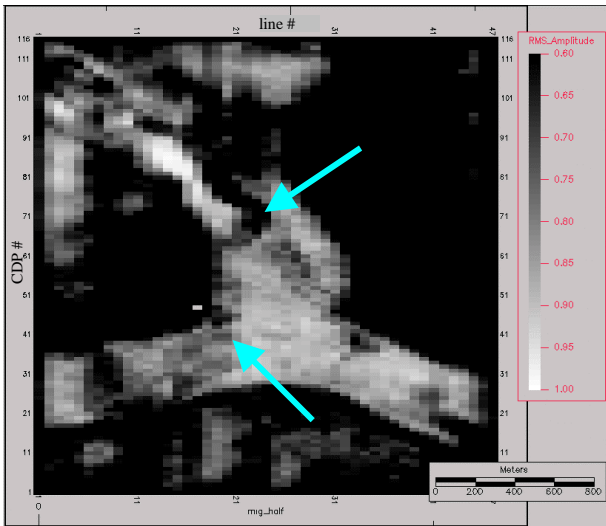
FIG. 5.14. Amplitude maps of the near, mid, and far angles of the (a) wet, (b) half-wet, and (c) dry channels.

V.4 Coherence analysis

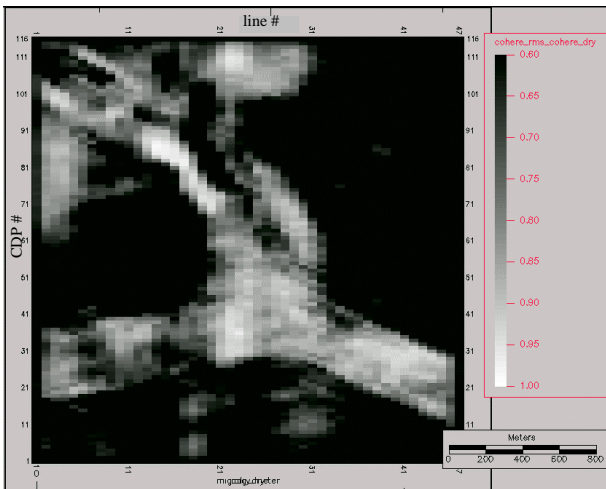
In this section I will discuss a coherence analysis on three seismic volumes of different channel situations from the stack of pre-stack time-migration data. The seismic coherence method I used is the semblance-based C_2 algorithm (Marfurt et.al., 1998). As with other coherence algorithms, the semblance-based algorithm collects traces in a running window; for example with dimensions of 3 traces inline, 3 traces crossline, and 40 ms. The data in each window are used to estimate the lateral continuity of the seismic events that fall in this window. Intuitively, the coherence attribute will be brighter (closer to white) in areas where the seismic events are laterally highly continuous. On the other hand, in the presence of a discontinuity, for example at the channel edges, the coherence attribute will be darker. Areas dominated by incoherent noise will also be dark. The seismic coherence maps of three channel cases shown in Figure 5.14 can illuminate the channel structure and the dry/wet boundary on half-wet channel case. Provided the amplitude of near, mid, and far angles (Figure 5.13), I then created the coherence maps for each channel situation (Figure 5.15).



(a)

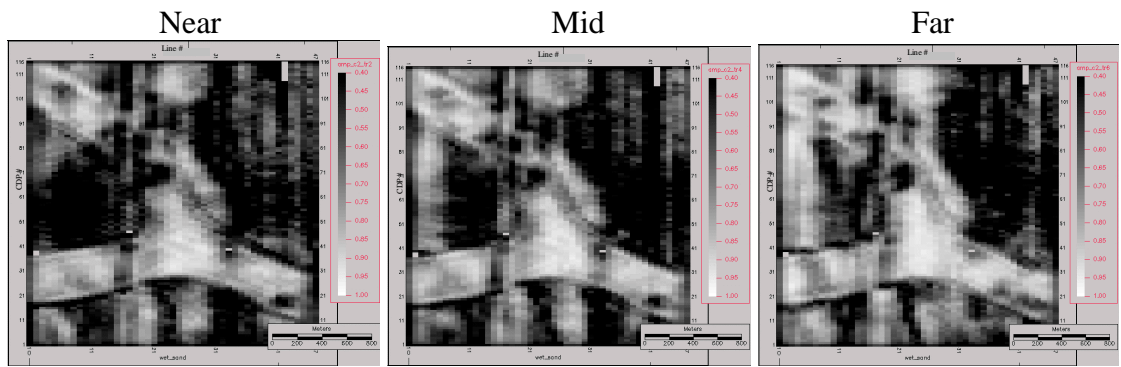


(b)

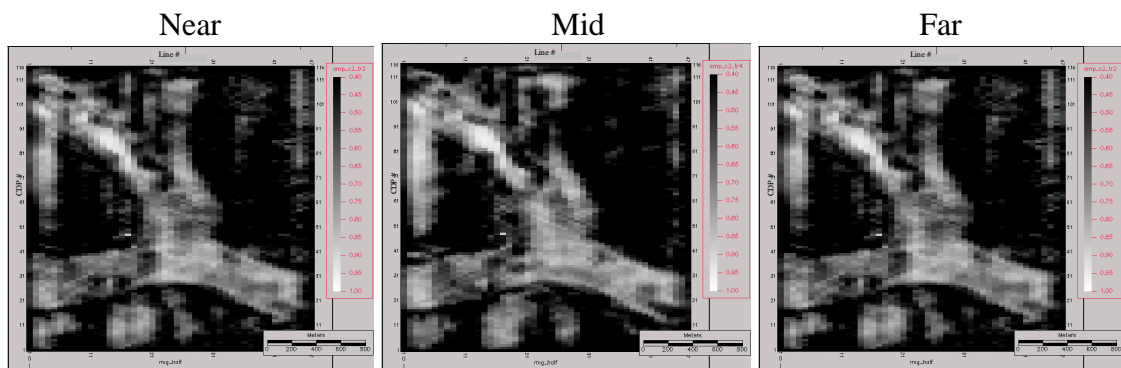


(c)

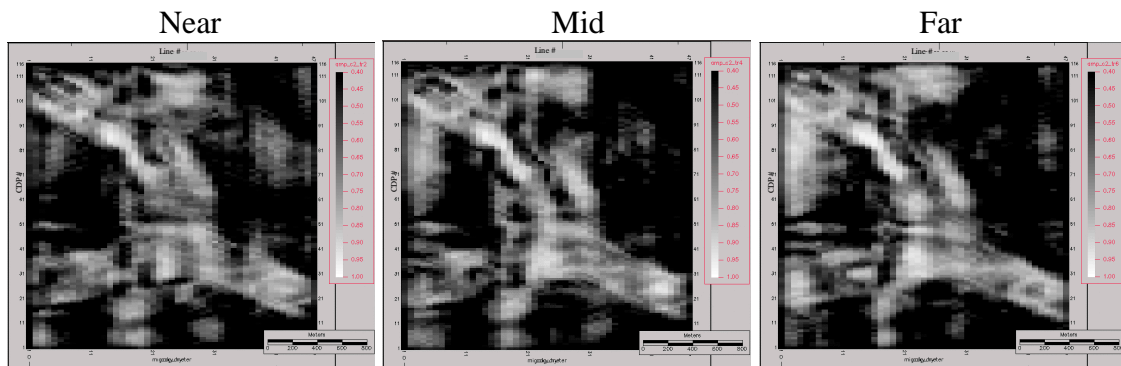
FIG. 5.14. Coherence maps of (a) wet channel, (b) half-wet channel, (c) dry channel.



(a)



(b)



(c)

FIG. 5.15. Coherence maps of near, mid, and far angles extracted from the pre-stack migrated data for (a) wet, (b) half-wet, and (c) dry channels.

Chapter VI

CONCLUSION

I expected to encounter three challenges in using physical models to simulate porous channel sands for time-lapse interpretation. The first challenge was related to the porous medium model construction, with the goal of approximating the geophysical properties associated with porous gas sands. The second challenge was the ability of our physical modeling system to do repeated time-lapse acquisition. The third challenge was calibrating our transducers to preserve relative amplitude measurements due to distance and angular directivity. I did not expect to encounter a fourth challenge- that of the fluid registration.

In spite of these formidable challenges, I am able to conclude that:

- (a) Sintered glass beads are a very good candidate for modeling porous rocks, having permeability, porosity, and Poisson's ratio that fall within the range of productive gas sands.
- (b) Calibration of transducer radiation patterns is essential to the preservation of relative amplitudes.

- (c) On time-lapse 3-D datasets comparison, the RMS amplitude attribute shows differences between dry and wet channel, which eventually signify the channel fluid-front. Other attributes including instantaneous phase, instantaneous frequency, and cross-correlation, are relatively insensitive to fluid change.
- (d) Comparison of pre-stack 3-D datasets with the estimated AVO response allows the discrimination of channel pore-fluid content.
- (e) Semblance-based coherence analysis is an excellent tool to illuminate the channel edge and the dry/wet boundary in the channel.
- (f) AVO analysis on 2-D lines inadequately satisfies the phase reversal prediction, but the changes in amplitude response between dry and wet channel still exhibit some differences. This 2-D dataset suffers from 3-D dip and sideswipe problems.
- (g) 3-D physical models suffer from many of the same acquisition problems of real time-lapse seismic experiments- positioning errors, residual patchy gas, and 'geologic' noise due to extra interfaces being introduced during model construction.

VI.1 Suggestions for future work

Along with the current experimental establishment of physical model of porous media incorporating AVO analysis for pore-fluid discrimination, I list some suggestions based on the problems I experienced during the experiment and the hope for continuing research:

- (a) An integrated upgrade on AGL's physical modeling acquisition system, especially to avoid indexer failure and energy irregularity during long duration data acquisition. An effective way to QC the data would be to embed a signal analysis tool in the data acquisition system, by simply triggering the recording with and without the source being fired. We can then calculate spectral ratios and detect noise burst due to faulty electronics and building noise.
- (b) To achieve accurate geometry, particularly if repeated datasets are to be acquired, a better transducer positioning technique is necessary. Optical or pressure switches might be used to reposition transducers at the corner of the model at permanent reference points.
- (c) Ringy signals by pulsing of transducers at resonance can be ameliorated by using a chirp signal.
- (d) Larger models are important in order to avoid some unwanted signals, such as diffractions from the model edge and the hoses. Note here also that the target model reflector should be built proportionally deep enough from the reflector above it, so that the reflection events from these two reflectors do not overlap at far offset traces. This problem can be resolved by requiring graduate students to enroll in a weight-training course.
- (e) A better technique to bury the sintered glass beads channel within two solid media is necessary to ensure a perfect contact with the channel.
- (f) Cooling surfaces that often act as reflectors within a 'homogeneous' layer should be optically scanned during model construction.

APPENDIX A

Transducer Calibration

Ultrasonic signals emitted by piezoelectric transducers depend strongly on transducer material, thickness, diameter, shape, excitation frequency, as well as the coupling between the transducer and the surrounding medium. In addition, the electronic instruments, particularly the pulse signal generator and the signal pre-amplifier will affect the amplitude and phase of the recorded signal. We see these effects in our recorded wavelet shape, amplitude, phase, and directivity, which in turn will strongly impact any true amplitude physical modeling.

Over many years of physical model experimentation in the AGL, a wide range of transducers has been used to generate signals. Most of these experiments have addressed seismic illumination and imaging problems, where it is important to accurately model the phase (travel times) of reflections and multiples, with amplitudes and radiation patterns being of secondary interest. The time-lapse seismic experiment in this thesis will require accurate seismic attribute (including AVO) analysis for detecting fluid movement. Thus, choosing a transducer having a well-calibrated understanding of amplitude with angle is tremendously important. While our spherical transducers allow us to simulate marine acquisition, and are in total contact with the surrounding (water) medium, we need to

physically hold and have cables connected to the transducers which lead to angular variations in radiation pattern. At the same time, the physical properties of piezoelectric ceramics are greatly different from those of water, leading to an impedance mismatch and subsequent ringing. The conventional transducers that generate compressional waves are based on piezoelectric effects. The most commonly used disc material is PZT (lead zirconium titanate) but other materials such as quartz crystal and lead metaniobate are employed as well. Many manufacturers offer a wide selection of PZT materials that are available to suit specific applications. Table A.1 and A.2 for instance, show some PZT characteristics provided by PI (Physik Instrumente). A general discussion of piezoelectricity can be found in Auld (1977).

Product Name	Description
PIC 140	Offers high mechanical stability and polarization resistance in combination with a high mechanical Q and high Curie Point. Applications are in the field of power ultrasonics, sound navigation and ranging or medical diagnostics.
PIC 141	offers high electromechanical coupling factors with reasonable mechanical Q, good mechanical stability, and resistance to high electrical fields.
PIC 151	offers the highest piezoelectric coupling factor and very high dielectric and piezoelectric constants. It is especially suited for micropositioning components, low-frequency ultrasonic transducers, buzzers and ultrasonic speakers.
PIC 155/PIC 255	offers a high piezoelectric coupling factor, low mechanical Q and minimal response of the dielectric constants to temperature changes. The material is especially suited for low-frequency ultrasonic transducers in pulse mode, for transmission and reception over a wide temperature range and special actuator applications.

Table A.1. An example list of various PZT products available in the market.

TECHNICAL DATA:					
PZT Characteristics	PIC 140	PIC 141	PIC 151	PIC 155	PIC 255

Density [g/cm ³]	7.60	7.80	7.80	7.70	7.8
Curie Temperature [°C]	330	275	250	345	350
Dielectric Constant $\epsilon_{33}^T / \epsilon_0$	1200	1300	2100	1500	1750
Dielectric Constant $\epsilon_{11}^T / \epsilon_0$	680	1500	1980	1400	-
Dielectric Loss (tan δ [$\times 10^{-3}$])	10	5	15	20	15
Resistivity [Ω m]	10^{10}	10^{10}	10^{11}	10^{11}	-
Coupling Factors					
k_p	0.50	0.58	0.62	0.62	0.62
k_{33}	0.60	0.66	0.69	0.69	0.35
k_{31}	0.25	0.31	0.34	0.35	0.69
Mechanical Q	350	1250	120	80	80
Frequency Constants [Hzm]					
N_p	2200	2200	2100	1950	2000
N_1	1680	1610	1500	1430	1420
N_3	1800	1925	1680	-	-
N_t	2100	2050	1950	1985	2000
Voltage Constants [$\times 10^{-3}$ Vm/N]					
g_{31}	- 8.5	- 13.1	- 11.5	-12.4	-11.3
g_{33}	28.2	29.0	22.8	27.0	25.1
Elastic Constant [$\times 10^{-12}$ m ² /N]					
S_{11}^E	11.7	12.4	15.0	15.6	16.1
S_{33}^E	11.7	13.0	19.0	19.7	20.7

Table A.2. Technical specification of PZT materials described on Table A.1.

The transducer backing material is most commonly epoxy or araldite doped with tungsten powder but other powders such as uranium oxide and lead have been used. The effect of

the low Q backing material is to absorb energy radiated in the direction opposite that of the front face of the transducer disc, thereby damping resonance and increasing the bandwidth of the resulting transducer (Figure A.1). Epoxy and araldite have lower velocities than our piezoelectric crystals; by adding high-density powders we can increase the impedance of the backing, $Z = \rho v$, to match that of our crystal.

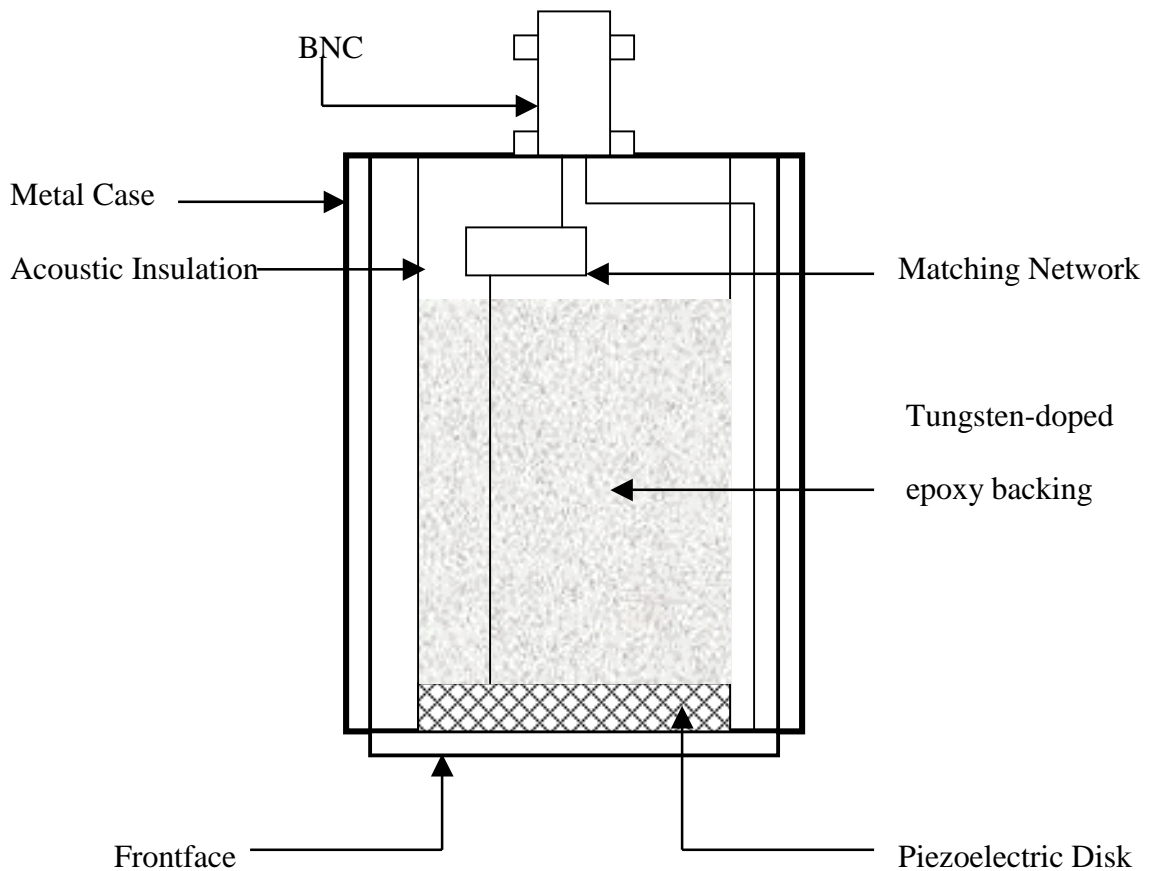


FIG. A.1. Cross section through a contact transducer.

Experimental technique

Given our need to calibrate amplitude and radiation pattern, I designed a methodology to evaluate the Edo Acoustics SN 327 spherical transducer used in my data acquisition. The aim of the evaluation is to show how the amplitude of SN 327 varies with angle. Two spherical transducers facing each other in the water tank were arranged such that one remained stationary while the other rotated 180 degrees about its axis. This arrangement gives a constant distance between the source and receiver. Using the Panametrics 5055PR Pulser Receiver, transmission signals were recorded at every 15 degrees of rotation starting from 0 to 90 degrees. This was done by marking the table plate in the water tank with an angle grid and using it as a reference (Figure A.2). At each transducer position I recorded 10 traces in order to increase the signal to (random background) noise level. After vertically stacking the 10 traces for each angle (Figure A.3), the maximum amplitude of every stacked trace was picked and plotted vs. angle giving the corresponding angle values. The directivity pattern is shown in Figure A.4. We note the radiation pattern is broad and varies by only 10% between ± 60 degrees, well within the limits needed in seismic reflection analysis.



FIG. A.2. Beam pattern data collection setup in the acoustic (water) tank.

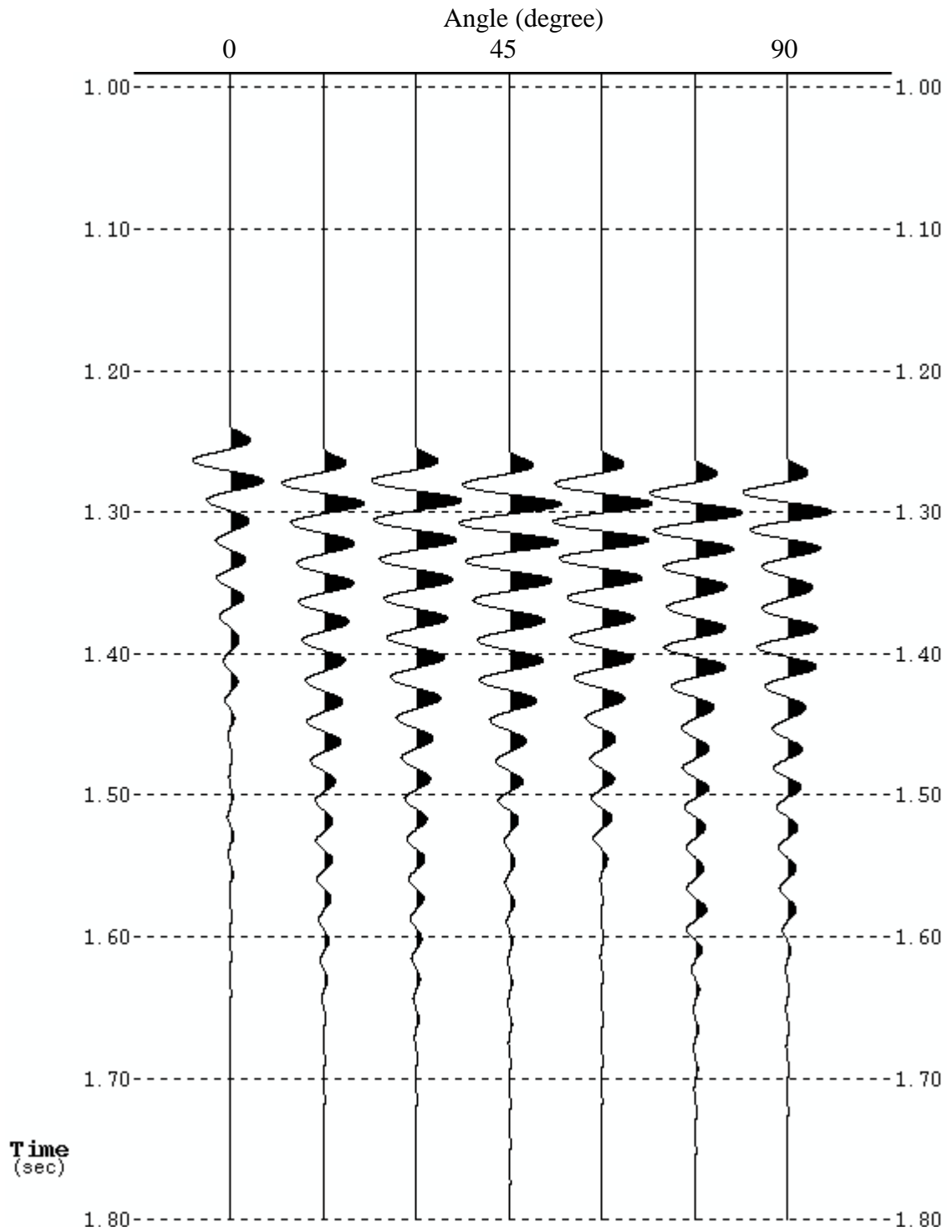


FIG. A.3. Seismic traces from 0 to 90 degrees with 15 degrees angle increment of a pair of spherical transducers. Arrival time differences between traces are due to small radius variation during transducer rotation.

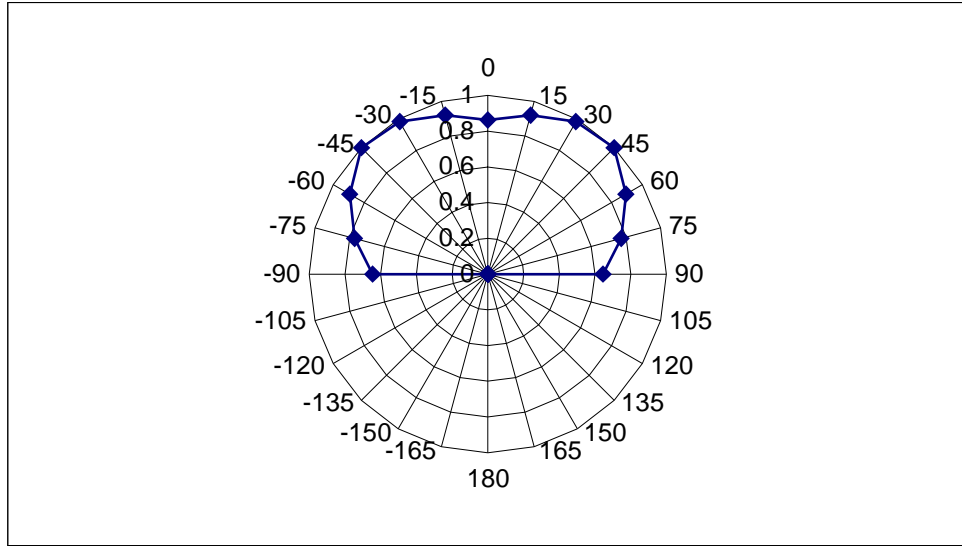


FIG. A.4. Amplitude-angle directivity of a single 300 kHz spherical transducer (SN 327, Edo Acoustics) extracted from the data shown in Figure A.2.

As mentioned above, transducers radiate ultrasonic signals differently due to their material characteristics and shape. Measuring the radiation pattern of different pairs of transducers, therefore, is an important task; first to examine how a particular transducer performs its directionally, and secondly to obtain the wavelet shape for use in inverse filtering during data processing. Following the first attempt for directivity measurement using two spherical transducers (SN 327, Edo Acoustics) for both source and receiver, I now examine two compressional-wave contact transducers (V103, Panametrics). Data were collected as shown in Figure A.2, but in an elastic tank while using a container to hold the water (Figure A.5). Unlike the omni-directionality of spherical transducer, the radiation pattern of the contact transducer shown in Figure A.7 is beamed about 0 degrees falling to 20% of the peak amplitude at ± 15 degrees. This narrow beam is due to the contact transducer disk being 3 wavelengths in diameter (in water) at its resonance

frequency of 300 kHz. While such a directed beam may be desirable in nondestructive testing and medical imaging applications, it is inappropriate for modeling the broad beam signals generated by the seismic airgun and vibrator array we wish to simulate.

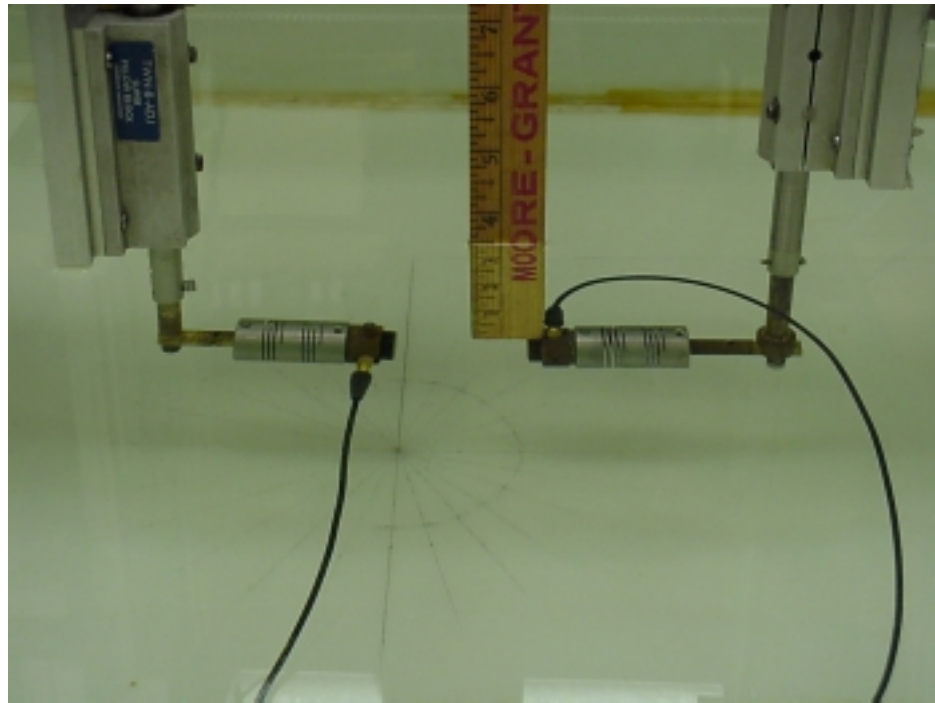


FIG. A.5. Beam pattern data collection setup in the elastic tank for a pair of contact transducers.

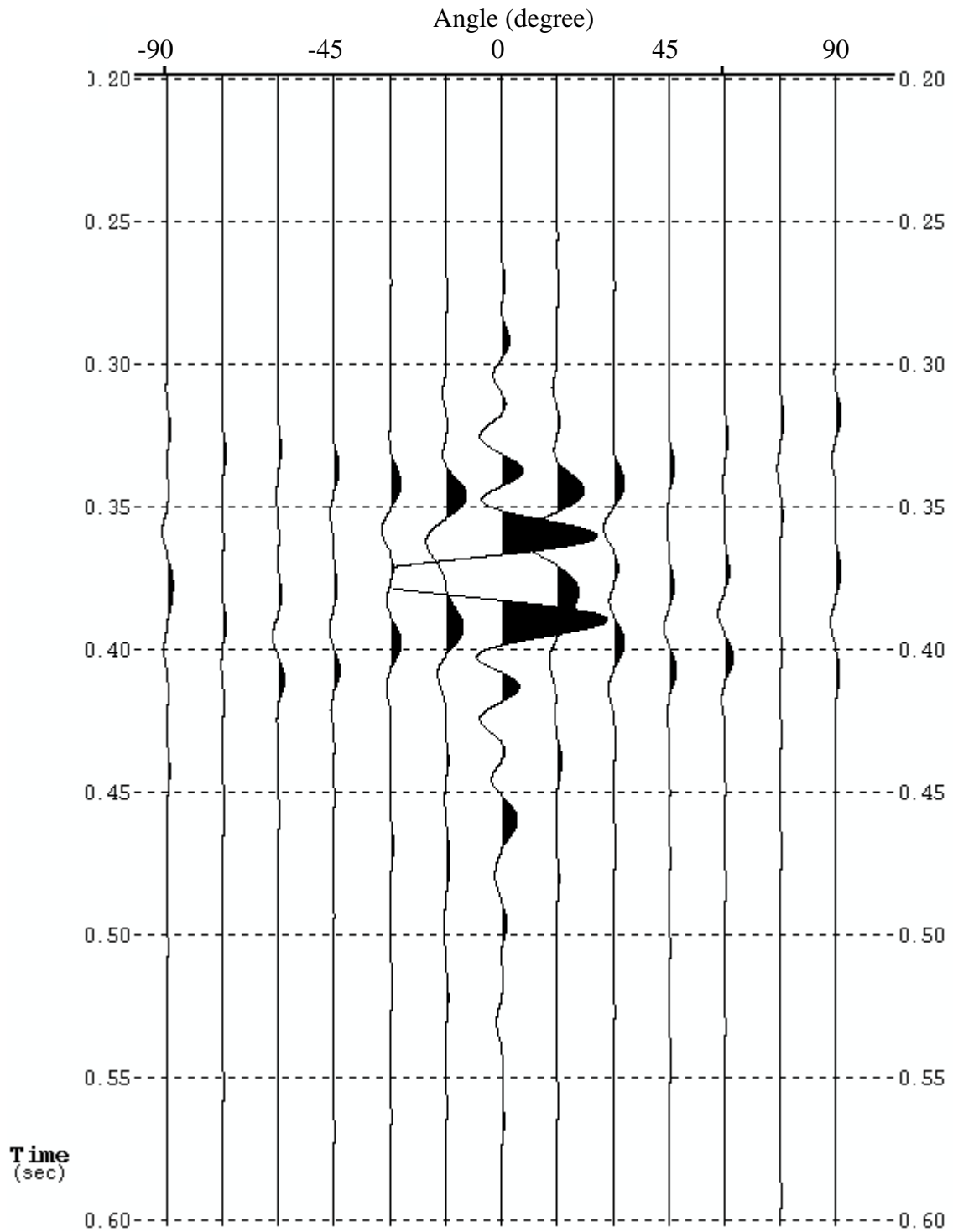


FIG. A.6. Seismic traces from -90 to 90 degrees with 15 degrees angle increment of a pair of contact transducers. Arrival time differences are due to small radius variation during transducer rotation.

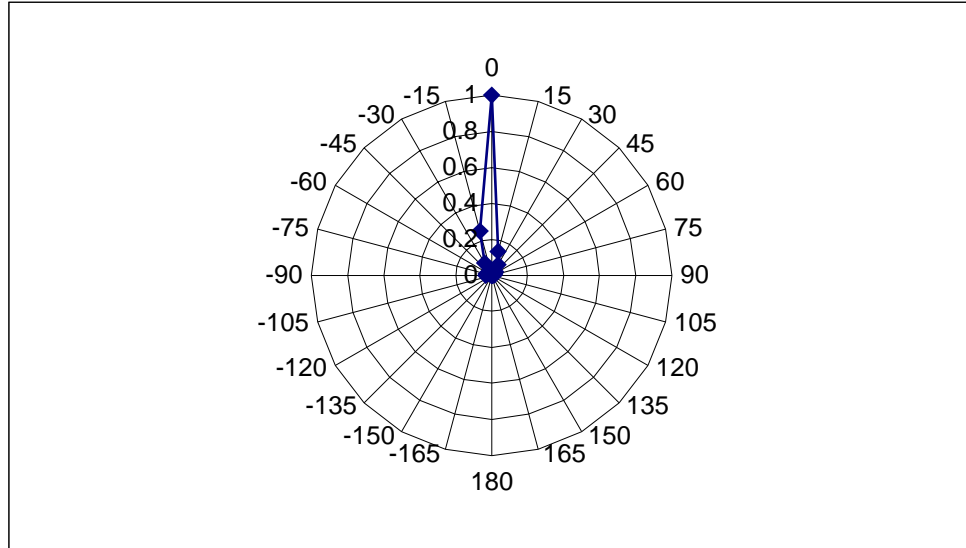


FIG. A.7. Amplitude-angle directivity of a single contact transducer (V103, Panametrics) extracted from the data shown in Figure A.6.

Noting that the tungsten-doped epoxy backed contact transducer response is less ringy (broader band) than the spherical transducer, I decided to use a contact transducer as the receiver and a spherical transducer as the source to calibrate the response of a single spherical transducer (Figure A.8).

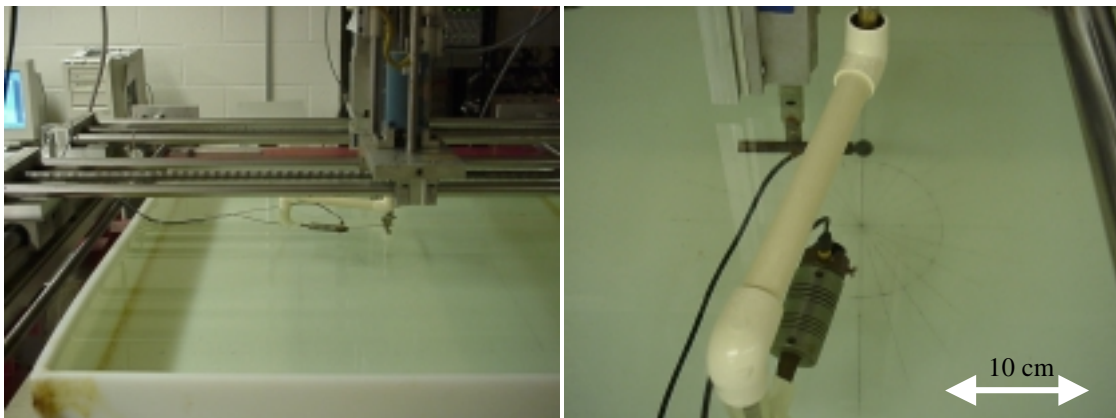


FIG. A.8. Beam pattern data collection setup in the elastic tank for a spherical (source) transducer and a contact (receiver) transducers. The apparatus is rotated so that the face of the flat contact transducer always faces the spherical transducer.

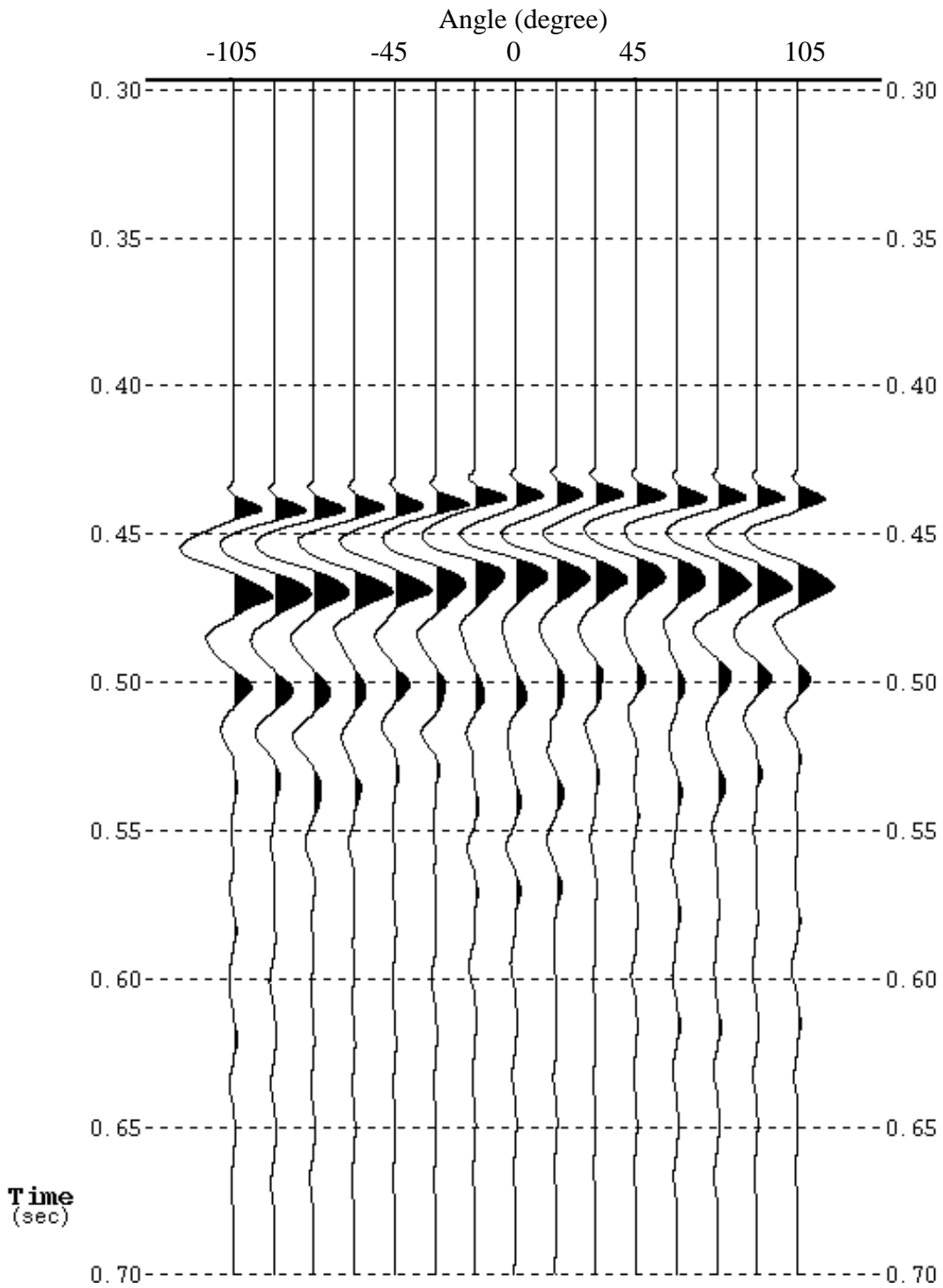


FIG. A.9. Seismic traces generated by a spherical transducer recorded by a contact transducer as shown in Figure A.8 from -105 to 105 degrees with 15 degrees increment angle. The drift away from a constant arrival time is due to inaccuracy of centering the measurement arc exactly about the center of the spherical transducer.

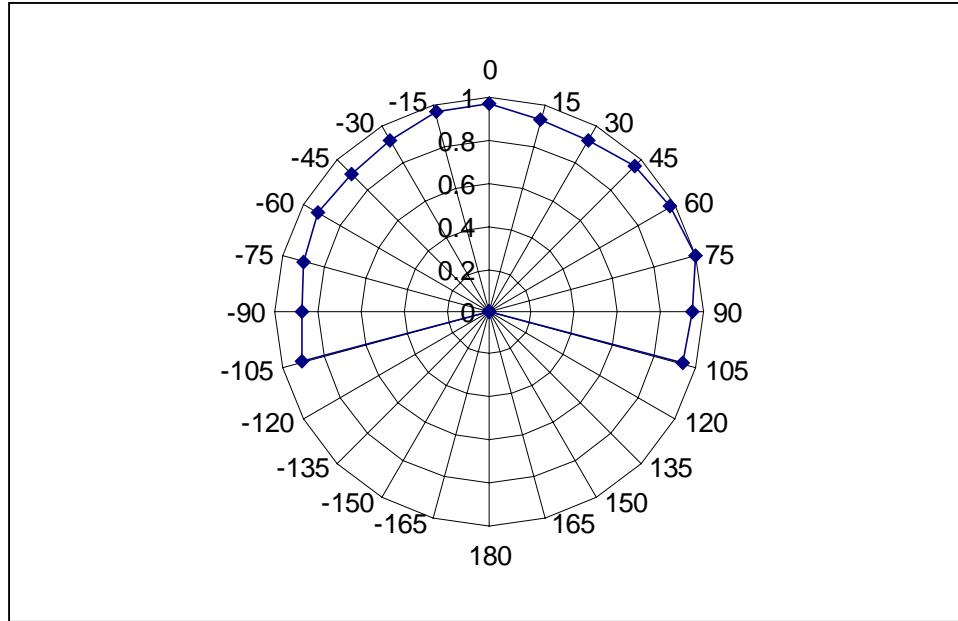


FIG. A.10. Amplitude-angle directivity of a single spherical transducer measured with contact transducer extracted from the data shown in Figure A.9.

The acoustic response shown in Figure A.9 shows the wavelet corresponding to Figures A.6 and A.7. The response has less ringing than that in Figure A.3, but more than in Figure A.6. Clearly, the spherical transducers ring badly near their resonance frequency. The beam pattern (Figure A.10) tells us that the spherical transducer in general radiates close to an omni-directional signals.

Amplitude versus Frequency

One means of avoiding the undesirable resonance yet maintaining the good radiation qualities of the spherical transducer is to excite them below resonance. In order to study

the feasibility of using a recorded sweep signal, I measured the spherical transducer directivity response using a contact transducer produced by a suite of sine waves varying from 50 kHz to 450 kHz generated by our Agilent 33120A Function/Arbitrary Waveform Generator (Figure A.11). Figures A.12 and A.13 show the amplitude as a function of angle and as a function of frequency, respectively. Two things to be noted are: first, the amplitudes are increasing faster when the source frequency almost reach the transducer dominant frequency at 350 kHz; secondly, the frequency range of 150 kHz to 300 kHz gives the most stable omni-directionality pattern compared to those outside the range.

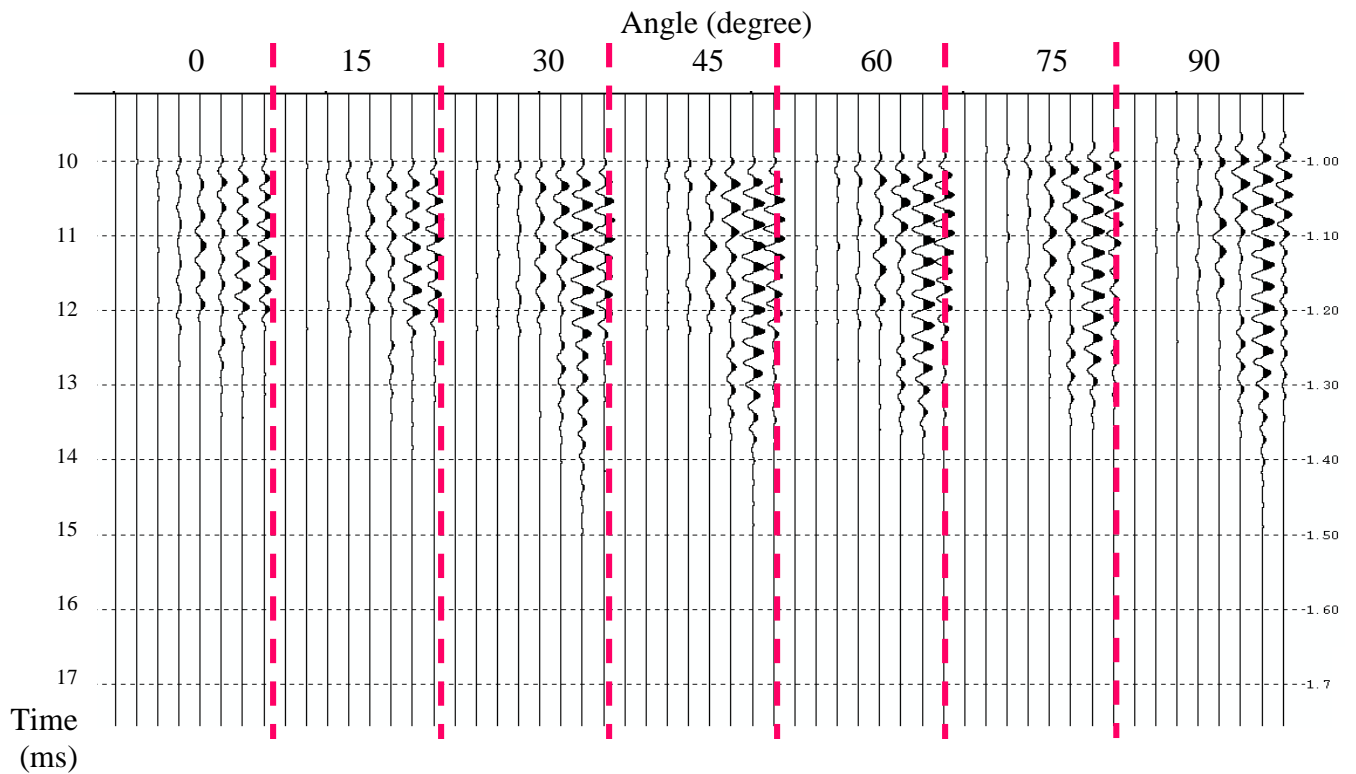


FIG. A.11. Seismic response of spherical transducer using 2 ms sine wave source signature at various frequencies of 50, 100, 150, 200, 250, 300, 350, and 400 kHz. Note resonance near 350 kHz.

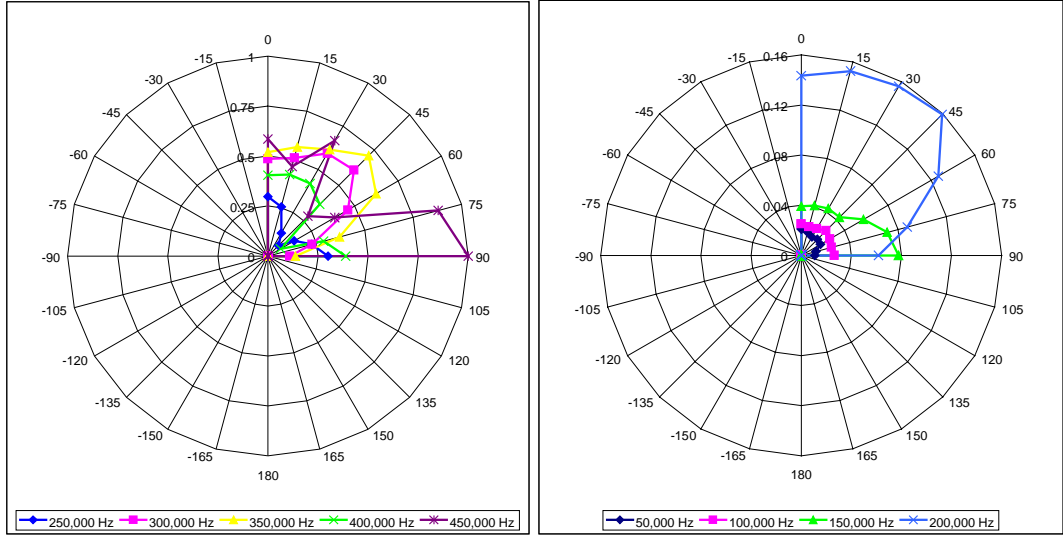


FIG. A.12. Radiation pattern of spherical transducer at various sweep frequencies extracted from Figure A.11.

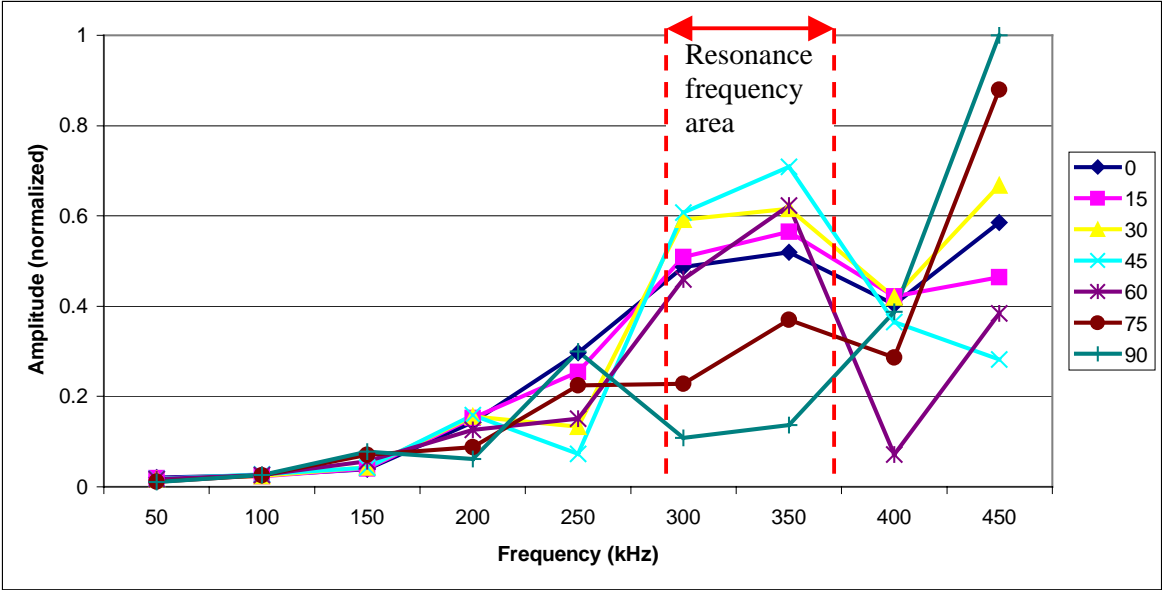


FIG. A.13. Amplitude versus frequency plot at different angles.

APPENDIX B

Reflectivity Calibration

Accurate reflection coefficients (RC) are key to conducting AVO analysis. Therefore, I designed an accurate experiment to explicitly measure how well our physical model data match those predicted by theory and by numerical models.

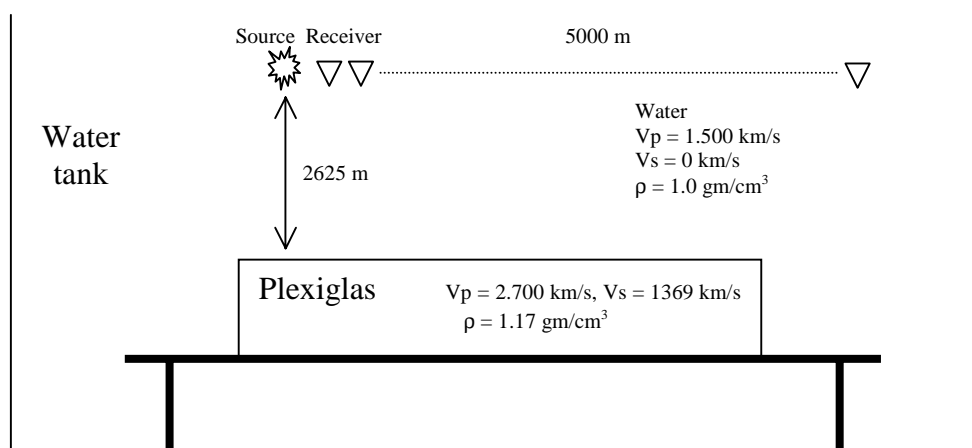


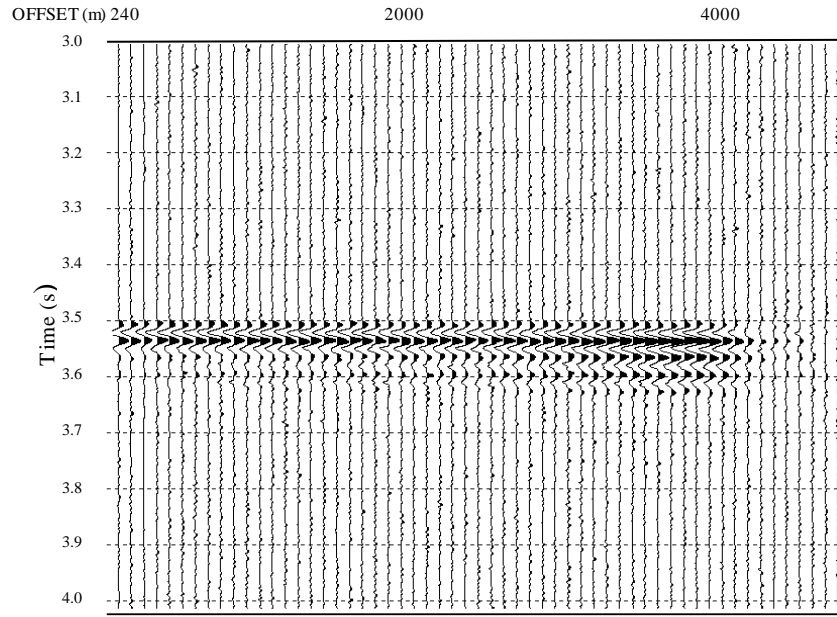
FIG. B.1. Tank acquisition setup for transducer calibration.

A single flat reflector model will be sufficient for this calibration. I used a 1.5 km thick (after scaling) plexiglas block with $V_p = 2.700$ km/s, $V_s = 1.369$ km/s, $\rho = 1.17$ gm/cc, and immersed it in the water tank. I designed a corresponding numerical model with the same velocities and densities, and calculated the response using Cerveny and Ravindra's

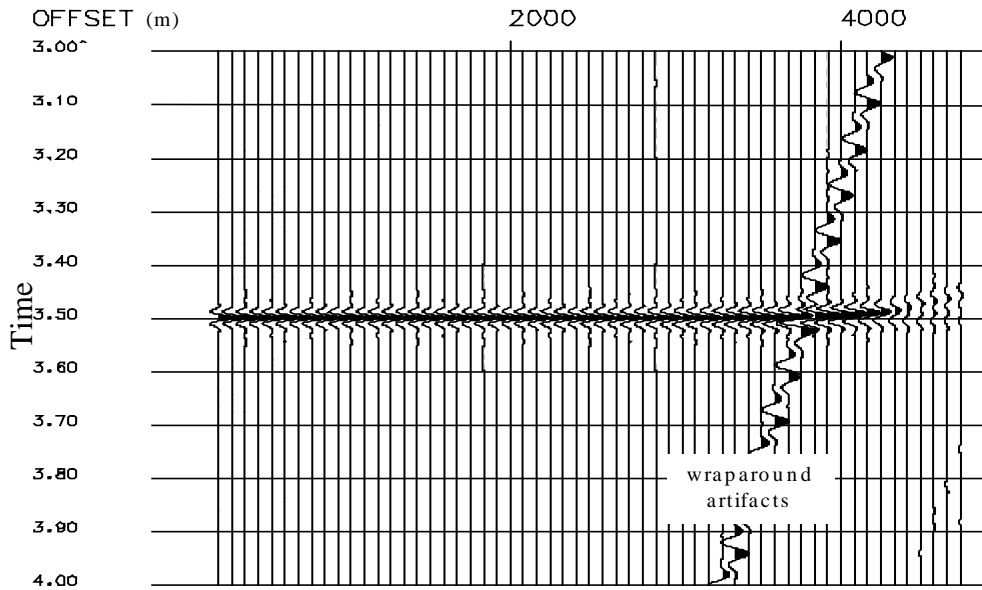
formulation (1971) equations and a commercial modeling code (Aki and Richards, 1980) provided by GDC.

In order to obtain large angles of incidence, I collected a common shot gather with 5 km offset range over the reflector at 2.6 km depth (Figure B.1). After applying a simple t^1 geometrical spreading correction, I flattened the reflection event on both the physical and numerical data (Figure B.2). Next, I calculated the trace envelope, then extracted the rms-amplitudes of the reflection signal, and divided them with that of the independently measured incident signal.

Plotting the RC values from physical model experiment and the theoretical solutions unfortunately yields unmatched curves. The physical model data shows an increase on RC with angle while both theoretical estimates show a decrease before the pre-critical angle (Figure B.3).



(a)



(b)

FIG. B.2. Flattened reflection events of the plexiglas from the (a) physical model experiment and (b) numerical modeling experiment.

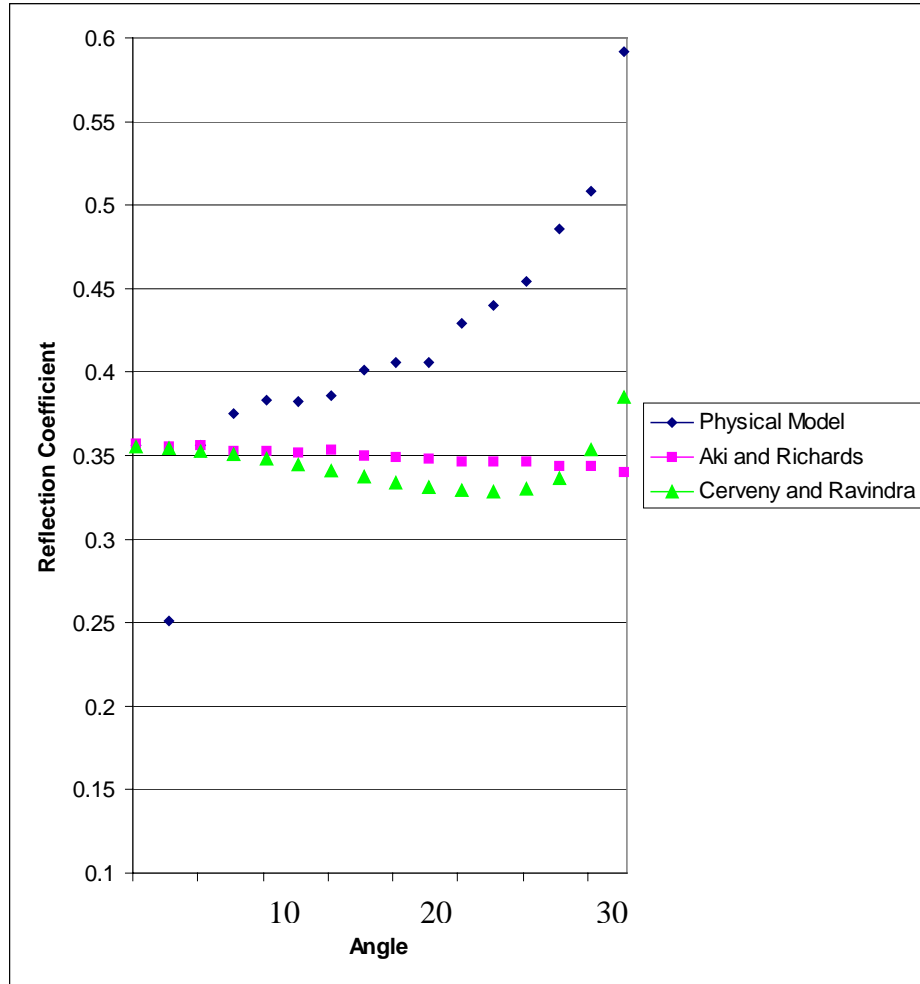


FIG. B.3. Reflection coefficient of uncorrected physical model experiment differs from that predicted by Cerveny and Ravindra's (1971) and from the Aki and Richard's solutions. the critical angle for this water/plexiglas interface is 33.7° .

While the directivity of the spherical transducers is quite constant (Figure A.10), these small changes are amplified when I use them as both source and receiver (Figure A.4). I therefore applied this directional compensation to the physical model data and display the result in Figure B.4. The RC plot of corrected amplitude due to the type of transducers, is

now reasonably close to the theoretical solutions up to the pre-critical angle of 26 degrees. I will use this calibration method for the time-lapse datasets in this thesis.

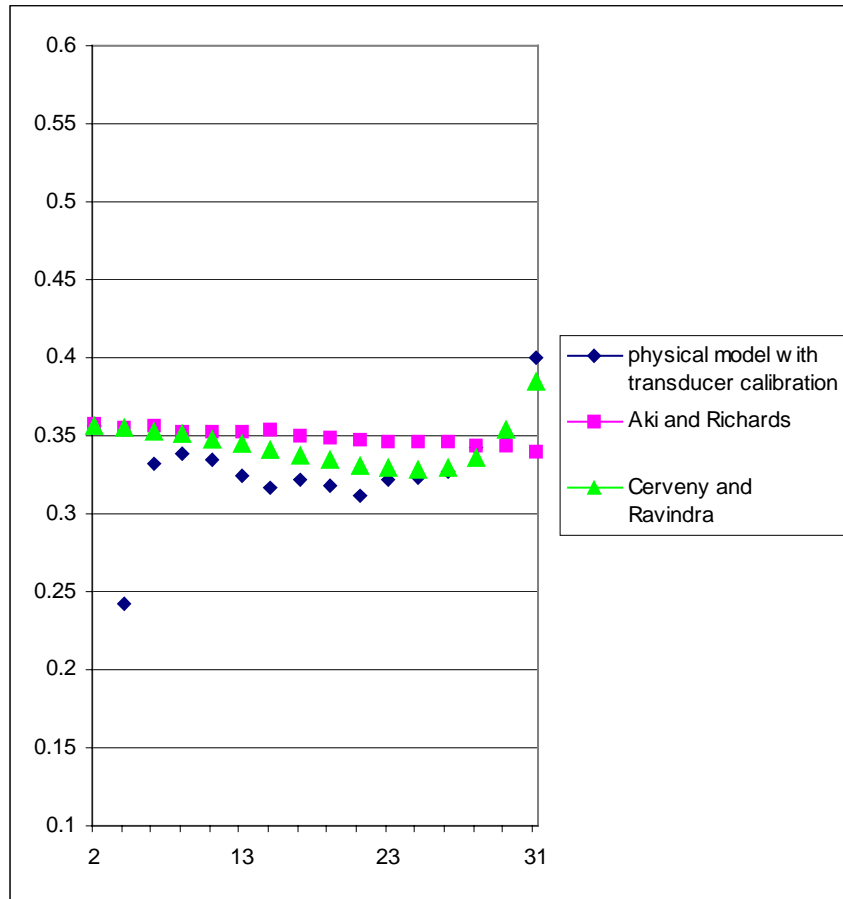


FIG. B.4. Reflection coefficient of the physical model experiment fits closer to the Cerveny and Ravindra's (1971) and Aki and Richards (1980) equations after transducer calibration correction. Data deviation at 4° angle is perhaps due to the experimental system.

APPENDIX C

Analysis of 2-D Vertically-Stacked Data

Acquisition of a 2-D line across the physical model by vertically stacking 50 traces at each source and receiver location offers greatly increased signal-to-noise ratio and hence better data resolution. After compensating for transducer directivity, and balancing the overall amplitude of two datasets, the processing flow starts with a spherical divergence correction, and continues with filtering and 2-D pre-stack time migration, prior to Normal-MoveOut (NMO), mute, and stacking (see Chapter IV.2.8).

Figure C.1 shows the migrated section through the dry and wet channel models. The channel sand image located at 1,150 ms shows insignificant amplitude changes between dry and wet channel situation. Therefore, we need to again return to and evaluate the prestack migrated data in order to interpret the AVO anomaly. In prestack gather, comparing the amplitude of near-offset channel reflection with the amplitude of near-offset water-epoxy reflection that has an estimated reflection coefficient of 0.35, results in a slight reflection coefficient difference of 0.17 and 0.20 for the dry and wet channel, respectively. This difference, unfortunately, does not correspond to the reflection coefficient prediction of 0.05 for dry and 0.33 for wet channel (see Figure 5.10). Instead, we find almost the same amplitude values on both the dry and wet stack migrated

sections. Although stacked migrated data does not allow us to predict pore-fluid content, prestack migrated data may allow us to have some insights in determining pore-fluid content. Three adjacent CDP gathers after NMO, located on top of the channel structure for air and glycerol pore-fluid content are shown in Figure C.2.

Notice that the effective reflection angle for AVO analysis falls between 0° and 30° , the pre-critical angle, that corresponds to 650 meters offset range. In Figure C.2, the dry, or air-filled channel CDP gathers shows first a decrease in channel reflection amplitude, and then an increase at further offset (up to 640 m). For the wet, or glycerol-filled channel, the reflection amplitude always decreases with offset. The difference between these dry and wet AVO responses indicates that they are distinguishable. Both amplitude variation responses follow the trend of the theoretical estimate based on Zoeppritz's solution (Figure 5.10) up to the pre-critical angle. However, two major discrepancies are found. The first is the amplitude decrease at mid-angle for the dry channel, and the second is the non-reversal of phase between dry and wet reflection events.

The reason for both discrepancies is unclear, but perhaps the channel at this particular acquisition line was not perfectly mimicking dry and wet situation due to poor fluid registration. Alternatively, since this is a 2-D line acquired over a 3-D structure, some energy coming from this line may be recorded and contributing some effects on the true reflection events.

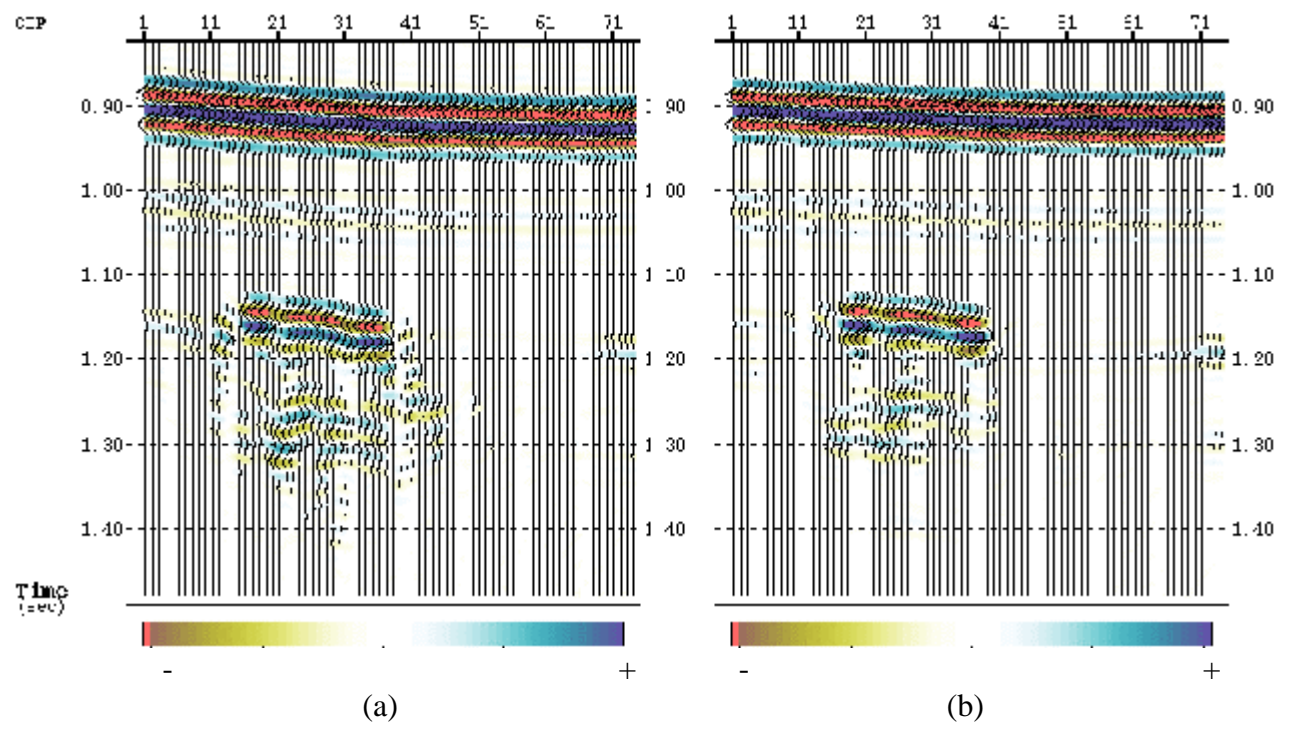


FIG. C.1. Migrated images of (a) dry and (b) wet channel sand for line 5. The amplitude between both images shows insignificant changes.

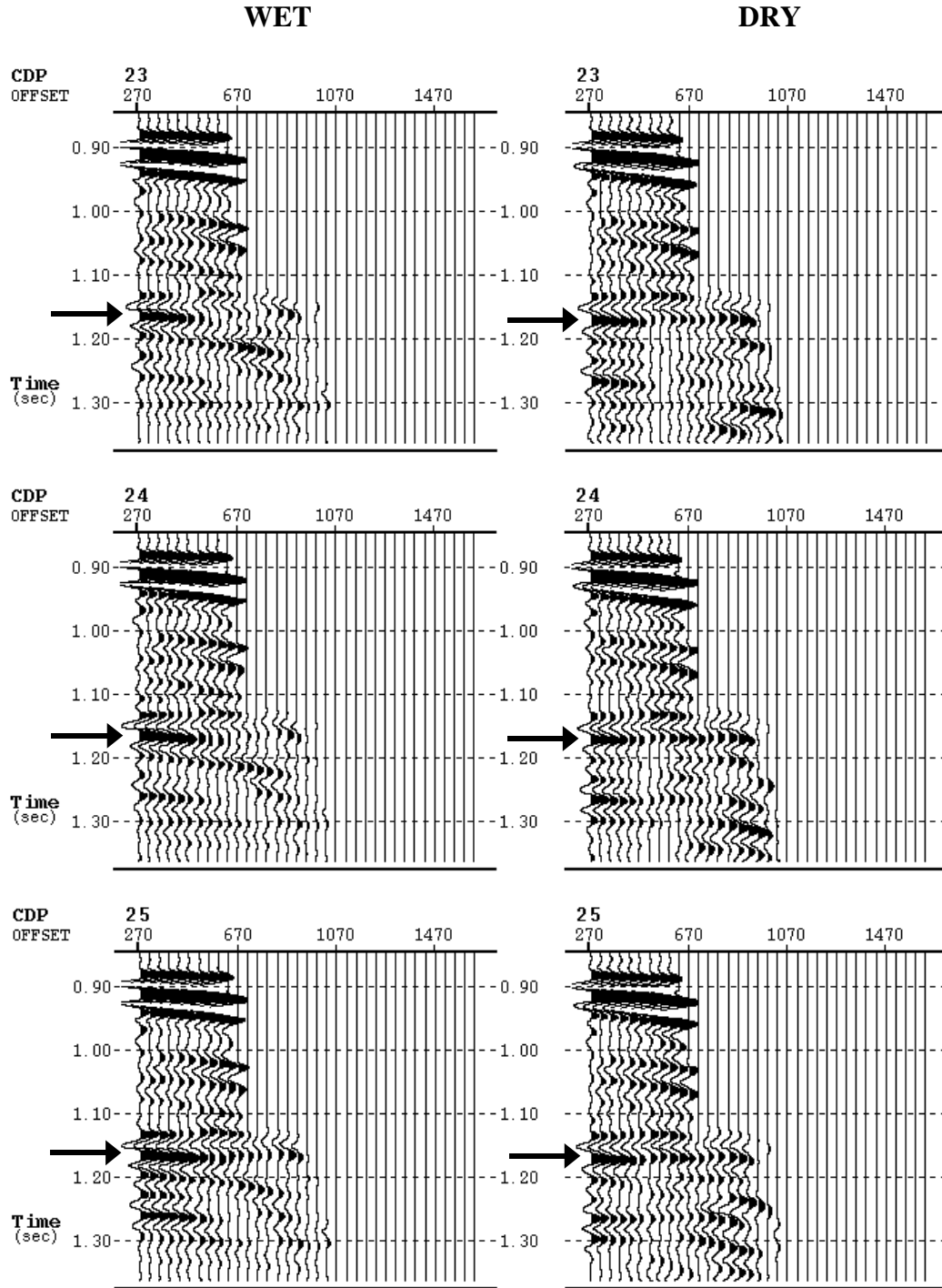


FIG. C.2. Three CDP gathers along line 5 from dry and wet 2-D datasets indicate an amplitude increase for the dry channel and an amplitude decrease for the wet channel. Unfortunately, the predicted phase reversal is not found in this comparison.

REFERENCES

- Aki, K., and Richards, P. G., 1980, *Quantitative Seismology - Theory and Methods*, vol.1, W.H. Freeman and Co., San Francisco.
- Auld, B. A., 1973, *Acoustic Fields and Waves in Solids*, John Wiley & Sons, Canada.
- Berge, P. A., Bonner, B. P., and Berryman, J. G., 1995, Ultrasonic velocity-porosity relationships for sandstone analogs made from fused glass beads: *Geophysics*, **60**, 108-119.
- Bortfeld, R., 1961, Approximations to the reflection and transmission coefficients of plane longitudinal and transverse waves, *Geophysical Prospecting*, **9**, 485-503.
- Castagna, J., 2000, An introduction to this special section AVO: The next step, *TLE*, **19**, 1187.
- Cerveny, V., and Ravindra, R., 1971, *Theory of seismic head waves*, Univ. of Toronto Press, Canada.
- Gardner, G. H. F., Gardner, L. W., and Gregory, A. R., 1974, Formation velocity and density - The diagnostic basics for stratigraphic traps: *Geophysics*, **39**, 770-780.
- Gassmann, Fritz, 1951, Elastic waves through a packing of spheres: *Geophysics*, **16**, 673-685.

- Gik, L. D., 1997, Physical modeling for travel of seismic waves in porous and fractured media: *Russian Geology and Geophysics*, **38**, 848-858.
- Hilterman, F., 2001, *Seismic Amplitude Interpretation: 2000 Distinguished Instructor Short Course (DISC)*, SEG, Tulsa.
- House, L., Larsen, S., and Bednar, J. B., 2000, 3-D elastic numerical modeling of a complex salt structure: SEG Annual Meeting, Expanded Abstracts, **70**.
- Knott, C. G., 1899, Reflection and refraction of elastic waves with seismological applications, *Phil. Mag.*, **48**, 64-97, 567-569.
- Koefoed, O., 1955, On the effect of Poisson's ratios of rock strata on the reflection coefficients of plane waves, *Geophysical Prospecting*, **3**, 381-387.
- Lowenthal, D., Lu, L., Roberson, R., and Sherwood, J., 1976, The Wave Equation Applied to Migration, *Geophysical Prospecting*, **24**, 380-399.
- Marfurt, K. J., Kirlin, R. L., Farmer, S. H., and Bahorich, M. S., 1998, 3-D seismic attributes using a semblance-based coherency algorithm, *Geophysics*, **63**, 1150-1165.
- Molyneux, J. B., and Schmitt, D. R., 1999, Compressional-wave velocities in attenuating media: A laboratory physical model study: *Geophysics*, resubmitted.
- Ostrander, W. J., 1984, Plane-wave reflection coefficients for gas sands at non-normal angles of incidence, *Geophysics*, **49**, 1637-1648.

- Richards, P. G., and Frasier, C. W., 1976, Scattering of elastic waves from depth-dependent inhomogeneities, *Geophysics*, **41**, 441-458.
- Rutherford, S. R., and Williams, R. H., 1989, Amplitude-versus-offset in gas sands, *Geophysics*, **54**, 680-688.
- Sherlock, Don H., 1999, *Seismic Imaging of Sandbox Models*, PhD thesis, Curtin Univ. of Tech, Australia.
- Sherwood, J., Kan, T. K., and Crampin, S., 1983, Synthetic seismograms in a solid layered earth: SEG Annual Meeting, **53**, SEG.
- Shuey, R. T., 1985, A simplification of the Zoeppritz equations, *Geophysics*, **50**, 609-614.
- Sparkman, G., 1998, Introduction: Time lapse or time elapse?, *Leading Edge*, **17**, 1386-1387.
- Stolt, R. H., 1978, Migration by Fourier transform, *Geophysics*, **43**, 23-48.
- Verm, R., and Hilterman, F. J., 1995, Lithology color-coded seismic sections: The calibration of AVO crossplotting to rock properties, *TLE*, **14**, 847-853.
- Winkler, K. W., 1983, Frequency dependent ultrasonic properties of high-porosity sandstones: *Journal of Geophysical Research*, **88**, 9493-9499.
- Yilmaz, O., 1987, *Seismic Data Processing*, SEG, Tulsa.
- Zoeppritz, K., 1919, Erdbebenwellen VIII B, On the reflection and propagation of seismic waves, *Göttinger Nachrichten*, **I**, 66-84.